University of Dundee

DOCTOR OF PHILOSOPHY

Sediment size effects on self-organisation behaviour of rip channels

Chen, Yiqiang

Award date:
2014

Link to publication

General rights
Copyright and moral rights for the publications made accessible in the public portal are retained by the authors and/or other copyright owners and it is a condition of accessing publications that users recognise and abide by the legal requirements associated with these rights.

- Users may download and print one copy of any publication from the public portal for the purpose of private study or research.
- You may not further distribute the material or use it for any profit-making activity or commercial gain
- You may freely distribute the URL identifying the publication in the public portal

Take down policy
If you believe that this document breaches copyright please contact us providing details, and we will remove access to the work immediately and investigate your claim.

Download date: 22. Jan. 2021

DOCTOR OF PHILOSOPHY

Sediment size effects on self-organisation behaviour of rip channels

Yiqiang Chen

2014

University of Dundee

Conditions for Use and Duplication
Copyright of this work belongs to the author unless otherwise identified in the body of the thesis. It is permitted to use and duplicate this work only for personal and non-commercial research, study or criticism/review. You must obtain prior written consent from the author for any other use. Any quotation from this thesis must be acknowledged using the normal academic conventions. It is not permitted to supply the whole or part of this thesis to any other person or to post the same on any website or other online location without the prior written consent of the author. Contact the Discovery team (discovery@dundee.ac.uk) with any queries about the use or acknowledgement of this work.

Sediment size effects on self-organisation behaviour of rip channels

Yiqiang Chen

October 2014

A thesis submitted to the University of Dundee for the degree of Doctor of Philosophy in the School of Engineering, Physics & Mathematics

Declaration

I declare that this work is original, except where indicted by special reference in the text. No part of the work referred to in the thesis has been submitted in support of an application for any another academic degree.

SIGNED: …… DATE: ……..

Certificate

This is to certify that Yiqiang Chen has done this research under my supervision, and that he has fulfilled the condition of Ordinance 14 of the University of Dundee, so that he is qualified to submit the following thesis in application for the degree of Doctor of Philosophy.

SIGNED: …… DATE: …….……..

Acknowledgements

This research has been financially supported by the joint scholarship from University of Dundee and China Scholarship Council. I am grateful for this financing support, without which I would not have been able to sit concentratively in the university to finish this thesis.

Besides the financial support, a number of people have helped me on finishing this thesis, who I would like to express my acknowledgements to them. First of all, I want to thank my supervisor Prof. Ping Dong for giving me this opportunity to do this research, for his unique patience and remarkable insight, for his never-ending optimism and enthusiasm, and for giving valuable improvement on the manuscripts of this thesis.

I also want to thank Dr Qinqin Gui, Dr. Chunyan Zhou, Chunyang Xu, Dr. Haixia Xu, Dr. Jisheng Zhang, and all other people in the Division of Civil Engineering for their helpful suggestions and encouragements.

Thanks to Dr Zhengtian Song, Ke Wang, Teng Liang and other guys, as we spend very happy time in and outside of the campus. The happy times we spend together can always let me feel relax.

At last, I would like to express my sincere gratitude to my family and also myself.

Yiqiang Chen

Dundee, UK

2014

Abstract

Rip channels are frequently observed morphological pattern on the sandy beach, which are critical to the erosion of beaches as well as the safety of beach visitors. Field observations indicate the wave conditions and sediment characteristics exert the controlling effects on the states of beaches and determine the development of rip channel system. Although the role of wave conditions on the rip channel dynamics has been extensively studied, little attention has been paid to the effects of sediment characteristics.

In this thesis, the impacts of grain size of both uniform and non-uniform sediments on the formation and nonlinear evolution of rip channels have been investigated using a nonlinear morphodynamic model that is adapted from the open source program XBeach. To quantitatively describe the impacts of sediment grain size, a number of indicators that represent the dynamical and geometrical characteristics of rip channels have been used. Specifically, the indicators that related to the dynamical properties of rip channels include growth rate, migration speed, response time and saturation time. The indicators that related to the geometrical characteristics of rip channels include predominant spacing and rip channel three-dimensionality.

For beaches that consist of uniform sediment, the grain size can affect number aspects of rip channel dynamics. It is found that when the grain size increases, both alongshore migration speed and growth rate decreases significantly, while the response and saturation time increases. On the other hand, the influence of grain size on the geometrical properties of the rip channel is much less pronounced, as the predominant wavelength of rip channels hardly changes and the rip channel three-dimensionality only vary slightly, depending on either the variation of grow rate or saturation time. The “global analysis” method that takes the variables over the whole modelling domain into account is then applied to investigate the mechanism underlying the variations of growth rate and migration speed. The results of

calculation using “global analysis” method reveal that the variations of growth rate and migration speed are mainly caused by the amount of sediments being stirred up into the water column which is clearly grain-size-dependent.

Previously, all modeling studies assume that the heterogeneous sediment on sandy beach can be represented by single homogeneous sediment, which implicitly suggest that the actual dynamics of rip channels for heterogeneous sediment are either similar to those within an environment comprised of uniform sediment or equivalent to the linear summation of dynamics determined for individual grains. However, our results of simulations that using heterogeneous sediment show that in some occasion this assumption is not valid, as the values of indicators that concern to the temporal evolution properties of rip channels for heterogeneous sediment can locate outside of the range that restricted by prediction using uniform sediment. This is because the gradient of sediment concentration depends on the spatial distribution of sediment size and is not always the linear summation of the gradient of sediment concentration calculated using uniform sediment grains. Therefore, our results suggest that special care for the spatial distribution of sediment size should be taken when predicting the development of rip channels.

Contents

Declaration i
Certificate ii
Acknowledgements iii
Abstract iv
Contents 1
Notation 4
List of Figures 10
List of Tables 17
Chapter 1 Introduction 18
1.1 Sandy beach: an intriguing and complex natural system 18
1.2 Nearshore zone of sandy beach 20
1.2.1 Beach profile terminology 21
1.2.2 Hydrodynamic forcing 22
1.2.3 Types of wave-dominated beaches 28
1.3 Rip channels on sandy beach 31
1.4 Self-organization behaviour of rip channels 34
1.5 Self-organization models for rip channels 35
1.6 Motivation and aims 38
1.7 Outline of thesis 41
Chapter 2 Current understanding on the morphodynamics of rip channels 42
2.1 Introduction 42
2.2 Field observations 43
2.2.1 Observation techniques 43
2.2.2 Field observation on individual rip channel system 44
2.2.3 Field observation on the coupling between rip channel systems 49
2.3 Modeling the formation and evolution of rip channels 50
2.3.1 The morphodynamic behavior of simulated rip channel system 50

2.3.2 The modeled coupling behavior between rip channel systems 53
2.4 Summary 54
Chapter 3 The numerical model: modification of XBeach.....55
3.1 Introduction 55
3.2 Calculation procedure of XBeach 56
3.3 Governing equations 58
3.3.1 Wave-action balance equation.....58
3.3.2 Shallow water equations.....60
3.3.3 Sediment mass conservation equation.....61
3.4 Formulas for variables in the governing equations 61
3.4.1 Wave breaking and energy dissipation.....61
3.4.2 Undertow 63
3.4.3 Wave skewness and asymmetry 63
3.4.4 Bed shear stress 64
3.4.5 Sediment transport flux 65
3.4.6 Including/excluding the three dimensional cross-shore process 67
3.5 Grid setup and boundary conditions 68
3.5.1 Grid setup 68
3.5.2 Boundary conditions.....69
Chapter 4 Emergence and dynamics of rip channels on a barred beach: modified XBeach validation.....72
4.1 Introduction 72
4.2 Setup of numerical simulations.....73
4.3 Rip channel response indicators.....76
4.4 Modeling results.....78
4.4.1 Emergence and dynamics of rip channels under normal waves.....78
4.4.2 Emergence and dynamics of rip channels under oblique waves 87
4.5 Discussion 96
4.5.1 Comparison with field observations and previous numerical studies 96
4.5.2 Dynamical equilibrium.....99
4.6 Summary 100

Chapter 5 The grain size effects on rip channel dynamics for beach with uniform sediment 101
5.1 Introduction 101
5.2 Model set-up 102
5.3 Modeling results 103
5.3.1 Rip channel temporal evolution for different sediment sizes 103
5.3.2 Parameter trend of rip channel response indicators 106
5.3.3 Sediment size effect on rip channel dynamical characteristics 111
5.3.4 Sediment size effects on rip channel geometrical characteristics 124
5.4 Discussion 125
5.5 Summary 126
Chapter 6 The grain size effects on rip channel dynamics for beach with non-uniform sediment 128
6.1 Introduction 128
6.2 Multigrain sedimentation/erosion module 129
6.3 Simulations set-up 132
6.4 Modeling results 137
6.4.1 Representative simulation using uniform sediment 137
6.4.2 Representative simulations using non-uniform sediment 142
6.4.3 Temporal evolution of crescentic bar and coupling time 147
6.5 Discussion 155
6.6 Summary 157
Chapter 7 Conclusions and future works 158
7.1 Conclusions 158
7.2 Recommendations for future works 159
Bibliography 162

Notation

Roman Symbols

a_0	Approximate water depth near swash zone boundary of initial bathymetry
a_1	Approximate water depth near surf zone boundary of initial bathymetry
a_2	Sandbar amplitude
A	Wave action
A_m	Rip channel amplitude
A_s	Wave asymmetry
A_{sb}	Coefficients for bedload transport
A_{ss}	Coefficients for suspended load transport
B	Breaking related coefficient
c	Wave phase velocity
c_D	Drag coefficient calculated
c_f	Friction coefficient
c_g	Wave group velocity
c_m	Rip channels migration speed
c_x	Wave celerity in cross-shore direction
c_y	Wave celerity in longshore direction
c_ϑ	Wave celerity in directional space
C	Depth-averaged sediment concentration
C_0	Depth-averaged sediment concentration at basic state

C_1	Dimensional scaling coefficient
d_g	Grain size
$d_g(i, j)$	Grain size of ith layer and jth sediment class
$\overline{d_g}(i)$	Mean grain size of ith layer
D	Water depth
D_w	Wave energy dissipation in each directional bin
$\overline{D_w}$	Total wave energy dissipation
D_z	Thick of each sediment layer
D_*	Dimensionless grain size
E_w	Wave energy in each directional bin
$\overline{E_w}$	Total wave energy
F_x	Cross-shore component of wave forcing
F_y	Alongshore component of wave forcing
$F_z(k_l)$	Fourier coefficient for the wavenumber of k_l
$\lvert F_z \rvert$	Modulus of the Fourier coefficients
g	Gravitational acceleration
h	Bed level deviation from the initial alongshore uniform bathymetry
$h_{\max}$	Maximum of h
$h_{\min}$	Minimum of h
$\lVert h \rVert$	Rip channel three-dimensionality
$\lVert h \rVert_{ts}$	Rip channel three-dimensionality at the saturation time
H_{rms}	Root mean square wave height
H^0_{rms}	Incident root mean square wave height
k	Wave number
k_b	Kinematic viscosity of water
k_l	Wavenumber of topographic signal

k_m	The dominant mode
k_v	Layer number of the variable layer
k_x	Wave vector component in cross-shore direction
k_y	Wave vector component in longshore direction
L_x	Cross-shore length of modeling domain
L_y	Alongshore length of modeling domain
$m_g(i, j)$	Sediment mass of ith layer and jth sediment class
n_x	Grids number in x- direction
n_y	Grids number in y- direction
N_g	Number of sediment classes
N_l	Numerical layers of seabed
p	Sediment porosity
P	Production term
$p_g(i, j)$	Fraction of ith layer and jth sediment class
P_x	Production term in x- direction
P_y	Production term in y- direction
$\overrightarrow{q_s}$	Sediment transport flux
q_x	Sediment transport flux in cross-shore direction
q_y	Sediment transport flux in alongshore direction
Q_b	Fraction of breaking waves
s	Relative density of sediment
S_c	Location of shoal crest
S_{xx}	Component of wave radiation stresses
S_{xy}	Component of wave radiation stresses
S_{yx}	Component of wave radiation stresses
S_{yy}	Component of wave radiation stresses

t	Time
t_r	Rip channels response time
t_s	Rip channels saturation time
T	Wave period
u	Cross-shore depth averaged current velocity
u_a	Cross-shore component of wave velocity caused by wave nonlinearity
u_{cr}	Threshold current velocity of motion
u^E	Cross-shore Eulerian velocity
u_{rms}	Root-mean-square wave orbital velocity amplitude at seabed
u_s	Undertow in x- direction
U_r	Ursell number
v	Alongshore depth averaged current velocity
v_a	Alongshore component of wave velocity caused by wave nonlinearity
v^E	Alongshore Eulerian velocity
v_s	Undertow in y- direction
uu	u- velocity on u- grid
uv	u- velocity on v- grid
vu	v- velocity on u- grid
vv	v- velocity on v- grid
v_y	Alongshore current speed on the bar crest at the basic state
$\vec{V}$	Current velocity includes undertow and wave nonlinearity induced velocity
V_m	Amplitude of wave nonlinearity caused flow velocity
Vol_a	Active volume of sandbar
x	Cross-shore coordinates
x_c	Sandbar crest location
x'	Cross-shore coordinates with origin at the shoreline
y	Alongshore coordinates

z_0	Initial alongshore uniform bathymetry
z_b	Seabed level
z_{c0}	Base level of bed sediment column
z_r	Roughness length

Roman Symbols

α	Depth-integrated volumetric sediment concentration
α_w	Wave breaking related coefficient
β_1	Shoreline slope
β_2	Offshore slope
γ	Bed slope coefficient
γ_1	Wave break index
γ_2	Free parameter
γ_b	Wave breaker index
γ_{ua}	Calibration factor
Γ	Bed diffusive coefficient
Γ_{vor}	Vorticity of current
Δ	Damping term
Δx	Grid size in x- direction
Δy	Grid size in y- direction
η	Water surface level
θ	Wave direction
θ^0	Incident wave angle
λ_1	Initial predominant wavelength
λ_m	Rip channels predominant spacing
λ_{mean}	Mean wavelength of rip channels
ρ	Water mass density

σ	Intrinsic wave frequency
τ_x	Cross-shore component of bed shear stress
τ_y	Alongshore component of bed shear stress
ν_h	Horizontal viscosity coefficient
Ω	Rip channels growth rate
Ω_1	Initial growth rate
Ω_i	Initial growth rate of transverse bar
Ω_o	Initial growth rate of crescentic bar

List of Figures

Figure 1.1 Temporal and spatial scales of different morphological features that appear on sandy beaches. 20
Figure 1.2 The nearshore zone of sandy beach, adapted from Komar (1998). 22
Figure 1.3 Schematic energy spectrum of ocean surface waves, adapted from Kinsman (2013). 23
Figure 1.4 A three-dimensional plot of the edge wave 24
Figure 1.5 (a) Undertow and (b) longshore currents in the nearshore zone of sandy beaches. 25
Figure 1.6 Rip current circulations under (a) normal and (b) oblique waves for alongshore non-uniform bathymetry. 27
Figure 1.7 Sketch of reflective beach state. Adapted from Short (1999). 29
Figure 1.8 Sketch of dissipative beach state. Adapted from Short (1999). 29
Figure 1.9 Sketch of intermediate beach, which includes four subtypes namely longshore bar-trough (LBT), rhythmic bar and beach (RBB), transverse bar and rip current (TBR), ridge-runnel or low tide terrace (LTT). Adapted from Short (1999). 30
Figure 1.10 Rhythmic morphological features on sandy beaches. a) Beach cusps at Tairua beach, New Zealand (Almar et al., 2008); b) Crescentic bar in Hainan, China; c) Oblique sandbar at Southwest France (Google Earth imagery). 32
Figure 1.11 Observed coexistence of rip channel systems. a) inner-bar patterns and shoreline undulations on New South Wales Coast, Australia (Castelle et al., 2010a) and b) inner-bar patterns and outer-bar patterns on sandy beach at Aquitanian Coast, France (Castelle et al., 2007).....34
Figure 1.12 Illustration of the self-organization theory, in which the positive feedback promote the growth of bed patterns and the negative feedback prohibit the formation of patterns. 36
Figure 1.13 Classification of existed self-organization models 37

Figure 2.1 Four time exposure images of different intermediate beach states at Palm Beach. (a) LBT on 8th May 1996, (b) RBB on 15th May 1996, (c) TBR on 25th May 1996, and (d) LTT on 11th June 1996. Adapted from Ranasinghe et al. (2004). 45

Figure 2.2 Merging (left) and splitting (right) of rip channels, observed on the Gold Beach, Australia. Adapted from van Enckevort et al. (2004). 47

Figure 3.1. Computation procedure of the XBeach model. The underlined terms indicate the main modules included in XBeach model. The terms in bolded Italics indicate the main output of each module. 57

Figure 3.2 Staggered grid in XBeach 69

Figure 4.1 Three-dimensional view of the initial bathymetry, with the color represents the perturbations. 74

Figure 4.2 (a) Snapshot of rip channel morphology after 21.3 days of simulation for $H_{rms}^{0} = 1.0\,m,\ \theta^{0} = 0^{\circ}$. (b) The alongshore bed profile at $x = 190\,m$ for day 0 (thick line) and day 21.3 (thin line). (c) The spectrum of $|F_z(k_l)|$ for $z_b(190, y, 21.3)$. 79

Figure 4.3 The seabed with superimposed currents at day 21.3 for $H_{rms}^{0} = 1.0\,m$, $\theta^{0} = 0^{\circ}$ in the area between (a) 100 m<x<250 m and 1170 m<y<1800 m and (b) 230 m<x<250 m and 1500 m<y<1800 m. (c) The vorticity corresponding to (a). 80

Figure 4.4 (a) Root mean square wave height and (b) wave energy dissipation over the domain 100 m<x<250 m and 1170 m<y<1800 m for $H_{rms}^{0} = 1.0\,m,\ \theta^{0} = 0^{\circ}$ at day 21.3. The unit of colorbar is meter in (a) and W/m^2 in (b). 82

Figure 4.5 Representative paths of three different rip current circulations for $H_{rms}^{0} = 1.0\,m,\ \theta^{0} = 0^{\circ}$: (a) rip current, (b) meandering current, (c) sinuous alongshore current. The large filled dots indicate the origins of the drifters. 83

Figure 4.6 The numbers and locations of the three different rip current circulations. The open circles, filled circles and crosses in (b) represent R-, S- and M-type of circulation respectively. 84

Figure 4.7 The seabed bathymetry (left panel) and bed perturbation (right panel) at day 1 (a and e), day 6 (b and f), day 21.3 (c and g) and day 100 (d and h) of simulation for $H_{rms}^{0} = 1.0\,m,\ \theta^{0} = 0^{\circ}$. 85

Figure 4.8 The evolution of (a) growth rate and (b) rip channel three-dimensionality for $H_{rms}^{0} = 1.0\,m,\ \theta^{0} = 0^{\circ}$. The four points denoted by the arrows corresponds to day 1, day 6, day 21.3 and day 100 respectively. 86

Figure 4.9 The temporal evolution of (a) alongshore bed profile $z_b(190, y, t)$ and (b) the predominant wavelength of rip channels λ_m for $H_{rms}^{0} = 1.0\,m,\ \theta^{0} = 0^{\circ}$. Darker colours represent deeper areas. 87

Figure 4.10 (a) Snapshot of rip channel morphology after 28 days of simulation for $H_{rms}^{0} = 1.0\,m,\ \theta^{0} = 4^{\circ}$. (b) The alongshore bed profile at $x = 190\,m$ for day 0 (thick line) and day 28 (thin line). (c) The spectrum of $|F_z(k_l)|$ for $z_b(190, y, 28)$. 89

Figure 4.11 The seabed with superimposed currents at day 28 for $H_{rms}^{0} = 1.0\,m$ and $\theta^{0} = 4^{\circ}$ in the area of (a) 100 m<x<250 m and 1170 m<y<1800 m and (b) 230 m<x<250 m and 1500 m<y<1800 m. (c)The vorticity corresponds to (a). 90

Figure 4.12 Hydrodynamic experiment for $H_{rms}^{0} = 1.0\,m,\ \theta^{0} = 4^{\circ}$. (a) Lagrangian path of drifter with its origin at $x = 170\,m,\ y = 1485\,m$ (filled circle). (b) Numbers and (c) spatial distribution of drifters for three types of rip current circulations. The open circles, filled circles and crosses in (b) represent R-, S- and M- type of circulation respectively. 91

Figure 4.13 The evolution of (a) growth rate and (b) rip channel three-dimensionality. The four points denoted by the arrows corresponds to day 1.3, day 10.3, day 28 and day 300 respectively.....92

Figure 4.14 The seabed bathymetry (left panel) and bed perturbation (right panel) at day 1.3 (a and e), day 10.3 (b and f), day 28 (c and g) and day 300 (d and h) of simulation with $H_{rms}^{0} = 1.0\,m,\ \theta^{0} = 4^{\circ}$ 93

Figure 4.15 The temporal evolution of (a) alongshore bed profile $z_b(190, y, t)$ and (b) the predominant wavelength of rip channels λ_m for $H_{rms}^{0} = 1.0\,m,\ \theta^{0} = 4^{\circ}$. Darker colours represent deeper areas. 95

Figure 4.16 The temporal evolution of the predominant wavelength of rip channels λ_m for $H_{rms}^{0} = 1.0\,m,\ \theta^{0} = 6^{\circ}$ 100

Figure 5.1 Temporal evolution of (a) growth rate, (b) rip channel three-dimensionality and (c) the predominant spacing for different sediment grain size with $H_{rms}^{0} = 1.0\,m, \theta = 0^{\circ}$. 104

Figure 5.2 Temporal evolution of (a) the bed level at $(x, y) = (190\text{m}, 1500\text{m})$ and (b) the selected shoal crest position for different sediment grain size with $H_{rms}^{0} = 1.0\,m$ and $\theta^{0} = 6^{\circ}$. Note that the bed level $z_b(190, 1500, t)$ in (a) has been shifted 1 m and 2 m downward for $d_g = 0.25\,mm$ and $d_g = 0.71\,mm$ respectively. 105

Figure 5.3 Sensitivity of rip channel dynamical characteristics to sediment grain size for $\theta^{0} = 0^{\circ}$. (a) Initial growth rate, (b) response time and (c) saturation time. 107

Figure 5.4 Sensitivity of rip channel dynamical characteristics to sediment grain size for $H_{rms}^{0} = 1.0\,m$. (a) Initial growth rate, (b) response time and (c) saturation time. 108

Figure 5.5 Sensitivity of migration speed to sediment grain size and offshore wave conditions. 109

Figure 5.6 Sensitivity of rip channel geometrical characteristics to sediment grain size and offshore waves (up: wave height, down: wave angle). The filled circles in left and right panels represent the same simulations, i.e., $H_{rms}^{0} = 1\,m$ and $\theta^{0} = 0^{o}$. 110

Figure 5.7 Comparison of initial growth rate Ω_1 and the growth rate Ω_{glo} that calculated using global analysis method for $H_{rms}^0 = 1.0\,m$ and $\theta^0 = 0^o$.113

Figure 5.8 Global analysis of growth rate for $H_{rms}^0 = 1.0\,m$ and $\theta^0 = 0^o$. $\Delta / \| h \|^2$, $P / \| h \|^2$ and $P_x / \| h \|^2$ computed as a function of (a) both sediment grain size and bathymetry, (b) only bathymetry and (c) only sediment grain size. Note that the x-axis for all plots indicates the value for variable d_g. 115

Figure 5.9 Initial growth rate versus (a) $1-\theta/\theta_{crit}$ and (b) $\partial C_0 / \partial x (1-\theta/\theta_{crit})$.....117

Figure 5.10 Initial growth rate versus response time for simulations with $H_{rms}^0 = 1.0\,m$ 118

Figure 5.11 Response time versus (a) alongshore current speed on the bar crest and (b) sediment transport rate divided by the active volume of sandbar for $H_{rms}^0 = 1.0\,m$. 120

Figure 5.12 Global analysis of migration speed for $H_{rms}^0 = 1.0\,m$ and $\theta^0 = 6^\circ$. Migration speed as a function of (a) $\| \nabla q_s \| / \| \partial z_b / \partial y \|$, (b) $\overline{\nabla q_s \cdot (\partial z_b / \partial y)} / \| \nabla q_s \| / \| \partial z_b / \partial y \|$, (c) $\| \nabla q_s \|$, (d) $\| \partial z_b / \partial y \|$, (e) $\| \nabla C \|$ and (f) $\| \vec{v} \|$. 121

Figure 5.13 Migration speeds versus (a) alongshore current velocity and (b) alongshore sediment transport rate on the bar crest for $H_{rms}^0 = 1.0\,m$. .123

Figure 5.14 Initial growth rate versus saturation time for simulations with $H_{rms}^0 = 1.0\,m$ 125

Figure 6.1 Schematic representation of the vertical stacked substrate layers and the evolution of bed layers. The white arrows in (a) indicate erosion and the black arrows in (b) indicate the deposition. 131

Figure 6.2 The cross-shore variation of (a) wave energy dissipation, (b) wave height and (c) depth-averaged sediment concentration on the initial alongshore uniform bathymetry for simulation with uniform sediment (0.25 mm)

with $H_{rms}^{0} = 1.2\ m$, $T = 7.5\,s$, $\theta^{0} = 0^{\circ}$. The dashed line is at $x = 195\,m$. 133

Figure 6.3 Bathymetry (thick solid line) and the cross-shore distribution of sediment grain size for that (a) observed on Duck beach, in North Carolina, USA and (b) used in the numerical simulations with non-uniform sediments. The small circles in (a) indicate the grain size of sediment samples and their corresponding cross-shore positions, whereas the seven large circles indicate the mean grain size for seven representative locations.....136

Figure 6.4 The temporal evolution of growth rate and predominant wavelength for simulation using uniform sediment ($d_g = 0.25\,mm$). The crosses and squares represent variables for the crescentic bar near the sandbar crest and transverse bar near the shoreline respectively. 139

Figure 6.5 The snapshot of seabed in the area between (left panel) 150 m<x<240 m and 75 m<y<345 m and (right panel) 220 m<x<240 m and 150 m<y<285m for (a,d) day 2, (b,e) day 7 and (c,f) day 12.5. The darker colour indicates deeper area. 140

Figure 6.6 The evolution of (a, c) growth rate and (b, d) predominant wavelength for (left panel) transverse bar and (right panel) crescentic bar. The squares in left panel are for simulation with crescentic bar being frozen and the circles in right panel are for simulation with transverse bar being frozen. The pluses in left panel and crosses in right panel are for simulation with seabed not being frozen. 141

Figure 6.7 The temporal evolution of rip channel response indicators for four selected simulation cases, i.e.,A1 (crosses), A2 (filled triangles), B4 (open triangles) and the default uniform sediment simulation with $d_g = 0.25\,mm$ (pluses). The rip channel indicators are the growth rate of crescentic bar (a), growth rate of transverse bar (b) and the predominant wavelength of transverse bar (c). 143

Figure 6.8 Fractional variation for fine sediment and the corresponding seabed at $55\,m \le y \le 325\,m$ and $150\,m \le x \le 240\,m$ for case B4 on (a) day 2, (b)

day 4 and (c) day 10. The black thick lines indicate the area of sedimentation and grey thin lines indicate the erosion area. The colorbar indicates the change of fine sediment fraction. 144

Figure 6.9 The alongshore-averaged (a) bed profile and (b) mean sediment grain size at day 0 (solid line), day 4 (solid line with squares) and day 10 (solid line with circles) for case B4. 146

Figure 6.10 Alongshore-averaged mean sediment size for case A2 at day 0 (solid line) and day 10 (solid line with circles). 147

Figure 6.11 Saturation time of crescentic bar (a) and coupling time (b) as a function of the growth rate for crescentic bar. The circles indicate simulations using uniform sediment. The squares for case A1-A3. The stars indicate case B1-B6. 148

Figure 6.12 (a) Saturation time of crescentic bar, (b) coupling time and (c) growth rate of crescentic bar as a function of (mean) sediment size. The circles indicate simulations using uniform sediment. The squares for case A1-A3. The stars indicate case B1-B6. 150

Figure 6.13 Hydrodynamic experiments. (a) Both bed effects and sediment concentration effects are included. (b) Only sediment concentration effects are included. (c) Only bed effects are included. 152

Figure 6.14 The cross-shore distribution of depth-averaged sediment concentration and its gradient for simulations using uniform sediment on alongshore uniform beach, where no perturbation is added. The black arrows indicate the direction of sediment concentration gradient. 153

Figure 6.15 The cross-shore distribution of depth-averaged sediment concentration and its gradient for simulation B4 and two simulations with uniform sediment ($d_g = 0.1\,mm, d_g = 0.5\,mm$) on alongshore uniform seabed without perturbation. 155

List of Tables

Table 1.1 Comparison of general properties of three basic beaches.....28
Table 2.1 Residence time of different types of wave-dominated beaches at Palm Beach and Duck Beach 48
Table 3.1 Different formulas of wave energy dissipation due to wave breaking 62
Table 4.1 Input parameters for all eight simulations.....75
Table 4.2 The values of rip channel response indicators for the eight simulations ...97
Table 5.1 Input parameters for six representative simulations 102
Table 6.1 The compositions of grain size for simulations using non-uniform sediments.....135

Chapter 1

Introduction

1.1 Sandy beach: an intriguing and complex natural system

Sandy beaches, composed primarily of the wave-lain deposit of sand-sized material, are intriguing environment that commonly found along the world's coastlines. This environment has been an important habitat of human for thousands of years, as it is the place where sea meets land, ever-changing waves combine with soft sands, and is characterised by warm sunshine and blue sky. The beauty and mystery of sandy beach has also naturally made it being as the destination of millions of the world's tourists. Recently, the advent of more adventurous activities and the possibility of closer observation on the wildlife for the beach goers have also undoubtedly increased the attraction of sandy beaches for holidaymakers. Nowadays, beach tourism is booming across the globe and has created massive working opportunities for people. For example, the beach tourism and recreation was estimated to create about equivalent of AUD $1039 million per annum in southeast Queensland, Australia (Windle and Rolfe, 2013). This alternatively makes a significant contribution to the economics of cities that locate near the sandy beaches. The numerous available working opportunities and unprecedented flourishing economy of coastal cities are in turn appealing an increasing number of human populations to settle down near the beaches.

However, the rapidly expanding human populations and intense coastal exploitation has caused widespread problems on the sandy beach systems. For instance, a substantial quantity of sand from beach is mined illegally for various purposes including building constructions (Padmalal and Maya, 2014), which consequently tends to destroy the natural equilibrium of beaches. Furthermore, the application of coastal engineering measures (e.g., shoreface nourishment) can cause large and

lasting environmental impacts, such as damaging the habitat for fauna on beaches (Jones et al., 2008). In addition, global climate change, particularly the sea level rise and dramatic increase of frequency and/or intensity of extreme weather, has significantly cause the disappearing or landward retreat of beaches (Emanuel, 2005).

To overcome these problems and achieve a better use of sandy beach, coastal engineers keep on trying to make effective engineering tools and measures. However, create such tools or measures necessarily rely on strong knowledge on the physical properties of sandy beach. In the eye of coastal engineer, sandy beach is a complex physical system, not just an intriguing system as in the eye of beach goer and tourists. Categorising sandy beach as a complex system is because sandy beach is open and dissipative system, in which a large number of elements dynamically related via non-linear interactions and feedbacks. There is no doubt that sandy beach is open system as it is subject to external forcing (waves, tides). The dissipation of energy input brought by these external forcing on beaches (wave breaking, bed friction, and contribute to the sediment transport) manifests obviously the dissipative nature. The nonlinear feedbacks in beach system are ubiquitous. For example, the hydrodynamic processes including mainly waves and currents lead to deposition in some places and erosion in elsewhere, resulting changes of the seafloor topography. These changes in turn can alter the operation of the hydrodynamic processes, making the entire process being as a dynamic circle.

The nature of complexity in sandy beach system also reflects in the following three aspects. First, the temporal scales of the hydrodynamic forcing that driven the transport of sediment are in quite wide range, which can range from order of second to order of days. Second, morphological features on sandy beach are diverse, including such as ripple, mega-ripple, beach cusp, crescentic bar and sand wave (Figure 1.1), the spatial length of which can vary from $O(0.01\,m)$ to $O(10^4\,m)$. Third, different types of morphological features are common to coexist and may interact with each other.

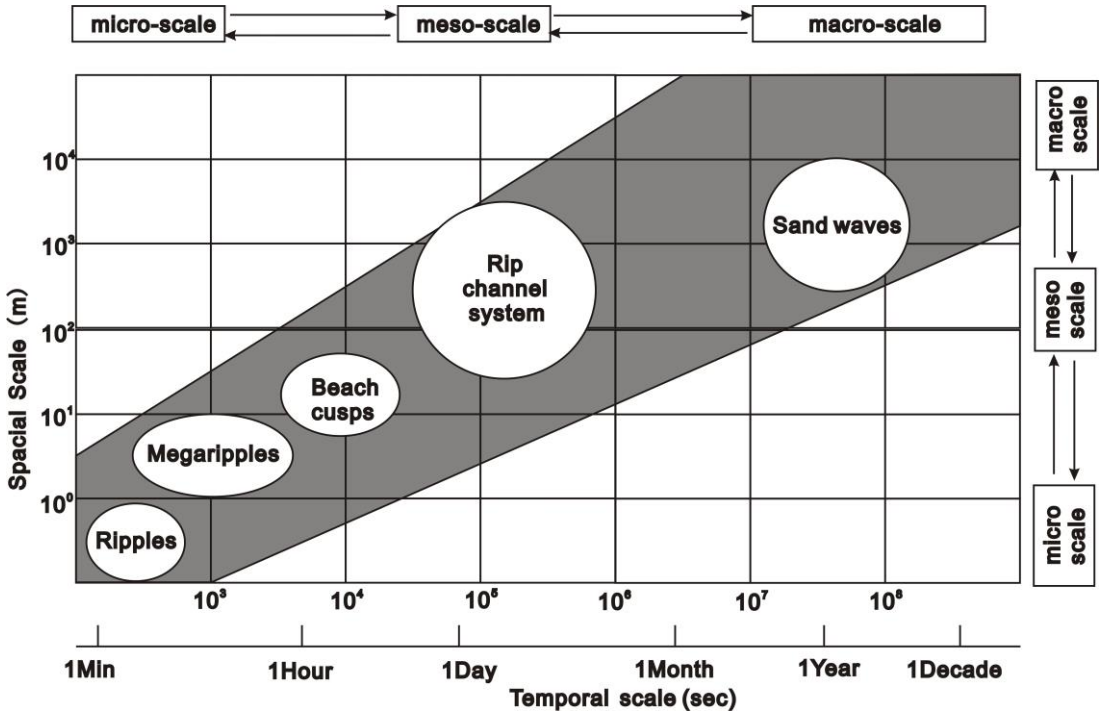

Figure 1.1 Temporal and spatial scales of different morphological features that appear on sandy beaches.

1.2 Nearshore zone of sandy beach

The sandy beaches can be generally divided into wave-dominated beaches and tide-dominated beaches, according to the hydrodynamic forcing that dominates the evolution of beaches. The term of “sandy beaches” used in the present thesis refers to wave-dominated sandy beach, as being the most common type of sandy beach observed in nature and the type of beach that is focused here. It should be noted that even on the wave-dominated sandy beach, the tidal effects can be important (Tiessen et al., 2010). However, the tidal effects are not considered in this thesis.

According to the main characteristic of processes for wave in different locations, the sandy beaches can be divided into a number of areas. Here, the area of our interest is the nearshore zone, in which we will mainly focus in the surf zone. In below, a detailed introduction on the concept of nearshore zone will be given, through introducing the terminology that related to the beach profile. Then, the

hydrodynamic forcing on sandy beaches will be described. The introduction of hydrodynamic forcing will give a background for understanding the properties of driving force for the evolution of sandy beaches. Finally, an introduction on six different types of wave-dominated beaches will be given, which range from the low energy reflective, through the four rip-dominated intermediate beaches to the higher energy dissipative beach type. Especially, the transition among the four rip-dominated beaches will be emphasized. The introduction of different types of beaches will give a background for understanding the general dynamical behaviour of rip channels.

1.2.1 Beach profile terminology

With consideration of the large differences between governing physical processes, wave-dominated sandy beaches can be divided into offshore, nearshore and backshore zones respectively (Figure 1.2). The offshore zone locates seaward beyond the closure depth. The closure depth is defined as the critical depth beyond which the seabed profile variations are no longer measurable (Reeve et al., 2004). The offshore zone is commonly stable as the water depth is deeper than the closure depth and thus the sediments are hardly to be stirred up by waves. The backshore zone is area that extending from the limit of average high-tide shoreline to dunes, which is only affected by waves during severe storms. Between the backshore zone and offshore zone is the nearshore zone, which with more specifically is bounded shoreward by the shoreline and seaward by the closure depth. The nearshore zone is almost constant evolving and is the most dynamical unit of sandy beach.

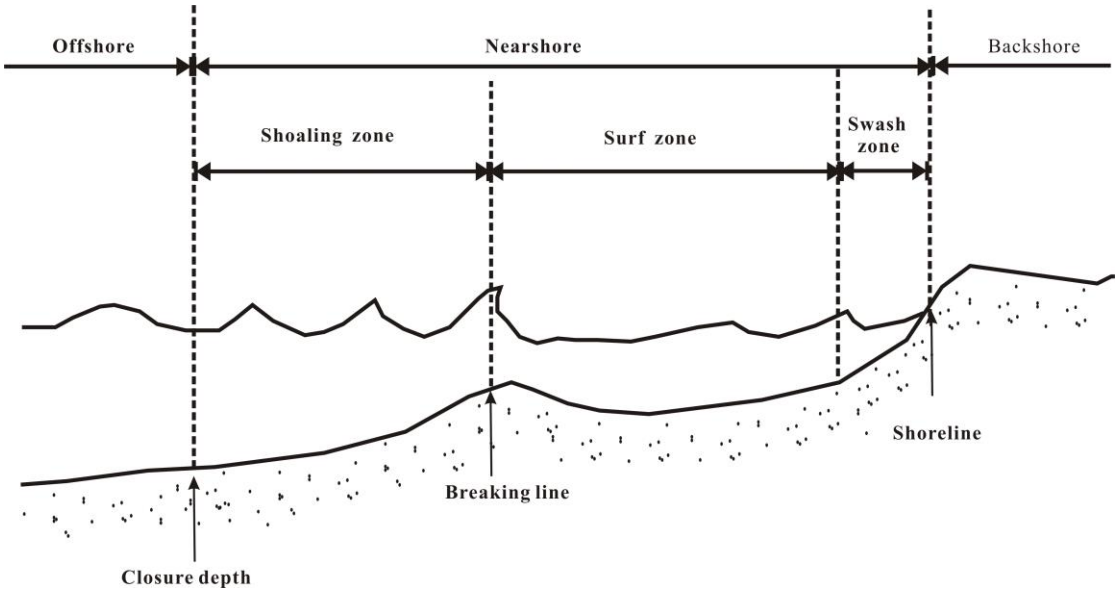

Figure 1.2 The nearshore zone of sandy beach, adapted from Komar (1998).

Depending on differences in the transformations of wave, the nearshore zone can be further divided into three subareas, namely shoaling zone, surf zone and swash zone, in turn, from the closure depth to the shoreline. The shoaling zone lies between the closure depth and the breaking line, at where wave height is about 76% of water depth and from where the waves start to break. In the shoaling zone, the wavelength of incoming wave decreases and the height of wave increases, as a result of interaction among waves and seabed. This transformation is called wave shoaling. Shoreward of the shoaling zone is the surf zone, at where wave energy dissipates significantly through wave breaking and therefore causes the wave height to decrease. Accompany with the attenuation of wave energy, a number of relevant processes take place such as generation of wave induced currents, strong turbulence actions, set-up of mean water level and vigorous sediment transport. The surf zone connects shoreward with the swash zone. The swash zone is area that alternately covered by water during the up-running of waves and exposed during the backwash.

1.2.2 Hydrodynamic forcing

In the nearshore zone of sandy beaches, the dynamics of seabed are mainly driven by hydrodynamic forcing, including that of waves and currents. Specifically, the waves

are the main hydrodynamic forcing that stir up the sediment, while the currents are mainly contribute to transport the sediment.

Waves

On sandy beaches, waves mainly fall into category to surface gravity waves, for which the disturbing force is the wind that blows over the sea surface and the primary restoring force is the gravity (Figure 1.3). The surface gravity waves and the currents they induced constitute the driving forcing that responsible for most of the sediment transport in nearshore zone. Specifically, the waves generated directly by winds are commonly called as short waves, the period of which is typically in the range of 1-30 s. In nature, many short wave trains with different periods usually coexist. The interaction or interference among these wave trains can produce the so-called infragravity waves, period of which is in the range of 30-300 s.

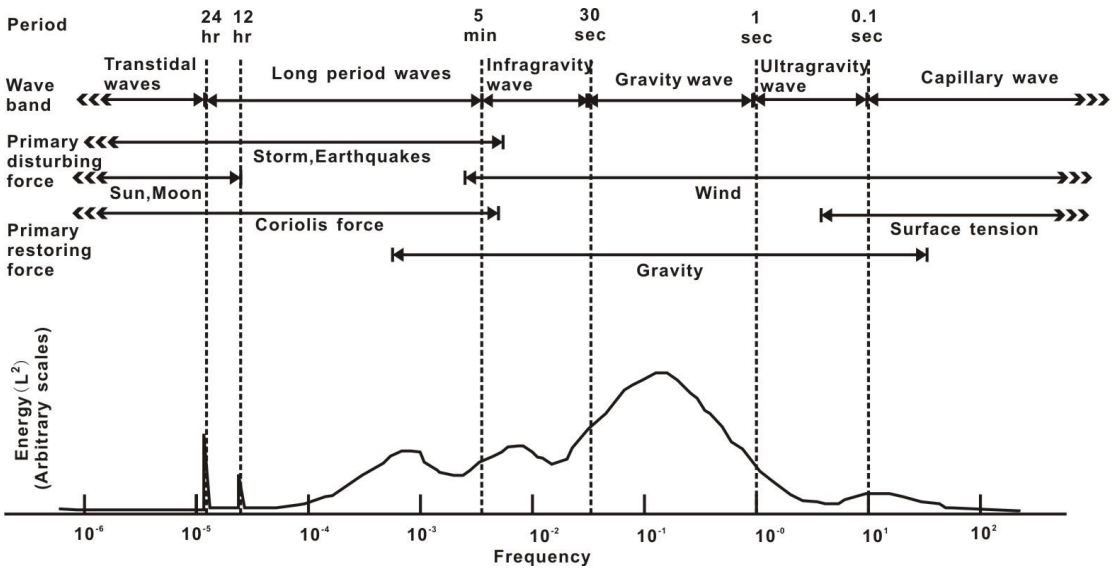

Figure 1.3 Schematic energy spectrum of ocean surface waves, adapted from Kinsman (2013).

According to the dynamic properties, the infragravity waves can be further divided into bound long wave, leaky wave and edge wave (Henderson and Bowen, 2003). Generally, the bound long waves are infragravity waves that approaching the shore

with a speed same as the group velocity of wind waves. The bound long waves tend to be released when the wind waves break, mainly in the nearshore zone. These released long waves are able to freely propagate and directly approach to the shoreline for their amplitude is relatively small. The presence of shoreline then enforces these waves to be reflected seaward, which may become trapped by the nearshore seabed as edge waves or propagate freely back into the offshore region as leaky waves. Edge waves typically have an alongshore periodicity and their amplitude decay exponentially in the seaward direction (Figure 1.4).

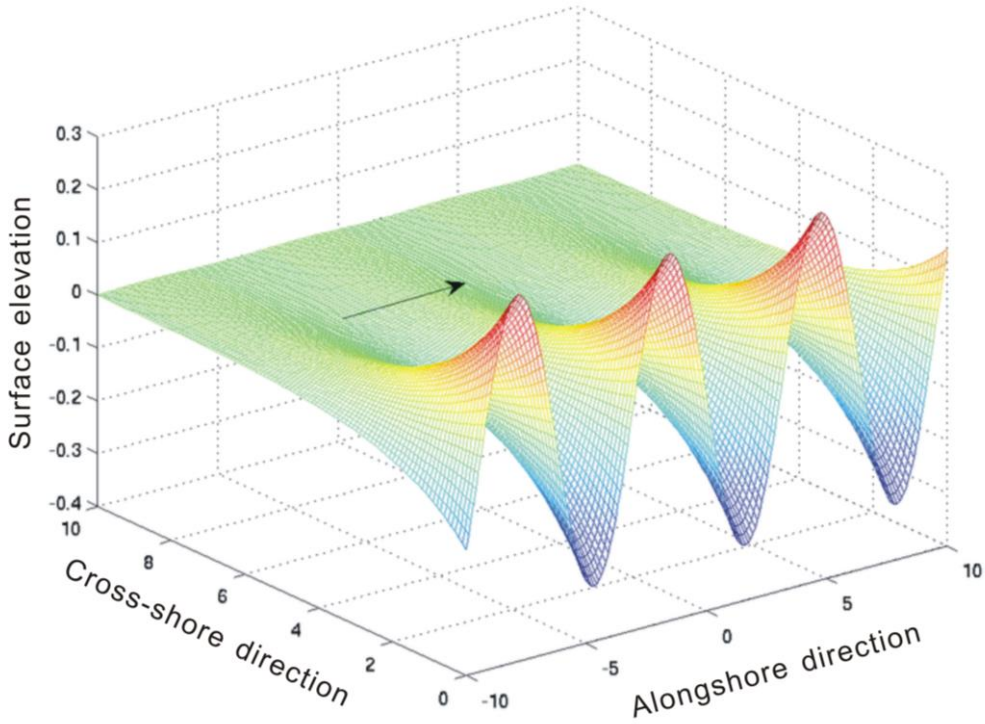

Figure 1.4 A three-dimensional plot of the edge wave

Currents

In the nearshore zone of wave-dominated sandy beaches, the currents caused by factors such as tide and wind are much less important than currents induced by wave. Therefore, we will only introduce the wave-induced currents here. The wave-induced

currents are generated due to the presence of radiation stresses, which are resulted by the travelling and breaking of waves. More specifically, the radiation stresses are an excess flow of momentum arising from the motions of waves and can produce a net force on the water body.

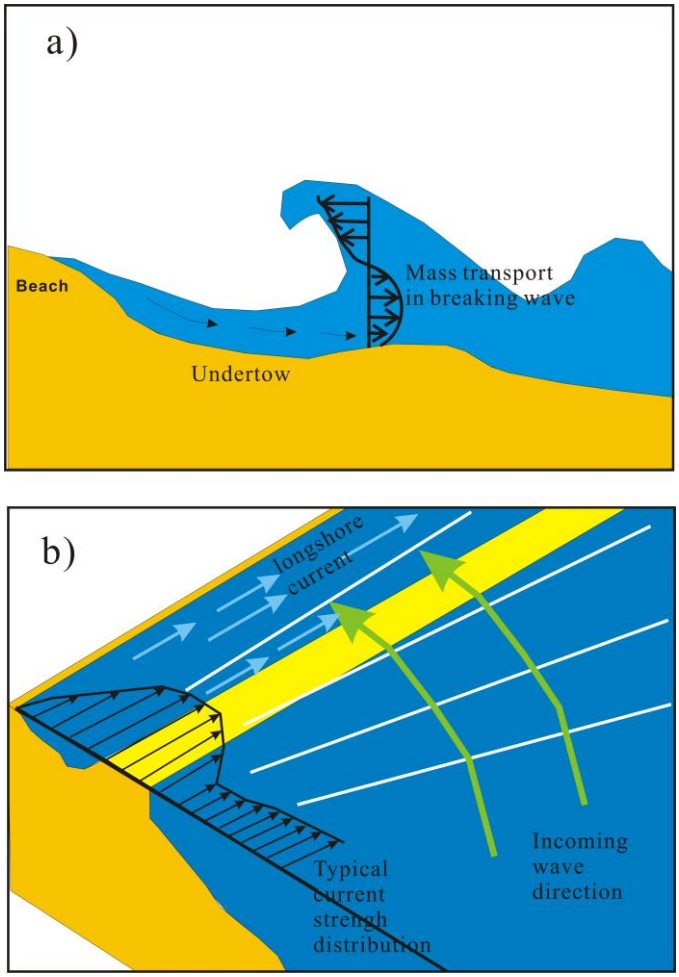

Figure 1.5 (a) Undertow and (b) longshore currents in the nearshore zone of sandy beaches.

On alongshore uniform sandy beaches, there are two main types of currents can be generated by waves. One is called undertow (Reeve et al., 2004), which is engendered by the wave-induced mass transport in order to balance the wave-induced onshore flow of water as the presence of the beach shoreline. This type of currents is offshore directed and fairly uniform along the beach (Figure 1.5a) and are responsible for the most of offshore sediment transport during erosive events.

Another type is called longshore currents (Figure 1.5b) which only exist in case of obliquely incident wave (waves approaching the shore with an angle to the shore normal direction), as in this situation the alongshore component of radiation force is not zero. This type of currents present as the main flow that drives the alongshore transport of sediments.

In addition, rip current, a narrow and seaward directed current which extends from the inner surf zone out through the breaking line, is another important type of currents that formed by waves. This type of currents though can be present, in theory, on alongshore uniform sandy beach (Weir et al., 2011), is commonly related to the presence of alongshore inhomogeneity in the seabed bathymetry of sandy beaches. This is because generation of rip currents are highly dependent on the alongshore topographic variation, which tends to cause the wave-induced return flow can shift back out to sea more easily in some special locations (usually the trough area between bumps).

As both rip current and undertow are seaward flows in the nearshore zone, they have been muddled in the scientific literatures during the early stage (Leatherman, 2012). However, these two types of currents are indeed very different. Firstly, rip currents are often confined to the upper column of the water body near the though area, while the undertow currents are omnipresent under breaking waves near the bottom of water column. Secondly, the speed of rip currents is much greater than that of undertow currents. Typically, rip currents can reach up to 1 m/s and it was reported that rip currents at some sites, e.g., Palm Beach in Australia, can reach as high as 2 m/s (Short, 1985). Thirdly, the presence of rip currents is not solely for they are essentially an integral component of nearshore circulation (Figure 1.6). This circulation is originated from some location where the breaking waves deduce an onshore current. This onshore current then deflected into alongshore direction and finally feed into the rip currents. The formed rip currents further move to sea and can return back shoreward. Recent observations using Lagrangian drifters show that there are two types of circulations exist in the nearshore, namely rip current circulation and sinuous alongshore current (MacMahan et al., 2010). Normally, the

rip current circulation is present under normal incident waves, of which the returned currents generated by rip currents can feed to the water body at the origin (Figure 1.6a). The sinuous alongshore current are generally formed under oblique wave incidence and in this case the returned currents feed to onshore current over the bump that are adjacently located at the down-current of the original bump (Figure 1.6b).

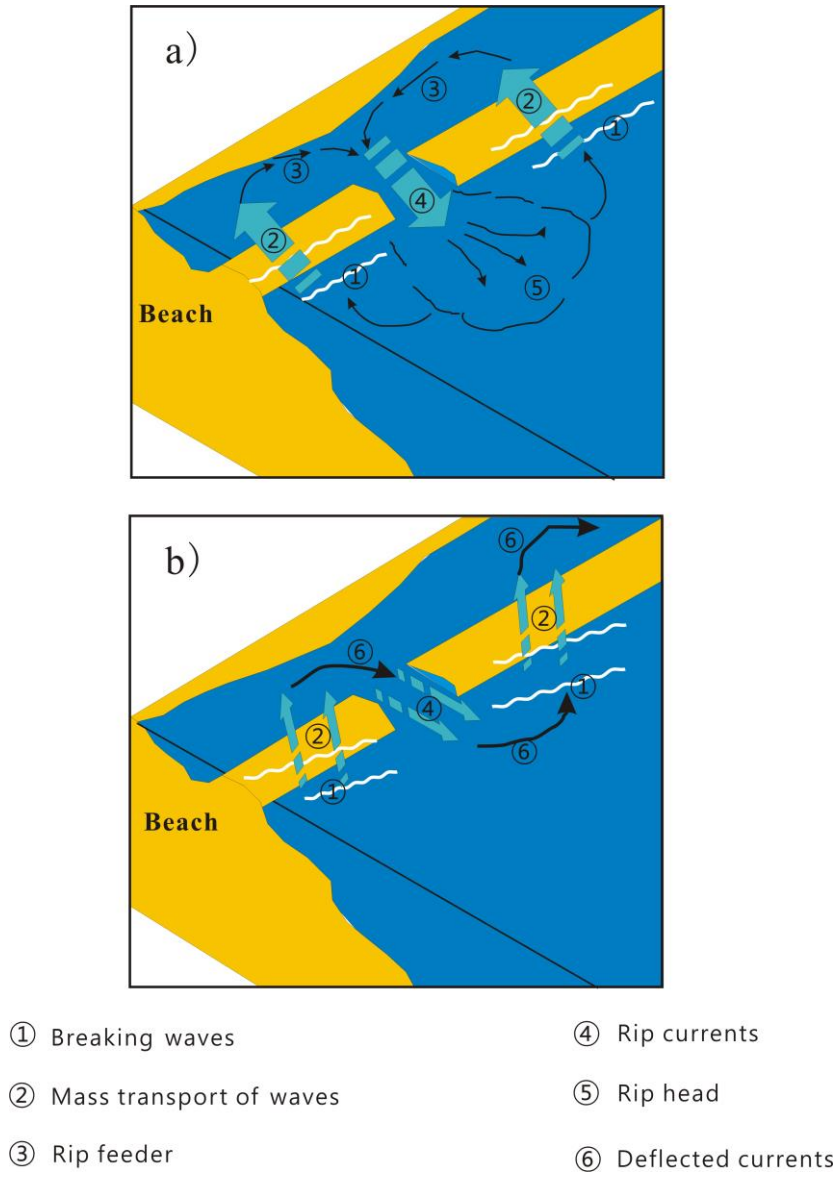

Figure 1.6 Rip current circulations under (a) normal and (b) oblique waves for alongshore non-uniform bathymetry.

1.2.3 Types of wave-dominated beaches

Based on extensive observations from a number of sandy beaches in Australian, Wright and Short (1984) distinguished three basic types of beaches for the wave-dominated sandy beaches, namely reflective beach, intermediate beach and dissipative beach. Table 1.1 gives a comparison of the general properties of these three basic types of beaches, which shows that these beaches differ considerably with each other, as the result of the difference in beach sediment and wave condition (McLachlan and Brown, 2010).

Table 1.1 Comparison of general properties of three basic beaches

Beach type	Dissipative	Intermediate	Reflective
Waves	Infragravity standing waves and bores	Gravity and infragravity waves	Gravity and edge waves
Morphology	Flat, with multiple bars	Variable bars	Deep water inshore
Sand storage	Stored in surf zone	Shifts between surf zone and beach	Stored on beach
Currents	Vertical, bores on surface, undertow below	Horizontal circulation cells	No surf zone, swash circulation within cusps

Reflective beach

Reflective beach (Figure 1.7, right panel is profile view and left panel is planar view) tends to occur under calm waves and/or with coarse sediment, which are generally formed as a result of beach accretion and/or the potential welding of a nearshore bar system. This type of beach often has a steep beach face that allows waves to break close the shoreline and become reflected. The presence of this state often declares

the beach has already fully recovered from the high-energy storm events, as the sediment tend to be stored near the shoreline and backshore. Typical morphological feature on reflective beach are cusps.

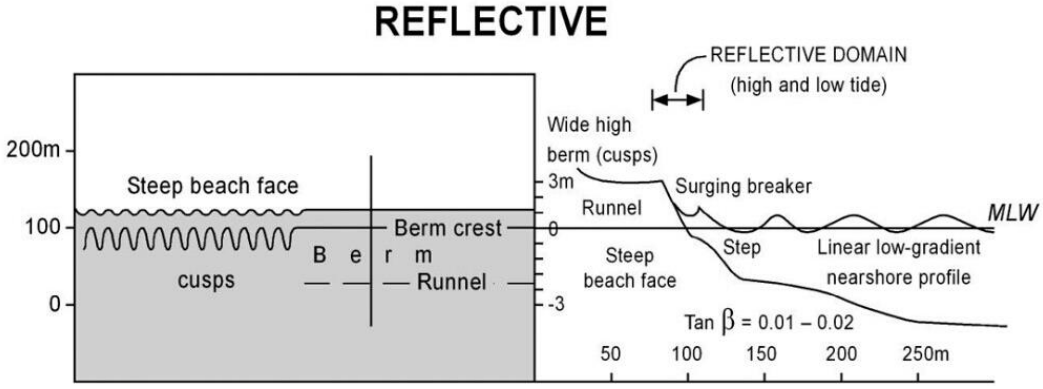

Figure 1.7 Sketch of reflective beach state. Adapted from Short (1999).

Dissipative beach

Dissipative beaches (Figure 1.8) prefer to occur under fierce waves and/or with fine sediment and are, essentially, the opposite of reflective beach states. This state of beach often has a flat beach profile, which tend to make the waves approaching onshore in the form of spilling. This beach state is often found after storm events as a result of beach erosion. When this beach state present, the nearshore sandbar, if exist, will possibly to be migrated offshore, which suggests a relatively low protection ability of sandbars in such a circumstance.

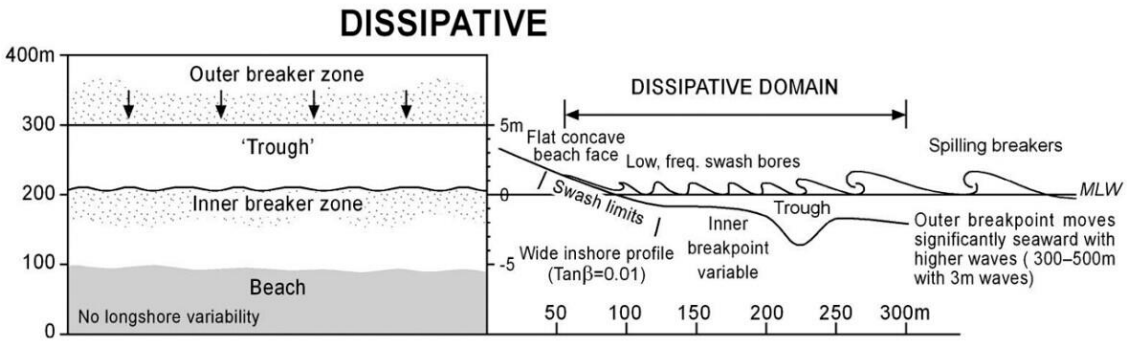

Figure 1.8 Sketch of dissipative beach state. Adapted from Short (1999).

Intermediate beach

Intermediate beaches (Figure 1.9) are the beaches that stay between the reflective and dissipative beach, which can be further divided into four sub-types: 1) longshore bar-trough (LBT), 2) rhythmic bar and beach (RBB), 3) transverse bar and rip current (TBR), 4) ridge-runnel or low tide terrace (LTT). These four sub-types of beaches can be genetically linked, as they are essentially different stages of the same morphodynamic process.

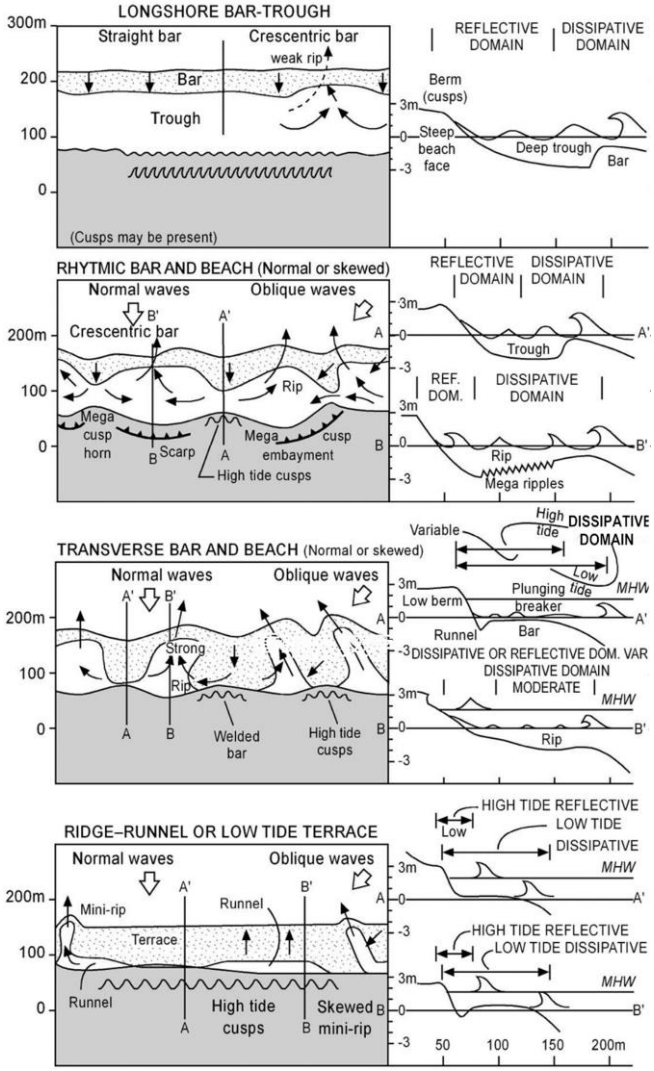

Figure 1.9 Sketch of intermediate beach, which includes four subtypes namely longshore bar-trough (LBT), rhythmic bar and beach (RBB), transverse bar and rip current (TBR), ridge-runnel or low tide terrace (LTT). Adapted from Short (1999).

The LBT beach is characterised by the presence of a straight sandbar that extends in the longshore direction and a deep trough that locates in the shoreward near to the sandbar. This type of beach is usually formed under high energy (storm) events. After the storm subsides, waves become milder, which may lead to the shifting of LBT beach into RBB beach. A typical characteristics of RBB beach is the presence of crescentic bars and megacusp near the shoreline, both of which are alongshore (quasi-) rhythmic. Combining to this morphology patterns, a well-developed rip current circulation can be generated. Under continued mild wave conditions, the RBB beach will further shift towards the TBR beach, as the horns of crescentic bar are now weld onto the shore after continued shoreward migration. Typically, the bars on this beach are perpendicular to the shoreline and are separated by deep rip channels. The current pattern is still dominated by horizontal current circulation, with water moved onshore over bars and strong offshore directed rip current in the trough. The ridge-runnel beach is similar to that of TBR beach, but it occurs in the intertidal zone with the bar or terrace connected to the beach at low tide level. Therefore, the current pattern may differ for high tide water level and mid tide water level. At high tide, the incident waves may break directly on the beach, performing similar to the wave breaking format on the reflective beach. But at mid tide, waves may break on the bar or terrace and thus can generate a rip currents circulation. This sequence of beach states transition and sandbars succession occur in theory. However, in the field, such a transition may be interrupted by the reoccurring of high energy storm, which can ‘resets’ the morphology to the LBT beach.

1.3 Rip channels on sandy beach

The nearly constant evolving seabed in the nearshore zone of sandy beach gives rise to a wide range of morphological features. Among the various of morphological features appear in the nearshore zone of sandy beach, the most striking one has to be the alongshore rhythmic morphological features, which can stretch from the swash

zone to the breaking area, being away from the shoreline with a certain distance (Figure 1.10).

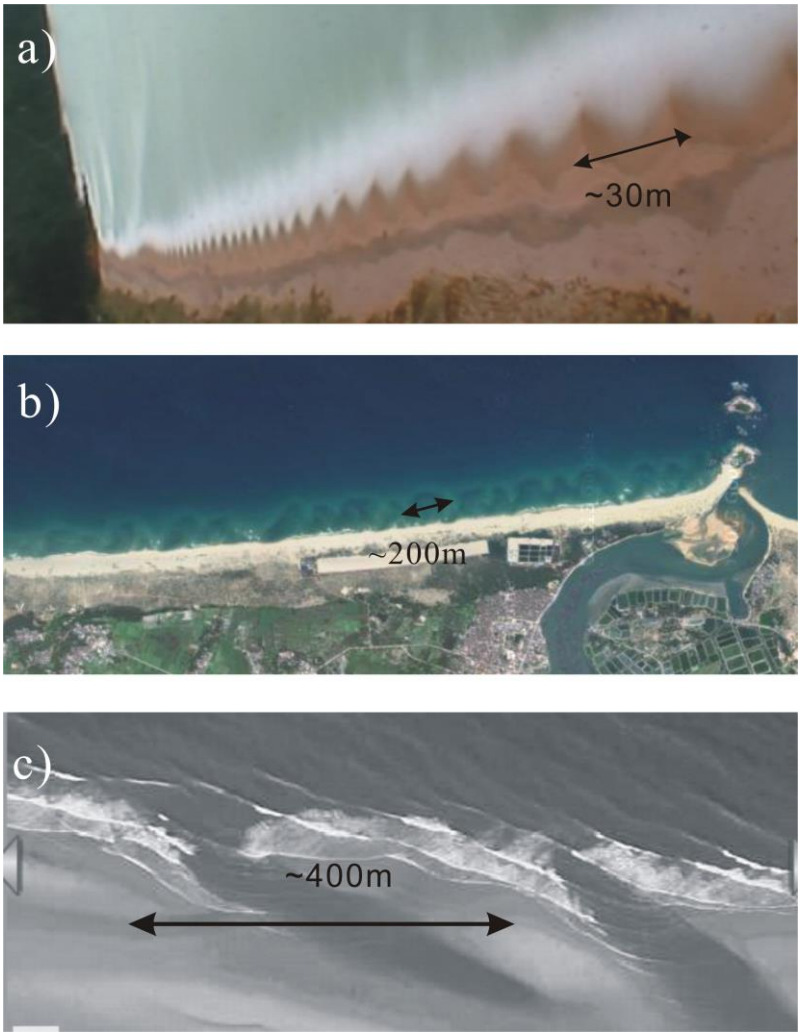

Figure 1.10 Rhythmic morphological features on sandy beaches. a) Beach cusps at Tairua beach, New Zealand (Almar et al., 2008); b) Crescentic bar in Hainan, China; c) Oblique sandbar at Southwest France (Google Earth imagery).

In the swash zone, it is common to see a type of crescent-shaped, concave indentions pattern, which is termed as “beach cusps”. The length scales of beach cusps are generally around 5-10 m in the cross-shore direction and 10-50 m in the alongshore direction. In the inner surf zone, several sand bumps (or bars) may display regularly along the coast with spacing in order of tens to hundreds metres. The orientation of single bump (bar) can be either perpendicular or oblique to the coast. These patterns

are often termed as “transverse/oblique bar system”, which can either appear accompanied with the alongshore uniform sandbar or exist independently. In some situations, these morphological patterns may be attached to the shoreline, generating a feature called “megacusps”. The appearance of megacusps is quite similar with that of beach cusps. However, the length scale of megacusps (around 100-500 m) is larger than that of beach cusps. In addition, the physical processes shape the megacusps are different to that shaping the beach cusps, as megacusps are generated by surf zone processes, while beach cusps appear in swash zone and are developed due to the run up and backwash of waves (Orzech et al., 2011; Thornton et al., 2007). In the outer surf zone (near the breaking line), another typical rhythmic morphological pattern named “crescentic bars” can be formed. The plan view of crescentic bar is alongshore meandering. In the present thesis, the transverse/oblique bar and crescentic bar are collectively called as “rip channel system” or “rip channels”, as they are both alongshore rhythmic morphological features exist in the surf zone and are often linked to the narrow, offshore-directed, jet-like flows called rip currents. Such a concept of “rip channel system” has also been used in the study of Garnier et al. (2008) .

In the field, more than one rip channel system, either being different types or appearing at different locations, may coexist on the same beach. This type of situation has been observed in many fields (Price et al., 2013; Ruessink et al., 2007; Thornton et al., 2007). In such situation, interactions between different rip channel systems may take place (Figure 1.11). For instance, the alongshore spacing of horns and bays of rip channels on the inner sandbar may exhibit the same alongshore characteristics as the shoreline rhythms (Sonu, 1973). Similar relationship can also be observed between the rip channels on inner-bar and that on the outer sandbar under certain conditions (Quartel, 2009; Ruessink et al., 2007). Recently, using a more than 9 years dataset of time-exposure images from the Gold Coast in Australia, Price and Ruessink (2013) developed a comprehensive framework to categorize the observed interaction behaviour among rip channels systems according to the

coupling phase (in-phase or out-of-phase), proceeding sequence of the outer bar (downstate or upstate) and the morphology of the inner bar (terraced or with rips).

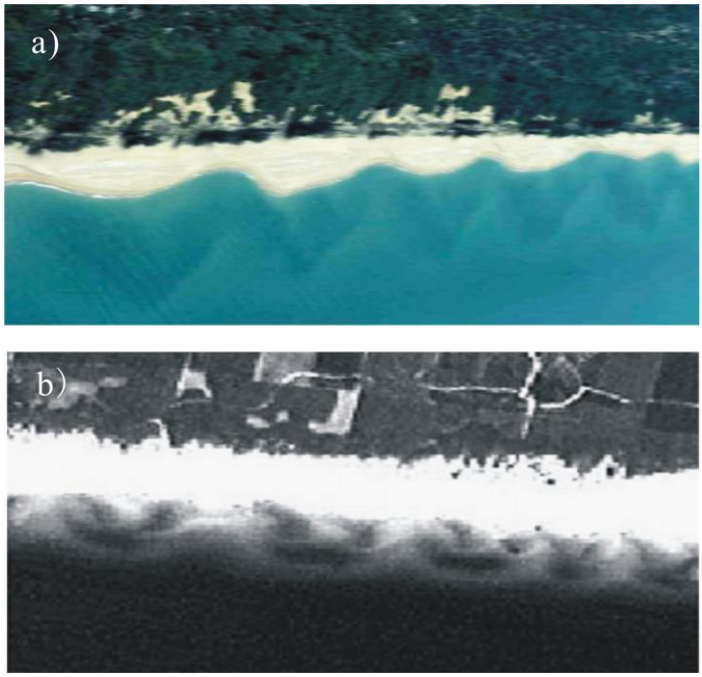

Figure 1.11 Observed coexistence of rip channel systems. a) inner-bar patterns and shoreline undulations on New South Wales Coast, Australia (Castelle et al., 2010a) and b) inner-bar patterns and outer-bar patterns on sandy beach at Aquitanian Coast, France (Castelle et al., 2007).

1.4 Self-organization behaviour of rip channels

On sandy beaches, some morphological features may directly obey the patterns in the external forcing, the behaviour of which is known as forced behaviour. Other patterns, however, do not resemble the similar patterns in the forcing, known as free behaviour or self-organization behaviour (Dodd et al., 2003). A more detailed discussion on these two types of behaviour can be found in the study of Coco and Murray (2007). Until now, both theories that explain the origin of rip channels as result of forced and free behaviour exist, which are named as the forced template theory and self-organization theory. The forced template theory considers that

patterns of the alongshore rhythmic rip channels are inherited from patterns in the flow field that has the same spatial scale as that in the rip channels. The patterns in flow field are often ascribed to the presence of “edge waves” (Holman and Bowen, 1982). A shortcoming of this theory is that no feedback of the seabed to the flow field is taken into account, which is contradicted to what happens in the field. In addition, there is lack of well-established criterion for selection of the frequency and phase of edge waves that are responsible for the growth of observed rhythmic patterns (Wijnberg and Kroon, 2002). Conversely, the self-organization theory emphasized that the template in hydrodynamic forcing is not necessary and the alongshore rhythmic rip channels can emerge from the feedbacks (positive and negative) between flow field, sediment processes and the evolving morphology. Although the correctness of self-organization theory is not that intuitive, it has nowadays been firmly established and widely accepted in the coastal research community (Werner and Fink, 1993), due to the advance in both field observations and numerical simulations.

Unfortunately, until now, it is still not conclusive to say which mechanism is responsible for the formation of rip channels and possibly both mechanism coexist. In the present thesis, however, we will only focus on the self-organization behaviour of rip channels. This is because we notice that the recent numerical studies involving infragravity wave show the dynamical and geometrical properties of rip channels is not that sensitive to the variation of infragravity wave properties (de Schipper et al., 2014; Reniers et al., 2004). This finding suggests that the template in hydrodynamic forcing may have only ignorable effects on the evolution of rip channels.

1.5 Self-organization models for rip channels

In fact, the establishment of self-organization theory is largely as a result of the success in the development of self-organization models. It has been shown by massive of numerical studies that the self-organization models can produce reasonably well prediction of the properties of alongshore rhythmic rip channel

system compared with that observed from the field (Garnier et al., 2006; Garnier et al., 2008; Ribas and Kroon, 2007; Thiébot et al., 2012).

The application of self-organization models to study the self-organization behaviour of rip channels starts from forcing an alongshore uniform wave (thus no template exist in the forcing) on the corresponding alongshore uniform equilibrium seabed. Following this, a perturbation is added on the equilibrium seabed, which will give rise to a perturbed flow field. With the feedbacks between seabed, waves and flows, the perturbation in the seabed will grow and present certain patterns if the positive feedbacks (the magnitude of the initial perturbation increase in the feedback loop) dominate, or the equilibrium seabed stays stable and no pattern will emerge if the negative feedbacks (the magnitude of the initial perturbation decrease in the feedback loop) dominate (see Figure 1.12).

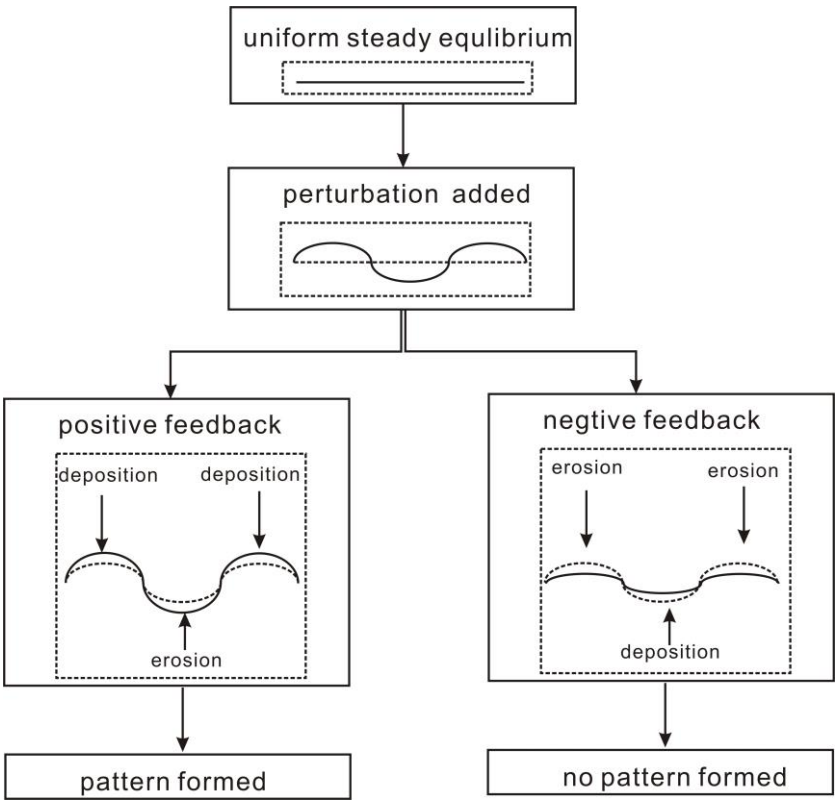

Figure 1.12 Illustration of the self-organization theory, in which the positive feedback promote the growth of bed patterns and the negative feedback prohibit the formation of patterns.

Nowadays, various self-organization models have been developed and are used in studying the emergence and evolution of rip channels (see Figure 1.13). These models can be generally classified into linear and nonlinear models (Dodd et al., 2003).

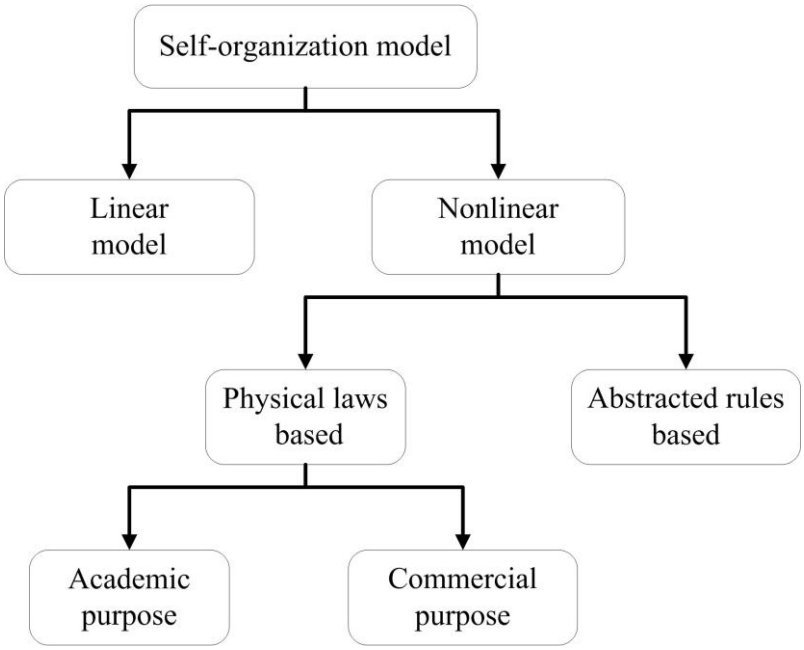

Figure 1.13 Classification of existed self-organization models

The linear models (see, e.g., MORFO60 used by Calvete et al.(2005)), known more commonly as linear stability models, are designed specifically to investigate the initial tendency to grow or decay of the various morphological patterns. Therefore, they are useful to identify positive feedback that is responsible for the observed morphological patterns and can also give the information about the relevant time and space scales. However, the predictions from linear models are not fully comparable to the observations from field as this type of models does not give any information on the actual amplitude of the features.

In contrast with linear models, the nonlinear models are not only able to give the information about the initial growth of morphology, but also able to give the information about the long-term behaviour of the morphological pattern and its finite amplitude. The nonlinear models can be built on either a reduced set of abstracted

rules (e.g., cellular automata model used by Murray(2004)) or the basic physical laws like mass, momentum and energy conservation (e.g., MORFO55 used by Garnier et al. (2008)). Specifically, the latter one is the main type of models that used to study the emergence of alongshore rhythmic sandbars (e.g., Castelle and Ruessink, 2011; Ribas and Kroon, 2007), which can be either adapted from the commercial models or specifically designed for "academic" purpose. Generally, the commercial models often contain complex processes and their uses are usually not free and expensive. On the contrary, the nonlinear models for "academic" purpose are often designed to understanding the underlying mechanisms of sandy beach evolution with only necessary processes included. These two types of models are essentially linked. For example, the knowledge obtained the nonlinear models for academic purpose can provide as guidelines for the setting up the commercial models.

1.6 Motivation and aims

The knowledge on the formation and evolution of rip channels is important because not only do rip channel system significantly affect the evolution of beach and coastline (Orzech et al., 2011), but also the rip currents associated with rip channel system are a serious hazard to beach users and can significantly affect the transport of coastal sediments and dispersion of pollutants. In addition, studying the formation and evolution of rip channels would be undoubtedly an important tool for any numerical models that intend to describe the morphodynamics of beaches, as they are representative natural morphological features appearing on sandy beach and reproducing their dynamical behaviour can be an important test for the numerical models.

Previously, the self-organization models have been used to understand the underlying mechanisms that responsible for the formation and evolution of rip channels and also to evaluate the influence of environment factors (Calvete et al., 2005; Castelle and Coco, 2012; Garnier et al., 2006; Murray, 2004). Largely thanks

to the knowledge obtained from studies that using self-organization models, our understandings on the formation and evolution of rip channels have been significantly improved in the last several decades. However, till now, the effect of sediment grain size on the formation and evolution of rip channel system is still largely unknown. Although previous studies have been carried out to investigate the role of sediment size on rip channels, they are limited to the initial formation of rip channels and considering only normal waves (Calvete et al., 2005). In addition, till now, the self-organization models for studying the formation and evolution of rip channels are based on the assumption of homogeneous sediment, i.e., the grain size of sediment is uniform and constant as the sediment is assumed to be consisted of grains with only one size.

However, the sediment on real sandy beach is seldom homogeneous as actually approximately 80% of the world's non-rocky coastal regions are composed by heterogeneous sediments (Holland and Elmore, 2008), the grain size of which typically exhibit a variation both in spatial and temporal scales. For example, the cross-shore sediment size in the nearshore commonly exhibits a fining trend offshore with mean grain size considered (Komar, 1998; Kulkarni et al., 2004; Wang et al., 1998). Guillén and Hoekstra (1996) obtained an "equilibrium" distribution of grain size fraction based on the field study at Terschelling in Netherlands, with characteristic of a decrease of grain size diameter from shoreline to closure depth. As to the rip channel system, sediment size is also not uniform and constant. MacMahan et al. (2005) found the surface sediment size varies in rip channels system, with coarser sands in deep rip channels and finer sediments in shoals. The similar pattern of grain size distribution was also found by Gallagher et al. (2011) through detailed analysis on the high resolution data of sediment size in a rip channel system. Furthermore, Gallagher et al. (2011) found that the pattern of sediment grain size changes temporally with the dynamic seabed bathymetry.

The assumption that the heterogeneous sediment on sandy beach can be represented by single homogeneous sediment should be only valid when the actual dynamics of rip channels are either similar to those within an environment comprised of uniform

sediment or equivalent to the linear summation of dynamics determined for individual grains.

However, a large number of previous studies show that the dynamics for environment with heterogeneous sediment is quite different to those in uniform environments. Foti and Blondeaux (1995) investigated the sea ripple formation when the bottom is made up of a mixture of sands. Their results show that the presence of heterogeneous sediment tend to stabilize the sea bed and generate ripples with longer wavelength. Walgreen et al. (2003) developed a linear model to study the formation of shoreface-connected ridges and they found the mixture of sediment also have a net stabilizing effect on the growth of bedforms as the growth rate decreases when sediment mixture considered. Moreover, they found the migration rate of the shoreface-connected ridge increase and the preferred wavelength become longer. Walgreen et al. (2004) investigated the effect of heterogeneous sediment on the formation of tidal sand ridges. Their results show that the growth rate and migration increases when the mixture of sediment are considered, whilst the wavelength of the ridges remains unchanged.

The aim of the present thesis is to investigate the effect of sediment size and its distribution on the formation and evolution of rip channels under the framework of self-organization. This knowledge is necessary to understand the dynamical behaviour of rip channels and is also necessary for inter-site comparison of field observation databases for rip channels from different beaches and to explain the inter-site differences in the observed dynamical behaviours. To this end, a self-organization model based on the open source program XBeach (Roelvink et al., 2009) is developed, tested and used.

The research questions that summarize the objectives of the present thesis are listed below:

1) What is the role of sediment size on the formation and evolution of rip channels, in case the beach is consisted of homogeneous sediment?

2) What is the influence of heterogeneous sediment on the characteristics and dynamical behaviour of rip channels?

3) Whether the heterogeneous sediment can be roughly instead by the homogeneous sediment that with the same mean grain size? If this is possible, in what situation this reduction can be used?

1.7 Outline of thesis

The thesis is arranged as follows. Chapter 2 gives a comprehensive review of literature that relate to the formation and evolution of rip channels. Chapter 3 describes the self-organization model used in this thesis, which is adapted from the XBeach model. Specifically, the governing equations, the processes parameterization and the boundary conditions are described in detail. Especially, the details on how to adapt the original XBeach model into the self-organization model used for the present study are emphasized. Chapter 4 is dedicated to test the performance of the adapted XBeach model, with a detailed comparison of the prediction for the formation and evolution of rip channels from the adapted XBeach model and previous numerical studies and field observations is displayed. Chapter 5 investigates the influence of grain size of homogeneous sediment on the properties and dynamical behaviour of rip channel system. Chapter 6 investigates the influence of heterogeneous sediments on the behaviour of rip channel system and the coupling behaviour among transverse bar system near the shoreline and crescentic bar system in the breaking zone. Chapter 7 gives conclusions for the work in this thesis and recommendations for the future researches.

Chapter 2

Current understanding on the morphodynamics of rip channels

2.1 Introduction

There is no doubt that our understandings on the morphodynamics of rip channels have been significantly improved in the past several decades. However, a comprehensive understanding is still to be far from complete. Before beginning to investigate the effect of sediment size and its distribution on the dynamics of rip channels, it is best to comprehensively review the previous works in literatures that concern on the emergence and development of rip channel system. Such a comprehensive review would help us to better position the potential contribution of the present thesis on the knowledge map that concerns to the dynamics of rip channel system. This comprehensive literature review will be given in this chapter, in which the advance in both field observations and numerical simulations on rip channel systems will be overviewed. Specifically, we will firstly take a brief look at the field observations on rip channel system, where both the observation/measurement technology and the relevant observation results are introduced. Then a detailed overview on the previous modelling studies for the formation and evolution of rip channel systems is carried out, in which qualitative comparison between the field observation and modelling simulation are given as well. Finally, a brief summary on the findings obtained from the comprehensive review will be given.

2.2 Field observations

2.2.1 Observation techniques

Nowadays, many techniques exist in monitoring the evolution of rip channel system as well as the nearshore zone processes that related to its evolution, with the factors monitored by which include such as waves, currents, seabed morphology and grain size of seabed. Commonly, the wave properties (wave height, period, direction) are measured using the pressure sensor (Austin et al., 2009), the currents are measured using the velocity sensor (MacMahan et al., 2005). These sensors can be either mounted on moving carriers like ships and amphibious vehicles, or installed on a fixed point of seabed to provide excellent data of the hydrodynamic forcing. The seabed bathymetry is traditionally measured using total station or echo sounding technique, in which the coordinates of a great amount of individual locations need to be measured in order to obtain the whole seabed bathymetry. Due to such technique is cumbersome and labour intensive, long-term and high-resolution beach morphological data sets are sparse (Southgate et al., 2003).

However, the availability of high quality morphological data sets have now significantly improved as the advent of remote sensing techniques, in particular, the introduction of Argus imaging technique (Lippmann and Holman, 1989). The work principle for Argus imaging system is that the images of sea surface captured by the Argus system can record the foam and turbulence produced by the wave breaking as patches of high intensity. By averaging the pixel values of a number of different images at certain intervals, the alongshore distribution of location of submerged sandbar and the curving alongshore shape of the sandbar can be revealed, which is in consist with the smooth high-intensity band of pixels on averaged Argus image. Due to the Argus imaging system can continually monitor the beaches, the change of seabed bathymetry with both high resolution in time and space scale can be obtained.

Similar to the measurement of seabed bathymetry, the traditional method for measuring the grain size of sediment on beach is tedious and time consuming. Traditionally, sediment size can not be measured in field but need to be measured in

laboratory, using the sediment samples that collected from the field. In laboratory, the sediment samples need to be dried first. Then the dried sediment samples need to be sieved using a number of griddles with different meshes. Usually, for each sediment sample, 10 minutes are needed to separate the sediment with different size through shaking the sample in the griddles. The separated sediment groups will then be weighted individually with the measured weight data are used to calculate the mean grain size of sediment. However, in recent, the efficiency for measuring the grain size of beach sediment has been improved largely due to the presence of digital imaging system (DIS). By using the digital imaging system, sediment samples are not needed to be collected from field, as the information about grain size of sediment can be stored in the format of images. The grain size of sediment can be easily estimated using digital image processing technology. Therefore, a large number of samples, in the form of image, can be collected easily, which allows for high spatial and temporal resolution surveys of sediment size on beaches (Gallagher et al., 2011).

2.2.2 Field observation on individual rip channel system

Benefit from the improvement of numerous observation techniques used in monitoring the sandy beaches, field observations on the morphodynamics of rip channel system have been enriched unprecedentedly in the last several decades. Until now, the seabed bathymetries of rip channels and the current circulation associate with the rip channels have been recorded in a wide range. From the Argus images, the alongshore rhythmic rip channel systems have been observed on beaches world-wide, including such as Duck beach at USA (Konicki and Holman, 2000), Perranporth beach at UK (Scott et al., 2007), Tairua beach at New Zealand (Gallop et al., 2011), Gold coast beach at Australia (Price and Ruessink, 2011), Gironde coast at southwest of France (Lafon et al., 2005), Noordwijk aan Zee at Dutch (Quartel, 2009), Monterey bay at USA (Orzech et al., 2010). Typically, the observed alongshore characteristic length of rip channel system in field is between $O(10)$ and $O(1000)$ m, with the alongshore characteristic length of rip channels may vary alongshore on a specific beach.

The current circulation coupled to the underlying bathymetry of rip channels have been observed on many beaches including both open beach (Scott et al., 2007) and embayed beach (Short, 1999), which is measured using fixed velocity instrumentation (Ferrer et al., 2011). Recently, the Largrangian behaviour of current circulation that related to the rip channels have been investigated using GPS tracked drifters (Austin et al., 2009; MacMahan et al., 2010). With using such drifters, our understanding on the behaviour of water exchange in rip channels has been significantly improved.

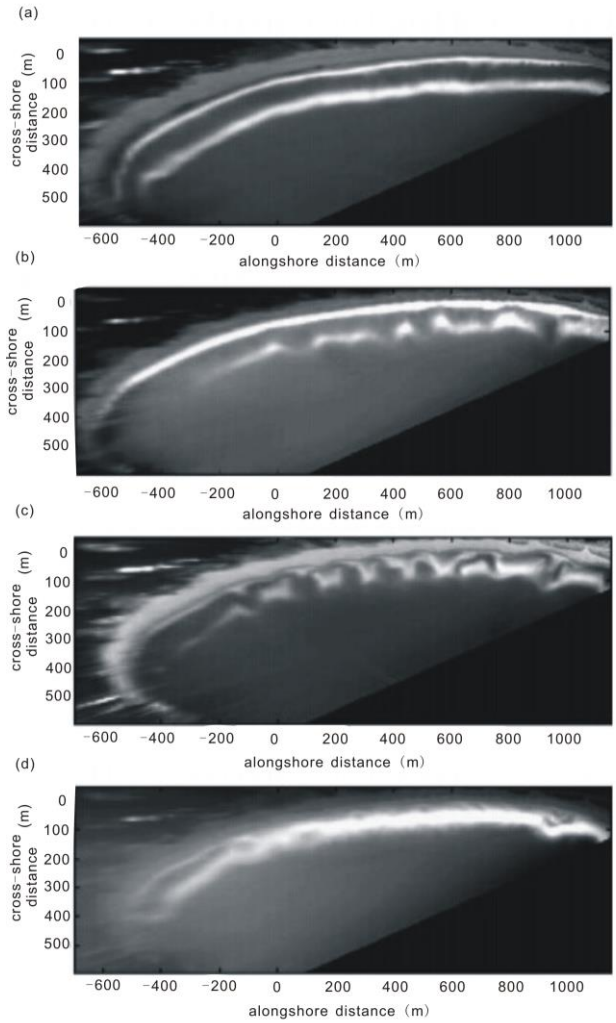

Figure 2.1 Four time exposure images of different intermediate beach states at Palm Beach. (a) LBT on 8th May 1996, (b) RBB on 15th May 1996, (c) TBR on 25th May 1996, and (d) LTT on 11th June 1996. Adapted from Ranasinghe et al. (2004).

Moreover, field observation also shows that the rip channel system in field is quite dynamic as it evolves continuously. The most typical example of such variation is emerging and disappearing of rip channels, as well as the transition between different types of rip channel morphologies. It has been observed that the rip channel system is common to be disappeared and replaced by shoreline-paralleled linear sandbar when the storms occur (Lafon et al., 2005; Ribas and Kroon, 2007). This linear sandbar has also been observed to migrate in the cross-shore direction, i.e., offshore migration under high wave conditions and onshore migration during mild waves (Gallagher et al., 1998). An emergence event of rip channels that occur at Palm Beach is given in Figure 2.1, which can be deduced by comparing Figure 2.1b and Figure 2.1a. It can be seen that after about 7 days evolution, the initial alongshore uniform sandbar evolves into crescentic bar. This initially emerged crescentic bar continues evolve and subsequently transmits into the transverse bar system after another 10 days evolution. This can be seen by comparing the Figure 2.1b and Figure 2.1c. Finally, the transverse bars merge with the shoreline and form the ridge-runnel type beach. Essentially, Figure 2.1 gives an example of the full transitionary cycle among different type of immediate beaches.

Besides these morphodynamic behaviour, there are also some other morphodynamic behaviours observed in field. For instance, splitting or merging of individual rip channel may take place (Figure 2.2), which seems attempt to make the rip channels turn into a more uniform pattern, as splitting is usually confined to the longest rip channel unit, whereas the merging usually occur on the smallest rip channel unit (van Enckevort et al., 2004). Moreover, the rip channel system are often observed to migrate in the alongshore direction when waves come oblique with respect to the shoreline (Orzech et al., 2010; Ribas and Kroon, 2007).

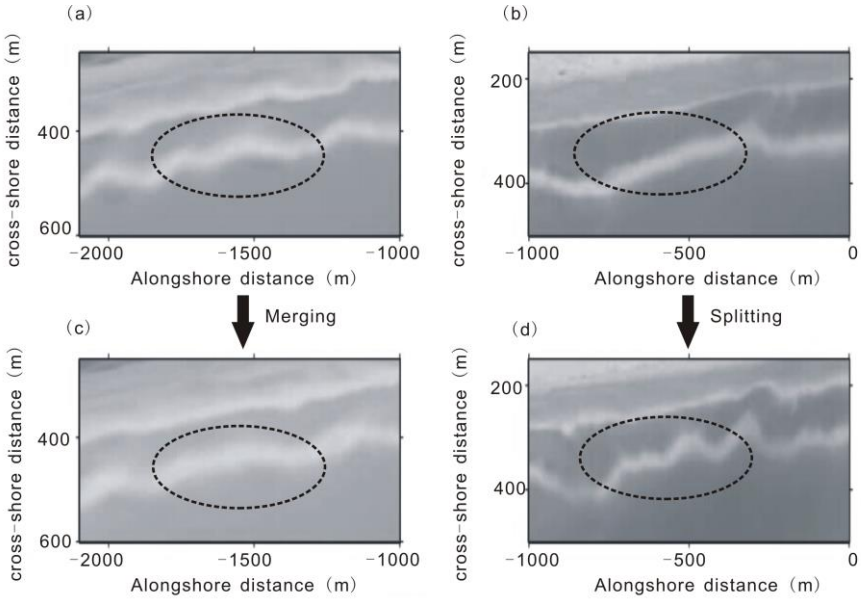

Figure 2.2 Merging (left) and splitting (right) of rip channels, observed on the Gold Beach, Australia. Adapted from van Enckevort et al. (2004).

Not only give the qualitatively information on morphodynamic behaviour of rip channels, the field observations also give quantitatively information on the development of rip channel system. For instance, the formation timescale of rip channels can be estimated from the Argus images, which approximately is equal to the residence time of LBT beach. Table 2.1 shows the residence time of different types of beaches at Palm Beach and Duck Beach as reported by Lippmann and Holman (1990) and Ranasinghe et al. (2004) respectively. Using 523 days of visually classified Argus time-exposure images obtained at Duck Beach, USA, Lippmann and Holman (1990) reported that the mean residence time of longshore uniform sandbar at the LBT beach is about 2.5 days, while Ranasinghe et al. (2004) reported that the mean residence time of longshore uniform sandbar at the LBT beach on Palm Beach, Australia is about 5.4 days and is more than two times of that observed for Duck Beach. This shows that the formation timescale of rip channels can be significantly different for different beaches.

Another commonly reported quantitative indicator for the development of rip channel system is migration speed of rip channels. Similar to the formation timescale,

the reported migration speed is also quite different among different monitoring site. By examine the video images obtained from Egmond in Netherlands, Ruessink et al. (2000) reported that the migration speed is up to 150 m/day at this site. By tracking the trajectory of the daily rip locations, Holman et al. (2006) found the root-mean-square migration speed is 17.1 m/day at Palm Beach. This migration speed is similar to that observed on Duck beach (Sallenger et al., 1985).

Table 2.1 Residence time of different types of wave-dominated beaches at Palm Beach and Duck Beach

Beach types	LTT	TBR	RBB	LBT
Palm Beach (days)	9.3	22.8	11.8	5.4
Duck Beach (days)	18	7.2	4.7	2.5

* This table is adapted from Ranasinghe et al. (2004).

Given the increasing availability of dataset on the morphodynamic properties of rip channels and the corresponding measured environment factors, massive field observations have also tried to link the morphological and dynamical characteristics of rip channel system to the incoming wave conditions (Holman et al., 2006; Ruessink et al., 2000; Turner et al., 2007) and the geometry characteristic of beach profile (van Enckevort et al., 2004). However, satisfactory predictors for the morphodynamic properties of rip channels is still not yet been proposed. For instance, the wavelength of rip channels usually increases with the wave height, the distance from the shoreline to the bar crest. In addition, this value has also been suggested to related with the water depth above the bar and bed slope (Short, 1979). But, such relationships are not universally applicable, as they are not clear from field observations in some sites. For example, Holman et al. (2006) found the mean rip spacing in Palm Beach is poorly correlated with the bar crest distance from the shoreline. Lafon et al. (2005) reported that the wavelength of rip channels in their observations on Truc Vert beach in France decrease when wave height increase.

Using three years of video-based data of a rip channel system, Turner et al. (2007) also found no correlation between the observed wavelength of rip channels and the offshore wave height, period or energy. The similar problem occurs in establishing a universal relationship for the migration speed. In more detail, although the migration speed is often found to depend on the offshore wave angle or its equivalent indicator, i.e., the longshore component of the offshore wave energy flux (Ruessink et al., 2000), this correlation is not that high as the events of odd migration rate were common to be observed. An extreme example of this situation is that the migration direction even can be not consistent with the prevailing offshore wave angle and resulting alongshore current (Turner et al., 2007).

2.2.3 Field observation on the coupling between rip channel systems

The observations on the coupling behaviour of rip channel systems have also increased significantly. Ruessink et al. (2007) observed that the alongshore spacing of horns and bays in the inner sandbar may exhibit the same alongshore characteristics as that in the outer sandbar under certain conditions. Similar relationship can also be observed between inner-bar patterns and shoreline rhythms (Castelle et al., 2012). More recently observations showed that the configurations of the coupled morphological patterns in the sandy beach are diverse in terms of the coupling length, coupling phase and dynamic characteristic of the entire beach. Castelle et al.(2008) found that for low-energy wave conditions and large outer-bar wavelength the inner-bar may couple at half rather than same of the outer-bar wavelength. Quartel (2009) observed that the phase of coupling between the intertidal morphological feature and the subtidal alongshore variability can varied from in-phase, where the horn of subtidal bar facing a shoreward perturbation of the intertidal barline, to out-of-phase, where the horn of subtidal bar facing with a seaward bulge in the intertidal barline, with the gradual phase transition due to different alongshore migration speed of bars. Price and Ruessink (2008) recently analyse a more than 9 years dataset of time-exposure images from the Gold Coast in Australia. They distinguished five types of coupled sandbar patterns based on the

coupling phase (in-phase or out-of-phase), proceeding sequence of the outer bar (downstate or upstate) and the morphology of the inner bar (terraced or with rips).

2.3 Modeling the formation and evolution of rip channels

2.3.1 The morphodynamic behavior of simulated rip channel system

In the last two decades, a great number of numerical studies using self-organization models have been carried out to investigate the formation and evolution of individual rip channel system. Generally, these simulations have been able to reproduce well of the observed morphodynamic behaviour of rip channels, including such as the merging and splitting of individual sandbar (Castelle and Ruessink, 2011), the transition from "Rhythmic Bar and Beach" to Transverse Bar and Rip morphology (Garnier et al., 2008). Moreover, the predicted wavelength of rip channels is in consistence with that observed from the field, e.g., Ribas and Kroon (2007) predicted the dominant wavelength of transverse/oblique sandbars is around 20-70 m and Calvete et al. (2005) predicted the dominant wavelength of crescentic bar is around 50-1000 m, both of which are well in the range of $O(10)$ and $O(1000)$ m as observed in field.

These numerical studies have improved our understanding on the growth and kinematics of rip channels, as they are essential in two aspects: 1) unravelling the underlying mechanisms that are responsible for the observed behaviour of rip channels, and 2) exploring the role of different environment factors (Castelle and Coco, 2012; Castelle and Ruessink, 2011; Garnier et al., 2006; Garnier et al., 2008). A typical example to demonstrate the ability of numerical simulations on explaining the observed behaviour of rip channels is the study that carried out by Castelle and Ruessink (2011). By considering the time-invariant waves, Castelle and Ruessink (2011) found that the rip channels can migrate alongshore with a net distance when the time-averaged wave angle is equal to zero. This finding gives a reasonable example on why in some site that the migration speed of rip channels is poorly

related to the offshore wave conditions, which can be explained as the result of cumulative effects that caused by the mismatch between wave conditions and the orientation of rip channel morphology. As to exploring the effects of environment factors on the properties of rip channels, previous numerical modelling have been employed to test the influence of wave height (Garnier et al., 2008), wave period (Calvete et al., 2005), wave angle (Garnier et al., 2013), tide (Durbarbier and Castelle, 2011), time-varying waves (Castelle and Ruessink, 2011), offshore bathymetric anomaly (Castelle et al., 2012) and embayed shoreline (Castelle and Coco, 2012).

A great number of attentions have been paid on investigating the influence of factors on the rip channel wavelength, which has been taken as a diagnostic indicator for the rip channels. Under constant waves, the numerical simulations show that the wavelength of rip channels generally increases for increasing wave heights and wave angles (Calvete et al., 2005). Moreover, it is also found that the characteristic of the initial cross-shore profile can have an important influence same as that of wave conditions on the wavelength of rip channels (Calvete et al., 2007). By considering the time variant wave conditions, Smit et al. (2012) further pointed out that the geometrical properties of rip channels not only dependant on the morphology, but also on the response time to hydrodynamic conditions. This is because the response time of rip channel system is much larger compared to the variability of the hydrodynamic conditions, thus the developed rip channel does not follow closely the concurrent offshore wave conditions (Smit et al., 2008). This suggests that to predict the wavelength of rip channels close to that observed from field, the whole morphological processes may need to be taken into account, i.e., the proper prediction on the temporal evolution characteristic of rip channels is essentially needed. Tiessen et al.(2010) emphasized that applying an algorithm that considering the formation timescale of sandbar (with the proxy growth rate used) can yield predictions from linear stability model closer to observations.

As for the temporal evolution characteristic of rip channel, some aspects need further attention. First, the proxies used to describe the formation timescale of rip channel

are various and not the same for different models. Usually, the timescale proxy used to describe the formation timescale of rip channels in the linear stability model is e-folding time, i.e., the time it takes for the initial perturbation to attain amplitude equal to *e*- times of the initial perturbation amplitude (Falqués et al., 2000). In nonlinear models, the timescale related to the formation timescale of rip channels are often calculated from the temporal evolution trajectory of bed level. Typical indicators of that used in the non-linear models include the growth rate (Garnier et al., 2008), response time (Smit et al., 2008) and saturation time (Castelle et al., 2012). The response time is defined as the time that the growth rate starts to decrease and the saturation time is defined as the time the growth rate decreases to be nearly zero. Second, due to the various proxies used for the formation timescale of rip channels, a direct comparison between different studies is difficult. However, within the same model concept, the relative variation of rip channel formation timescale with response to different environment factors can be found in many studies. In general, the growth rate of rip channels increases with increasing wave height and decreases with increasing wave angles (Garnier et al., 2008; Garnier et al., 2013). Jiménez et al.(2014) suggested the formation timescale of rip channels may be dependent on the wave energy. In particular, rip channels need longer time to develop in low energy waves. Smit et al. (2008) and Drønen and Deigaard (2007) found that the active cross-shore sectional volume of sandbar or the slope of sandbar can significantly impact the growth time of rip channels. Third, the predited formation timescale of rip channels is quite different among different models. For example, under the same model configuration, the e-folding time predicted by nonlinear model MORFO55 can be two times as that by predicted by linear model MORFO60 (Falqués et al., 2008). At last, it seems that the predicted growth time of rip channel is much wider to that observed in the field (Calvete et al., 2005), as the timescale predicted by numerical simulations ranged from 0.5 to 30 days, while it is around 1 to 3 days in field as suggested by van Enckevort et al. (2004). Recently, this mismatch has been explained as the result of the assumption that used in the models, such as neglecting the influence of initial bedforms (Tiessen et al., 2011). However, this mismatch

could also been resulted by other model assumptions, e.g., the grain size is assumed to be uniform in all previous simulations.

2.3.2 The modeled coupling behavior between rip channel systems

The morphological coupling between rip channel systems on sand beaches has already been the subject of several numerical studies. The first such study was carried out by Garnier et al. (2007), who explored the coupling behaviour between transverse bar attached to the shoreline and crescentic bar at the breaking are by using the 2DH morphodynamic model. A comparable situation on double barred beach was analyzed by Castelle et al. (2010a) , in the study of which the normal incident waves were considered as well. Castelle et al. (2010a) found the coupled inner bar features are arisen from the rip-cell circulations that depend on the outer bar geometry and the incident wave height. In this case, the rip-cell circulations that enforced on the inner bar are driven by alongshore variability in wave refraction and wave breaking across the crescentic outer bar. This type of coupling mechanism is also termed as “bedsurf” coupling (Falqués et al., 2000). Be different from Castelle et al.(2010a), Thiébot et al. (2012) performed simulations with obliquely incident waves and showed that the wave direction is also crucial to the morphological coupling on the double sandbar system. This conclusion supports the conclusion found by Price et al.(2007), who showed that the presence of Idt coupling (In-phase coupled with the outer bar proceeded downstate and the inner-bar morphology was terraced) is related to the obliquely incident waves. Under oblique wave conditions it is the magnitude and meandering nature in the alongshore currents rather than the rip-cell circulations stimulate the morphological coupling, which is different to the mechanisms under normal wave conditions. Fundamentally, both these two mechanisms are results of the joint action of gradients in sediment concentration and the waves and thus the resulting current flows.

Overall, all these studies attempted to demonstrate the possibility of potential coupling among different sandbars and to explore factors that affect the different coupled patterns. However, no attempt was made to investigate how long it takes for

the sandbars on beach to develop into coupled patterns and what factors influence such a coupling timescale.

Considering that the morphological coupling is indeed interplay among different sandbars, it is therefore reasonable to expect that the behaviour of morphological coupling would be highly related to the dynamics of individual morphological feature. This is affirmed by the findings of previous numerical study conducted by Thiébot et al.(2012). They found that that the relative length of formation timescale of outer- and inner-bar are important to the morphological coupling on a double-barred beach, with the coupling occurs when the outer-bar grow faster than the inner-bar. If go one step further, it is reasonable to expect that the coupling timescale is somehow dependent on the formation timescale of the individual sandbar.

2.4 Summary

In this chapter, the present understanding on the morphodynamics of rip channels have been overviewed. Due to the advance achieved both in the field observation and numerical simulations, our understanding on the rip channel system do have been improved significantly. Most importantly, it is recognized that the observed properties of rip channels in field are not only dependent on the wave conditions, but also on factors like the antecedent morphology and the temporal scale of rip channel growth, as the rip channels are determined by the whole morphological processes. This suggests that the proper estimation of the temporal evolution properties of rip channels is significantly important. However, the temporal evolution properties of rip channels are not well understood in the present stage as the predicted growth time of rip channels seems to agree not well with the field observation. Moreover, the proxies used to describe the growth time of rip channels are various, which prohibits an inter-model comparison. With respect to the individual rip channel system, understanding on the timescale for the temporal evolution of coupling between different rip channels is still nearly blank. Therefore, further research on these aspects are needed.

Chapter 3

The numerical model: modification of XBeach

3.1 Introduction

The XBeach model (Roelvink et al., 2009) is an open-source, process-based numerical model, developed by the joint efforts of UNESO|IHE, Delft University of Technology and University of Miami. It consists of coupled modules for simulating waves, currents, sediment transport and bed level changes based on a set of depth-averaged flow equations, which consist of the wave action balance equation, the water mass conservation equation, the momentum conservation equation, and the sediment mass conservation equation. The numerical implementation of XBeach model is mainly first order upwind, which in combination with an explicit finite difference staggered grid makes the model robust. The model utilizes an automatic time step of calculation based on Courant criterion and allows the output time step being fixed or fixed by user.

Originally, the XBeach model is designed specifically as a robust modelling tool for assessing the erosion of sandy beach from extreme weather condition (Roelvink et al., 2009). However, the application of XBeach model has been broadly extended in the recent years by modifying the module/sub-module in the XBeach model. For example, McCall et al. (2014) conducted a numerical study for the storm hydrodynamics on gravel beaches using a modified XBeach model, in which a non-hydrostatic pressure correction term and a groundwater model that allows infiltration and exfiltration through the permeable gravel bed is added. Almost at the same time, Jamal et al. (2014) also added a sub-module for simulation of infiltration and exfiltration process to the XBeach model. Using this modified XBeach model, Jamal et al. (2014) investigated the morphodynamic evolution of a gravel beach.

In the present thesis, the XBeach model is modified to serve as a tool for investigating the self-organization behaviour on sandy beach. Although massive numerical models have been developed for studying the self-organization behaviour of rip channels, they are commonly only used by limited researchers and not available to public. In addition, these numerical models have not been widely validated using the experiment data and field observations. Comparing to these models, the XBeach model is open source and has been tested using massive laboratory experiments and field observations (Orzech et al., 2011; Roelvink et al., 2009; Vousdoukas et al., 2012).

A comprehensive description of the modified model will be given in the following, where the modifications will be emphasized. Specifically, the modification of XBeach model includes allowing excluding the three dimensional cross-shore processes, adding a periodic boundary condition in the lateral boundaries, adding a non-flux condition in the shore boundary and adding a new breaking model. In section 3.2, the main modules of XBeach model and the links between them will be introduced. In section 3.3, the formulations of governing equations are given. Section 3.4 presents the expression for the variables included in the governing equations. Section 3.5 deals with the staggered grid and boundary conditions.

3.2 Calculation procedure of XBeach

There are four main modules in the XBeach model, namely wave module, current module, sediment transport module and morphology module. Figure 3.1 outlines these four different modules and gives an illustration on the calculation procedure of XBeach model. This procedure starts from a given initial bathymetry and a specified offshore wave boundary condition. The waves that imposed at the offshore boundary then propagate toward the shoreline, process of which is determined by the wave action balance equation and calculated in the wave module. The flow module uses the radiation stress gradients obtained from the wave modules as the driving term to calculate current field according to the shallow water equation. The generated

current fields in combination with the equilibrium sediment concentration calculated in the sediment transport module determines the gradient of sediment transport. The derived sediment transport gradient is then used to calculate the evolution of seabed (deposition or erosion) according to the sediment mass balance equation. The evolved seabed then returned feedbacks on the physical processes inside the wave and currents module, such as wave transformation and current convergence.

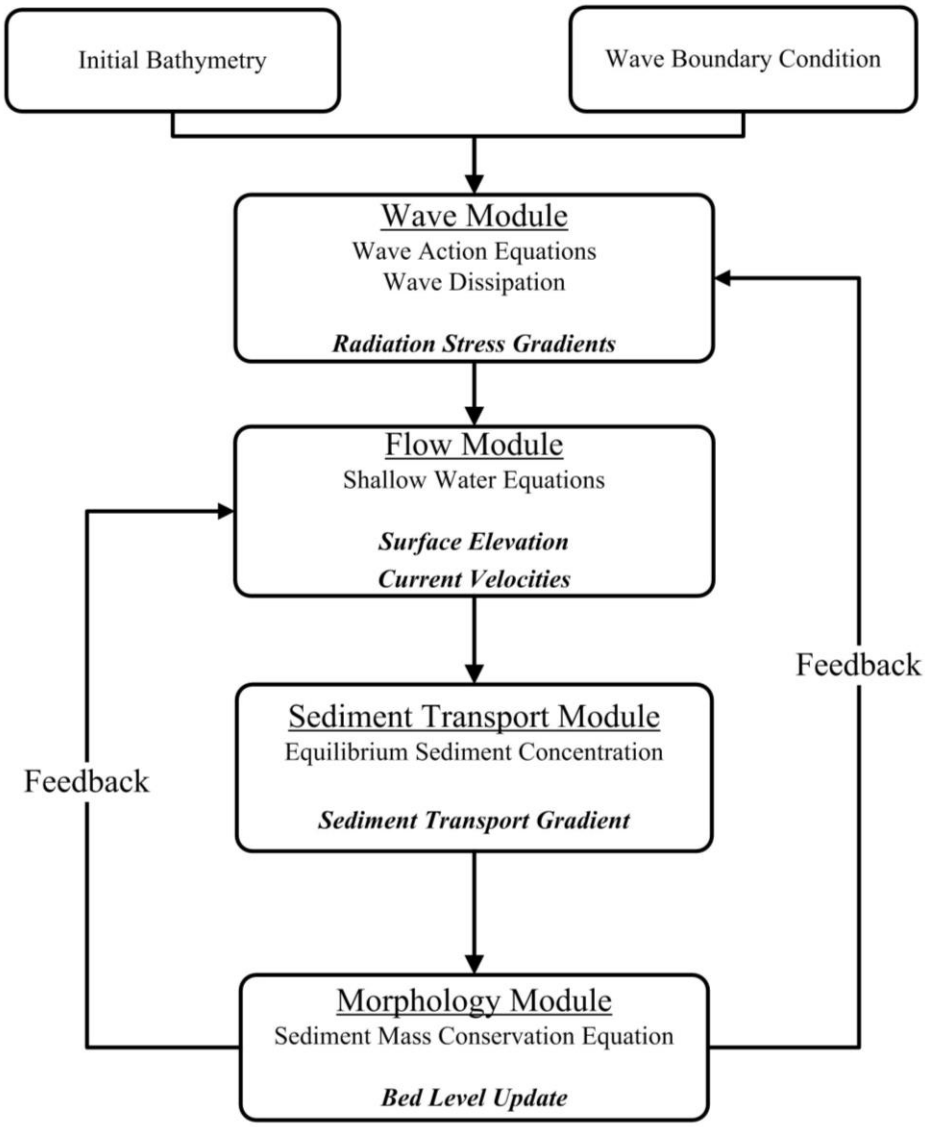

Figure 3.1. Computation procedure of the XBeach model. The underlined terms indicate the main modules included in XBeach model. The terms in bolded Italics indicate the main output of each module.

3.3 Governing equations

3.3.1 Wave-action balance equation

The wave fields and resulting radiation stress are computed from the time dependent wave-action balance equation. Similar to the HISWA (Hindcasting Shallow Water WAves) model developed by Delft University of Technology (Holthuijsen et al., 1989), The XBeach model takes the directional distribution of the wave-action density into account, but uses a single representative frequency to represent the frequency spectrum. The wave-action balance is then given by:

$$\frac{\partial A}{\partial t}+\frac{\partial c_x A}{\partial x}+\frac{\partial c_y A}{\partial y}+\frac{\partial c_\theta A}{\partial \theta}=-\frac{D_w}{\sigma}, \tag{3.1}$$

where t, x, y, θ represent the temporal, spatial and directional dependencies, c_x, c_y, c_ϑ is the wave celerity in x-, y-, θ- space respectively, D_w is the wave energy dissipation in each directional bin and the wave action,

$$A(x,y,\theta,t)=\frac{E_w(x,y,\theta,t)}{\sigma(x,y,t)}, \tag{3.2}$$

is the ratio of wave energy density in each directional bin E_w and the wave frequency σ.

The propagation speeds of wave action in x- and y- direction are calculated as

$$c_x = c_g \cos(\theta)+u, \tag{3.3}$$

$$c_y = c_g \sin(\theta)+v, \tag{3.4}$$

with u and v are the cross-shore and alongshore depth-averaged velocities, c_g is wave group velocity that is obtained from linear wave theory as:

$$c_g = (\frac{1}{2}+\frac{kD}{\sinh 2kD})\frac{\sigma}{k}, \tag{3.5}$$

here, D is water depth, k is wave number. If wave-current interaction is turned off, the last term in the right hand side of Equation (3.3) and Equation (3.4) is not considered.

The propagation speed in θ-space is calculated as:

$$c_\theta = \frac{\sigma}{\sin 2kD}\left(\frac{\partial D}{\partial x}\sin\theta - \frac{\partial D}{\partial y}\cos\theta\right) + \cos\theta\left(\sin\theta\frac{\partial u}{\partial x} - \cos\theta\frac{\partial u}{\partial y}\right) + \sin\theta\left(\sin\theta\frac{\partial v}{\partial x} - \cos\theta\frac{\partial v}{\partial y}\right), \tag{3.6}$$

If wave-current interaction is turned off, the last two terms on the right hand side of Equation (3.6) is not considered.

In case that the wave-current interaction is considered, the wave number k is obtained from the eikonal equations, which can be calculated as:

$$\begin{aligned} &\frac{\partial k_x}{\partial t} + \frac{\partial}{\partial x}(\sigma + k_x u + k_y v) = 0, \\ &\frac{\partial k_y}{\partial t} + \frac{\partial}{\partial y}(\sigma + k_x u + k_y v) = 0, \end{aligned} \tag{3.7}$$

where k_x , k_y are the cross-shore and alongshore component of wave vector respectively, with their relationship to wave number can be expressed as $k = \sqrt{k_x^2 + k_y^2}$. Once the wave number is obtained, the wave frequency σ is then can be obtained from the linear dispersion relation as:

$$\sigma = \sqrt{gk\tanh kD}, \tag{3.8}$$

with g is gravitational acceleration.

In case that the wave-current interaction is not considered, the wave frequency σ is calculated first as σ=$2\pi/T$ and then the wave number is obtained using the linear dispersion relation.

Given the spatial distribution of wave action, and therefore the wave energy distribution, the wave radiation stress can be formulated as:

$$S_{xx} = \int (\frac{c_g}{c}(1+\cos^2\theta) - \frac{1}{2})E_w d\theta$$
$$S_{xy} = S_{yx} = \int \sin\theta\cos\theta(\frac{c_g}{c}E_w)d\theta \tag{3.9}$$
$$S_{yy} = \int (\frac{c_g}{c}(1+\sin^2\theta) - \frac{1}{2})E_w d\theta,$$

where $S_{xx}, S_{xy}, S_{yx}, S_{yy}$ are the components of wave radiation stresses, and $c = \sigma / k$ is the wave phase velocity.

It should be noted that the XBeach model includes a roller energy balance solver, which is turned off in the present study. This is because the roller wave is not taken into account in the present thesis, which is in line with previous modelling studies on self-organization behaviour of rip channels, e.g., Garnier et al. (2008) and Thiébot et al.(2012).

3.3.2 Shallow water equations

The flow is calculated using the depth-averaged nonlinear shallow water equations, which are composed of the water mass conservation and momentum conservation equations:

$$\frac{\partial u}{\partial t} + u\frac{\partial u}{\partial x} + v\frac{\partial u}{\partial y} - \nu_h(\frac{\partial^2 u}{\partial x^2} + \frac{\partial^2 u}{\partial y^2}) + \frac{\tau_x - F_x}{\rho D} + g\frac{\partial \eta}{\partial x} = 0 \tag{3.10}$$

$$\frac{\partial v}{\partial t} + u\frac{\partial v}{\partial x} + v\frac{\partial v}{\partial y} - \nu_h(\frac{\partial^2 v}{\partial x^2} + \frac{\partial^2 v}{\partial y^2}) + \frac{\tau_y - F_y}{\rho D} + g\frac{\partial \eta}{\partial y} = 0 \tag{3.11}$$

$$\frac{\partial \eta}{\partial t} + \frac{\partial Du}{\partial x} + \frac{\partial Dv}{\partial y} = 0, \tag{3.12}$$

in which u and v are the components of depth averaged velocity vector, $\vec{\mathbf{u}}$, in x- and y- direction respectively, ρ is the mass density of water, η is the water surface level, ν_h is the horizontal viscosity coefficient, $\tau_{x,y}$ are components of the bed shear

stress, $F_{x,y}$ are the x- and y-component of wave forcing, which is determined by wave-induced radiation stress tensor and is calculated as:

$$F_x = -(\frac{\partial S_{xx}}{\partial x} + \frac{\partial S_{xy}}{\partial y}), \tag{3.13}$$

$$F_y = -(\frac{\partial S_{xy}}{\partial x} + \frac{\partial S_{yy}}{\partial y}). \tag{3.14}$$

3.3.3 Sediment mass conservation equation

Due to the erosion and deposition of sediment, the seabed level will change temporally. To update seabed level, the sediment mass conservation equation is used:

$$\frac{\partial z_b}{\partial t} + \frac{1}{1-p}(\frac{\partial q_x}{\partial x} + \frac{\partial q_y}{\partial y}) = 0, \tag{3.15}$$

where p is the sediment porosity and is set to be 0.4 throughout this thesis, q_x and q_y are sediment transport flux $\overrightarrow{q_s}$ in x- and y- directions, z_b is the seabed level.

3.4 Formulas for variables in the governing equations

3.4.1 Wave breaking and energy dissipation

The wave energy dissipation can be caused due to the wave breaking and bed friction. However, considering the wave energy dissipation due to bed friction is small compared to that caused by wave breaking, only the wave energy dissipation due to the wave breaking will be taken into account in this thesis. To calculate the wave energy dissipation that caused by wave breaking in each directional bin, the total wave energy dissipation $\overline{D_w}$ is firstly needed to be determined, which is then distributed proportionally over the wave directions as:

$$D_w = \frac{E_w}{\overline{E_w}} \overline{D_w}, \tag{3.16}$$

where $\overline{E_w}$ is the total wave energy.

Table 3.1 Different formulas of wave energy dissipation due to wave breaking

Break	Wave type	Origin	Formula expression [a]
break=1	instationary	Roelvink (1993)	$\overline{D_w} = 2\frac{\alpha_w}{T} Q_b \overline{E_w}$ with $Q_b = 1 - \exp\left(-\left(\frac{H_{rms}}{H_{\max}}\right)^n\right)$ $H_{rms} = \sqrt{\frac{8\overline{E_w}}{\rho g}}$ $H_{\max} = \frac{\gamma_1 \tanh kD}{k}$
break=2	stationary	Baldock et al.(1998)	$\overline{D_w} = \frac{\alpha_w}{4T} Q_b \rho g (H_b^2 + H_{rms}^2)$ With $Q_b = \exp\left[-\left(\frac{H_b^2}{H_{rms}^2}\right)\right]$ $H_b = \frac{0.88}{k}\tanh\left[\frac{\gamma_1 kD}{0.88}\right]$
break=3	instationary	Variant of Roelvink (1993)	$\overline{D_w} = 2\frac{\alpha_w}{T} Q_b \overline{E_w} \frac{H_{rms}}{D}$ Q_b is calculated same as break=1
break=4	instationary	Roelvink and Daly (unpublished)	$\overline{D_w} = 2\frac{\alpha_w}{T} Q_b \overline{E_w}$ Q_b is calculated same as break=1, But $Q_b = 1, if\ H_{rms} > \gamma_1 D$ $Q_b = 0, if\ H_{rms} < \gamma_2 D$
break=5	stationary	Thornton and Guza (1983)	$\overline{D_w} = \frac{3\rho g \sigma B^3}{32\sqrt{\pi}} \frac{H_{rms}^{\ 5}}{\gamma_b^{\ 2} D^3} (1 - \frac{1}{(1+(H_{rms}/\gamma_b D)^2)^{2.5}})$

[a] $\alpha_w = O(1)$, T is wave period, Q_b is fraction of breaking waves, H_{rms} is root-mean-square wave height, γ_1 is break index (0.55 in this thesis), γ_2 is a free parameter, B is the breaking related coefficient (here, $B = 1.0$), γ_b is the breaker index (default $\gamma_b = 0.42$ (Thornton and Guza, 1983)).

There are a number of different formulas for calculation of total wave energy dissipation due to wave breaking in XBeach model, such as formula that proposed by Baldock et al.(1998), Roelvink (1993) and its variants. Besides these formula, we have added a new wave energy dissipation formula here, which is proposed by Thornton and Guza (1983), i.e., break=5. The detailed information about the five different wave energy dissipation formulas in the modified XBeach model are listed in Table 3.1.

3.4.2 Undertow

The undertow in XBeach model is calculated as:

$$u_s = -\frac{\overline{E_w}\cos\theta}{\rho D c}, \qquad v_s = -\frac{\overline{E_w}\sin\theta}{\rho D c}, \tag{3.17}$$

with u_s and v_s represents the component of undertow in x- and y- direction respectively.

3.4.3 Wave skewness and asymmetry

The amplitude of flow velocity related to wave skewness and asymmetry V_m is calculated as:

$$V_w = \gamma_{ua} u_{rms}(S_k - A_s), \tag{3.18}$$

where γ_{ua} is a calibration factor, u_{rms} is root-mean-square wave orbital velocity amplitude at the seabed:

$$u_{rms} = \frac{\pi H_{rms}}{T \sinh(kD)}. \tag{3.19}$$

S_k and A_s represents the wave skewness and asymmetry respectively, which is calculated as:

$$\begin{aligned} S_k &= \frac{0.79}{1+\exp\frac{-0.61-\log U_r}{-0.35}} \cos(-\frac{\pi}{2}+\frac{\pi}{2}\tanh(0.64/U_r^{0.60})), \\ A_s &= \frac{0.79}{1+\exp\frac{-0.61-\log U_r}{-0.35}} \sin(-\frac{\pi}{2}+\frac{\pi}{2}\tanh(0.64/U_r^{0.60})). \end{aligned} \tag{3.20}$$

Here, U_r is Ursell number and is defined as $U_r = H_{rms} L_w^2 / D^3$. The Ursell number is the parameter that used to indicate the nonlinearity of waves.

Once V_w is determined, it will be decomposed into alongshore and cross-shore component as:

$$\begin{aligned} u_a &= V_w \cos\theta, \\ v_a &= V_w \sin\theta. \end{aligned} \tag{3.21}$$

3.4.4 Bed shear stress

The bed shear stress in the momentum conservation equation is calculated using the formulation proposed by Feddersen et al. (2000):

$$\begin{aligned} \tau_{\mathbf{x}} &= c_f \rho u^E \sqrt{(1.16 u_{rms})^2 + (u^E)^2}, \\ \tau_{\mathbf{y}} &= c_f \rho v^E \sqrt{(1.16 u_{rms})^2 + (v^E)^2}, \end{aligned} \tag{3.22}$$

with c_f represents the friction coefficient (here, $c_f = 0.01$, i.e., without considering the effects of sediment size), u^E and v^E is cross-shore and longshore component of Eulerian velocity, which is calculated as:

$$\begin{aligned} u^E &= u + u_s, \\ v^E &= v + v_s. \end{aligned} \tag{3.23}$$

In the case that the undertow vanishes, the strength of Eulerian current velocity will be equal to the strength of depth averaged velocity that calculated from Equation (3.10) and Equation(3.11). In this situation, the bed shear stress can be calculated using depth averaged velocity instead as:

$$\begin{aligned} \tau_{\mathbf{x}} &= c_f \rho u \sqrt{(1.16u_{rms})^2 + u^2}, \\ \tau_{\mathbf{y}} &= c_f \rho v \sqrt{(1.16u_{rms})^2 + v^2}. \end{aligned} \tag{3.24}$$

3.4.5 Sediment transport flux

The sediment transport flux $\overrightarrow{q_s}$ in Equation (3.15) is calculated using the formula of Soulsby (1997), which is because it is also widely used in the previous studies on self-organization behaviours of rip channels (Garnier et al., 2008; Garnier et al., 2010b). This formula is written as:

$$\overrightarrow{q_s} = \alpha(\overrightarrow{V} - \gamma u_{rms} \nabla z_b), \tag{3.25}$$

where $\overrightarrow{V}$ is the current velocity that takes both the undertow and the velocity caused by wave nonlinearity into account; γ is the bed slope coefficient, the value of which is $O(1)$; α is depth-integrated volumetric sediment concentration given by Soulsby (1997):

$$\begin{aligned} &if \left(\left(u^E\right)^2 + \left(v^E\right)^2 + \frac{0.018}{c_D} u_{rms}^2 \right)^{1/2} > u_{cr} \\ &\qquad \alpha = A_s \left[\left(\left(u^E\right)^2 + \left(v^E\right)^2 + \frac{0.018}{c_D} u_{rms}^2 \right)^{1/2} - u_{cr} \right]^{2.4} \\ &otherwise, \\ &\qquad \alpha = 0 \end{aligned} \tag{3.26}$$

in which c_D is the drag coefficient calculated as $c_D = (0.40/(\ln(D/z_r) - 1))^2$ with z_r is the roughness length (default value: $z_r = 0.006m$); $A_s = A_{sb} + A_{ss}$ with A_{sb} and A_{ss} are the coefficients for the bedload and suspended load transport:

$$A_{sb} = \frac{0.005D(d_g/D)^{1.2}}{[(s-1)gd_g]^{1.2}},$$
$$A_{ss} = \frac{0.012d_g D_*^{-0.6}}{[(s-1)gd_g]^{1.2}}, \tag{3.27}$$

in which s is the relative density of sediment (here, s =2.65), d_g is the grain size. D_* is the dimensionless grain size:

$$D_* = \left(\frac{g(s-1)}{k_b^2}\right)^{1/3} d_g, \tag{3.28}$$

and k_b is the kinematic viscosity of water (default value: $k_b = 1.3\times10^{-6} m^2 s^{-2}$).

The parameter u_{cr} in Equation (3.26) is the threshold current velocity of motion, which is dependent on the water depth and grain size:

$$u_{cr} = 0.19\left(d_g\right)^{0.1} \log_{10}\left(\frac{4D}{d_g}\right) \; for \; 0.1 \le d_g \le 0.5mm,$$
$$u_{cr} = 8.5\left(d_g\right)^{0.6} \log_{10}\left(\frac{4D}{d_g}\right) \; for \; 0.5 \le d_g \le 2mm. \tag{3.29}$$

To be much clearer, the expression of Equation (3.25) is expanded here, which is written as:

$$q_x = \alpha u + \alpha u_s + \alpha u_a - \gamma u_{rms}\frac{\partial h}{\partial x} - \gamma u_{rms}\frac{\partial z_0}{\partial x}, \tag{3.30}$$

$$q_y = \alpha v + \alpha v_s + \alpha v_a - \gamma u_{rms}\frac{\partial h}{\partial y} - \gamma u_{rms}\frac{\partial z_0}{\partial y}, \tag{3.31}$$

where z_0 is the initial alongshore uniform bathymetry, i.e., basic state; h is the bed level deviation from the initial alongshore uniform bathymetry.

3.4.6 Including/excluding the three dimensional cross-shore process

In XBeach model, three dimensional structures of current are parameterized by characterizing its cross-shore vertical structure using the offshore-oriented undertow and onshore-oriented current deduced by wave skewness and asymmetry (In more general, these two terms are also named as wave nonlinearity). The undertow is inserted into the calculation of bed shear stress (see Equation(3.22)) and sediment transports flux (see Equation(3.26), Equation (3.30) and Equation (3.31)), while the onshore currents caused by wave nonlinearity is inserted in Equation(3.30) and Equation (3.31).

In the present thesis, the vertical current structure (undertow and onshore currents caused by wave nonlinearity) is disconnected to the modelling framework and therefore their effects on the hydrodynamic and morphodynamic processes are excluded. This is because our interests are to study the formation and evolution of rip channels emerged from the self-organization behaviour rather than the cross-shore migration of bars, under which the sediment transport driven by the alongshore current and rip currents is typically much larger than the sediment transport driven by undertow and wave-nonlinearity.

In the case that the cross-shore vertical current structure is excluded, we assume that the onshore transport by wave nonlinearity induced current and undertow is in balance with the gravitational downslope transport. Therefore, the second, third and last term on the right hand side of Equation (3.30) and Equation (3.31) are vanished, which make the sediment transport formula simplified as:

$$q_x = \alpha u - \gamma u_{rms} \frac{\partial h}{\partial x}, \tag{3.32}$$

$$q_y = \alpha v - \gamma u_{rms} \frac{\partial h}{\partial y}. \tag{3.33}$$

In this condition, the initial bathymetry that is alongshore uniform would be supposed to be an equilibrium profile. This assumption has been commonly adopted in all the modelling studies on the self-organization behaviour of rip channels

(Castelle and Ruessink, 2011; Damgaard et al., 2002; Garnier et al., 2006; Garnier et al., 2010a; Thiébot et al., 2012). In order to keep in coherent within the modelling framework, the cross-shore vertical effects are exclude from the bed shear stresses as well, when the cross-shore sediment transport due to undertow and waves nonlinearity are excluded. Therefore, in such situation, the bed shear stress is then governed by Equation(3.24). Similar operation is implemented in Equation(3.26), where the Eulerian velocity is replaced by depth averaged current velocity obtained from the momentum conservation equation.

3.5 Grid setup and boundary conditions

3.5.1 Grid setup

The modelling domain is rectilinear, with its x- axis is approximately perpendicular toward the coast and its y- axis is orthogonal to the x- axis and thus the y- direction is nearly alongshore parallel. The cross-shore length of modelling domain is defined as L_x , and the alongshore length of modelling domain is defined as L_y . The modelling domain is discretized into n_x grids in x- direction and n_y grids in y- direction, with their grid size defined as Δx and Δy, respectively. The XBeach model employs a staggered grid (see Figure 3.2), in which the variables used in XBeach model can be specified either in the cell centre or at the cell interfaces. More specifically, the scalar quantities like bed levels, wave energy balance, water surface levels, water depths and sediment concentrations are set in cell centres, and vector quantities like radiation stress gradients, current velocities and sediment transports are defined at the cell interfaces. The points on the cell interfaces can be divided into u- and v- points.

Current velocities at u- and v- points are denoted as uu and vv respectively, which are updated by the shallow water equation directly. But, the current velocities at the cell centres are interpolated from the four surrounding grid points on u- and v- grid and are for output purpose only. Similarly, the u- velocity on v- grid (v- velocity on

u- grid), denoted as uv (vu), is obtained by interpolation from the four surrounding points on v- grid (u- grid).

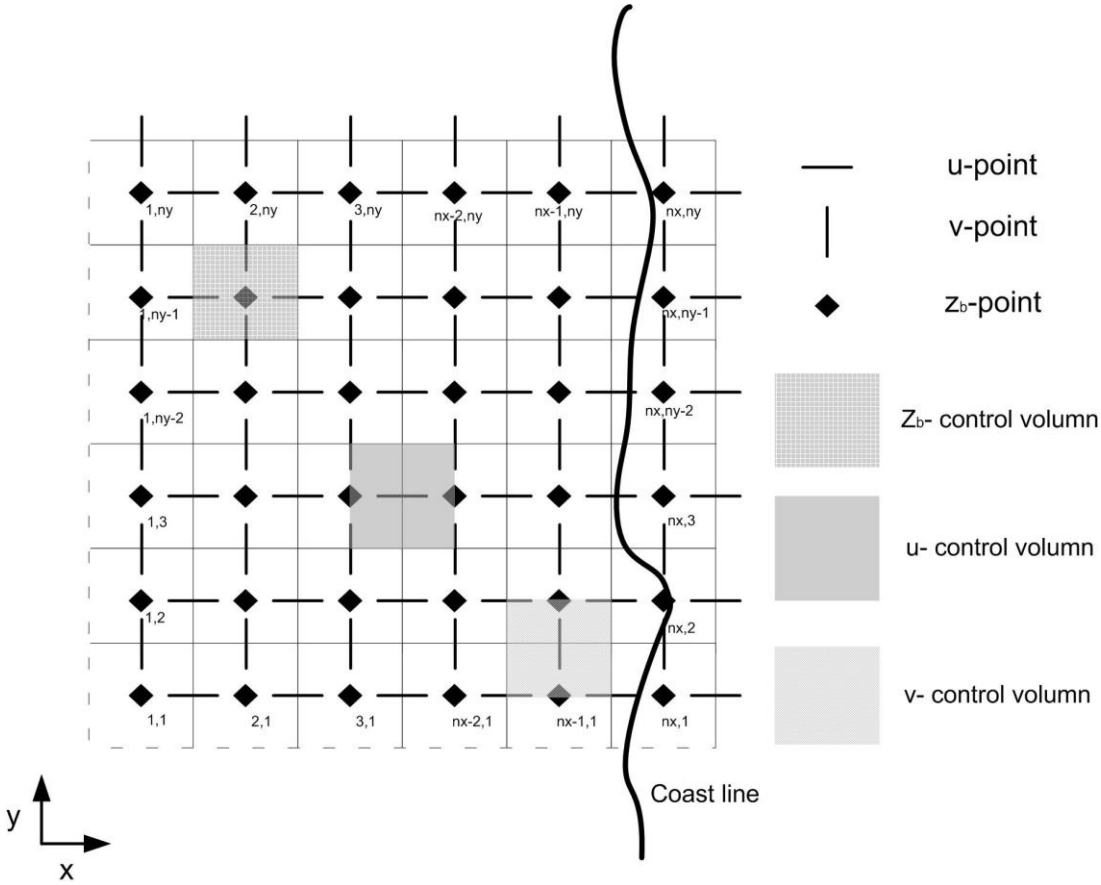

Figure 3.2 Staggered grid in XBeach

3.5.2 Boundary conditions

Offshore boundary conditions

The XBeach model is driven by the waves imposed on the offshore boundary. In XBeach, a number of different wave boundary include that for both of stationary and instationary (including infragravity motions) wave conditions are optional. However, in the present thesis, only stationary waves will be taken into account. This is because the primary objective of this study is to investigate the self-organization behaviour of rip channels, for which the morphodynamics in the surf zone are

concentrated. In the surf zone, the impacts of infragravity waves are supposed to be small. Furthermore, previous modelling studies also show that the infragravity waves have neglectable effects on the morphodynamic evolution of rip channels (de Schipper et al., 2014; Reniers et al., 2004). Another advantage of considering stationary waves is the reduction of the computation time, as the solver for the stationary waves utilizes a forward marching technique, where the equations are solved row by row.

In the case of using stationary waves, the main parameters need to be specified at the offshore boundary include wave height, wave period and wave direction. The specified waves will then propagate into the modelling domain and generate currents. The waves and currents in the domain may then need to pass through the offshore boundary to the deep sea with minimal reflection. To do so, a weakly reflective-type boundary is activated and applied to the variables of uu, vv and η, following the work by Dongeren and Svendsen (1997). More detailed information can be found in the manual of XBeach model (Roelvink et al., 2010).

Lateral boundary conditions

The lateral boundary conditions in the original XBeach are Neumann conditions. In the present study, the periodic boundary conditions are also implemented, as here we are interested in the rip channel systems that are alongshore rhythmic. The lateral boundary condition has been applied on the variables include wave height H_{rms}, wave number k, wave frequency σ, water surface level η, seabed level z_b, depth averaged current velocities uu and vv.

If the Neumann boundary conditions are specified, then the gradient in variables mentioned above on the lateral boundaries is assumed be zero. For instance, the current velocity at the lateral boundaries under Neumann boundary conditions can be written as:

$$\begin{aligned} &uu(1:nx,1) = uu(1:nx,2), \\ &uu(1:nx,ny) = uu(1:nx,ny\text{-}1), \\ &vv(1:nx,1) = vv(1:nx,2), \\ &vv(1:nx,ny) = vv(1:nx,ny\text{-}1). \end{aligned} \tag{3.34}$$

If the periodic boundary conditions are specified, then the value and first y- derivative in variables mentioned above on the left and right lateral boundary are assumed be the equal. For instance, the current velocity at the lateral boundaries under periodic boundary conditions can be written as:

$$\begin{aligned} &uu(1:nx,1) = uu(1:nx,ny-1), \\ &uu(1:nx,ny) = uu(1:nx,2), \\ &vv(1:nx,1) = vv(1:nx,ny-1), \\ &vv(1:nx,ny) = vv(1:nx,2). \end{aligned} \tag{3.35}$$

Shore boundary conditions

At the shore boundary, we impose non-flux conditions, which mean that no current and sediment transport can pass through the shore boundary. The purpose of using this type of boundary conditions is to avoid the complications of swash zone dynamics, which are expected to have negligible effects on the dynamics of rip channel system. The non-flux shore boundary conditions are only applied on the variables of uu, vv and q_x, which are written as:

$$\begin{aligned} &uu(nx,1:ny) = 0, \\ &vv(nx,1:ny) = \frac{1}{3} vv(nx-1,1:ny), \\ &q_x(nx,1:ny) = 0. \end{aligned} \tag{3.36}$$

Chapter 4

Emergence and dynamics of rip channels on a barred beach: modified XBeach validation

4.1 Introduction

In this chapter, the capability of modified XBeach model on studying the self-organization behaviour of rip channels is tested by investigating the emergence and dynamics of rip channels on a barred beach. The cross-shore profile of this barred beach is same as the single barred beach presented in Yu and Slinn (2003). In fact, selecting this bathymetry is because the same bathymetry profile has been used in previous studies of both linear stability analysis (Calvete et al., 2005) and nonlinear stability analysis (Garnier et al., 2008), which then can provide as an useful tool for validating the prediction from the modified XBeach model.

The main specific goals in this chapter including:

- to investigate whether the modified XBeach model can generate the rip channels from the interaction of topography, waves and currents,
- to test whether the modified XBeach model can produce the typical morphodynamic behaviour of rip channels, such as the merging and splitting of sandbars,
- to investigate whether the properties and dynamics of rip channels predicted by the modified XBeach model are in consistent with previous studies.

This chapter is organized as follow: in Section 4.2, the set-up of the numerical simulations is illustrated. In Section 4.3 the definitions of response indicators that used to describe the geometrical and dynamical properties of rip channels are given. In Section 4.4 the main results of numerical simulations are presented. Section 4.5

gives a discussion on the modelling results. The summary of this chapter is drawn in the final section.

4.2 Setup of numerical simulations

Initial topography

The initial topography used in the simulations is composed of an alongshore uniform barred beach profile and a random perturbation. The cross-shore profile of alongshore uniform barred beach is taken from the study of Yu and Slinn (2003), which is based on the observed bar system at Duck, North Carolina. This barred beach profile can be formulated as:

$$z_0 = \underbrace{-a_0 - a_1(1-\frac{\beta_2}{\beta_1})\tanh\left(\frac{\beta_1 x'}{a_1}\right) - \beta_2 x'}_{planar\ slope} + \underbrace{a_2 \exp\left[-5\left(\frac{x'-x_c}{x_c}\right)^2\right]}_{bar}, \tag{4.1}$$

where x' is the cross-shore coordinate. From Equation(4.1), we can see that the initial cross-shore profile of alongshore uniform barred beach consists of a planar slope and a sandbar. The parameters that related to the planar slope include: $a_0 = 0.25m$ and $a_1 = 2.97m$ that represents the approximate depth of water near swash/surf zone boundary respectively, β_1=0.075 and β_2=0.0064 are the slope of shoreline and offshore. The parameters that determine the shape of sandbar are $a_2 = 1.5m$ as the bar amplitude and $x_c = 80m$ gives the location of bar crest. Figure 4.1 gives a three dimensional view of the initial bathymetry of barred beach, which extend offshore to location with water depth is approximate 4.5 m. However, it should be noted that the direction of x- axis has been inversed with respective to that used in Equation(4.1). In detail, the coordinate of x- axis is positive seaward in

Equation(4.1), while it is positive landward in Figure 4.1, which is in consistent with the coordinates used in XBeach model. The random perturbation that imposed on the alongshore uniform beach has a magnitude of $3\,cm$.

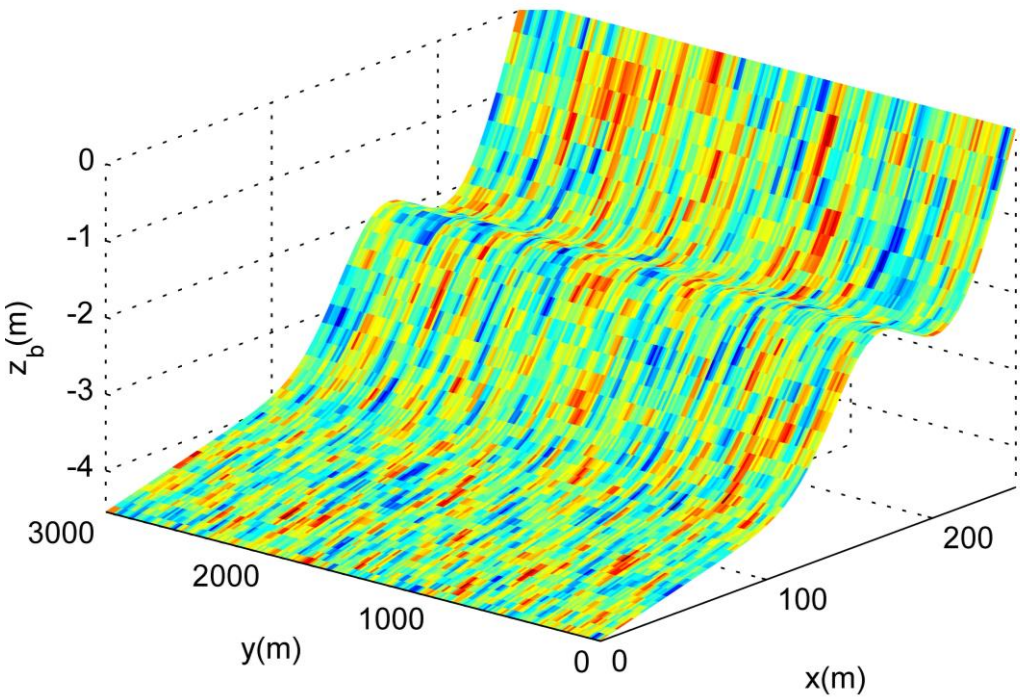

Figure 4.1 Three-dimensional view of the initial bathymetry, with the color represents the perturbations.

Computational domain and parameters set-up

The computational domain has an extension $L_x = 250\,m$ in the cross-shore direction, and $L_y = 3000\,m$ in alongshore direction. The grid spacing is $(\Delta x, \Delta y) = (5, 15)\,m$. At the seaward boundary, the stationary waves are imposed. The formulation of Baldock et al.(1998) is used to calculate the wave energy dissipation due to break. For all variables their default values in XBeach model are used, except that for bed slope coefficient γ. Here, the value of γ is chosen to be equal to 5 (in default γ=1.6), which is in consistent with the previous numerical studies by Garnier et al.(2008). In

fact, large uncertainty exist on determine the value of γ. The reasons for chosen of γ=5 here is two folder. First, we want to reach the saturation state of rip channels, which needs the down slope transport of sediment being adequate to damp the transport due to convection. Secondly, the use of same bed slope coefficient also makes a more convenient comparison between our results and the previous results by Garnier and his co-workers (Garnier et al., 2008), who used the same bathymetry as the one used here. In the lateral boundaries, the periodic boundary conditions are used.

Table 4.1 Input parameters for all eight simulations

Case No	H^0_{rms} (m)	θ^0 (deg)	T (s)	Simulation timelength (day)	d_g (mm)
C1	0.8	0	9	100	0.25
C2	1	0	9	100	0.25
C3	1.2	0	9	100	0.25
C4	1	2	9	300	0.25
C5	1	4	9	300	0.25
C6	1	6	9	300	0.25
C7	1	8	9	300	0.25
C8	1	10	9	300	0.25

We have run simulations using both normal and oblique incident waves, with totally eight different offshore wave conditions are specified. The input parameters including that of wave conditions, sediment size and simulations length are shown in Table 4.1. Specifically, we have varied the wave angle at the offshore boundary from

shore normal to 10° with a 2° step size (i.e., $\theta^0 = 0^\circ, 2^\circ, 4^\circ, 6^\circ, 8^\circ, 10^\circ.$) for incident wave height $H^0_{rms} = 1.0\,m$ and incident wave height from 0.8 to 1.2 m with a 0.2 m step size (i.e., $H^0_{rms} = 0.8\,m, 1.0\,m, 1.2\,m$) for normal waves $\theta^0 = 0^\circ$. The incident wave period has been kept equal to 9 s and the sediment size is kept equal to 0.25 mm. The simulation time length is 100 days for simulations using normal waves and 300 days for simulations using oblique waves. The default simulations under normal and oblique waves are case C2 and C5 respectively.

4.3 Rip channel response indicators

To describe the formation and evolution of rip channels, a number of rip channel response indicators, representing the geometrical and dynamical characteristics of rip channels, are used in the present study. The indicators representing rip channel geometrical properties include predominant spacing λ_m , rip channel three-dimensionality $\|h\|$ and rip channel amplitude A_m, while indicators that related to dynamical characteristics of rip channels include growth rate Ω, migration speed c_m, response time t_r and saturation time t_s.

Geometrical characteristics indicators

The predominant wavelength of rip channels λ_m is calculated using the Fourier analysis. Here, Fourier transform is applied on the bed level perturbation signal at the alongshore section of $x = 190\,m$:

$$F_z(k_l) = \sum_{j=1}^{ny} h(190, y_j) \exp\left(-i \frac{2\pi}{ny} (j-1)(l-1) \right), \tag{4.2}$$

where $F_z(k_l)$ is the Fourier coefficient for the wavenumber (also named as mode) of the perturbation signal k_l . Here, k_l is defined as:

$$k_l = \frac{2\pi(l-1)}{L_y}, \quad l = 1:ny. \tag{4.3}$$

The modulus of the Fourier coefficients $F_z(k_l)$ is denoted as $|F_z(k_l)|$. The distribution of the significance of $|F_z(k_l)|$ gives the information on the relative intensities of signal on different modes k_l. The dominant mode, denoted as k_m, is the mode that has the maximum modulus of the Fourier coefficients. The predominant wavelength of rip channels λ_m is the wavelength that corresponds to the dominant mode k_m, which is calculated as:

$$\lambda_m = \frac{2\pi}{k_m}. \tag{4.4}$$

The rip channel three-dimensionality $\|h\|$ is calculated using the method of "global analysis" (Garnier et al., 2006; Garnier et al., 2010a), which takes the variables over the whole modelling domain into account:

$$\|\mathrm{h}\| = \left(\frac{1}{\mathrm{L_x} L_y} \int_0^{L_x} \int_0^{L_y} h(x,y,t)^2 \, dxdy \right)^{1/2}. \tag{4.5}$$

The rip channel amplitude A_m is defined as half of the height different between the maximum ($h_{\max}$) and minimum ($h_{\min}$) value of h throughout the modelling domain:

$$A_m = \frac{1}{2}(h_{\max} - h_{\min}). \tag{4.6}$$

Dynamical characteristics indicators

The growth rate Ω is deduced from the evolution curve of $\|h\|$:

$$\Omega(t) = \frac{1}{2\|h\|^2} \frac{d\|h\|^2}{dt}, \tag{4.7}$$

Response time t_r and saturation time t_s can be obtained from the evolution curve of growth rate Ω. Specifically, the response time t_r is defined as the moment that the growth rate reaches its peak after which the growth rate starts to decrease. The saturation time t_s is defined as the time that the growth rate first decreased to $\Omega < 0.01\,d^{-1}$ after the response time.

The migration speed c_m is defined as the distance that rip channels move alongshore in a day. This speed can be calculated by the temporal track of specified rip channel trough or crest.

4.4 Modeling results

In this section, results of the two default simulations, i.e., case C2 and C5, are firstly described. Then, the modelling results presented here are compared with the predictions using MORFO55 by Garnier and his co-authors (2008) and the previous field observations.

4.4.1 Emergence and dynamics of rip channels under normal waves

Hydrodynamic and morphological characteristics

The snapshot of bed morphology over the full modelling domain on day 21.3 for the reference simulation with normal-incident wave is shown in Figure 4.2a, from which we can see that sixteen well-developed rip channels spread quasi-periodically in the alongshore direction, with a mean wavelength $\lambda_{mean} \approx 190m$. The rip channels are composed of deep troughs and shallow shoals, with the axis of shoals (the direction pointed from the shoreward head of bars to the seaward head of bars) are nearly perpendicular to the shoreline. The alongshore bed profile at $x = 190\,m$ on day 0 and day 21.3 are given in Figure 4.2b, from which we can see that the depth at the troughs increase while the depth at shoals decrease comparing to the initial depth.

Moreover, the widths of troughs are relatively shorter comparing to the widths of shoals. Applying the Fourier transform on the alongshore bed profile $z_b(190, y, 21.3)$, we can obtain the predominant wavelength of rip channels at day 21.3 for this simulation is $\lambda_m = 158\,m$ (Figure 4.2c). It should be noted that the same predominant wavelength can be obtained if another alongshore bed profile is used. In addition, we can find that the predominant wavelength may not strictly same to the mean wavelength that derived by counting the number of rip channels in the modelling domain.

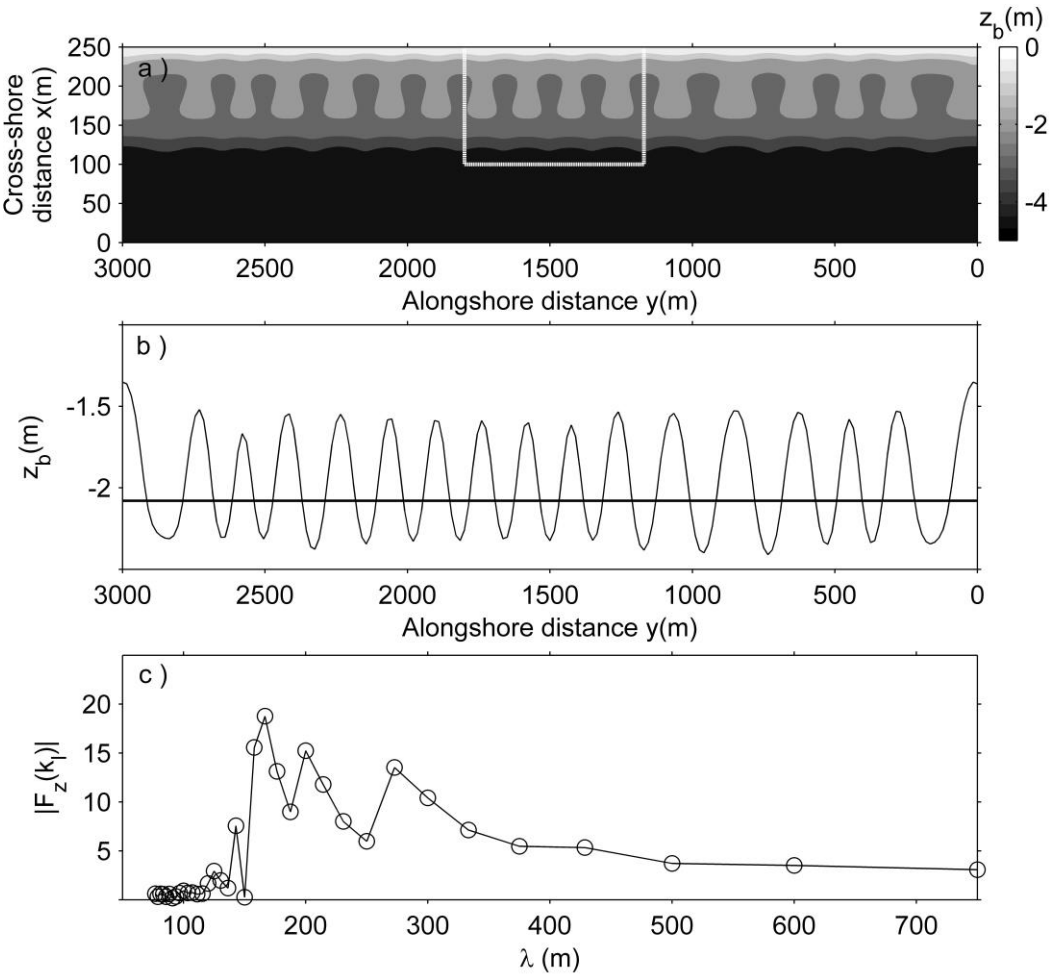

Figure 4.2 (a) Snapshot of rip channel morphology after 21.3 days of simulation for $H^0_{rms} = 1.0\,m,\ \theta^0 = 0^\circ$. (b) The alongshore bed profile at $x = 190\,m$ for day 0 (thick line) and day 21.3 (thin line). (c) The spectrum of $|F_z(k_l)|$ for $z_b(190, y, 21.3)$.

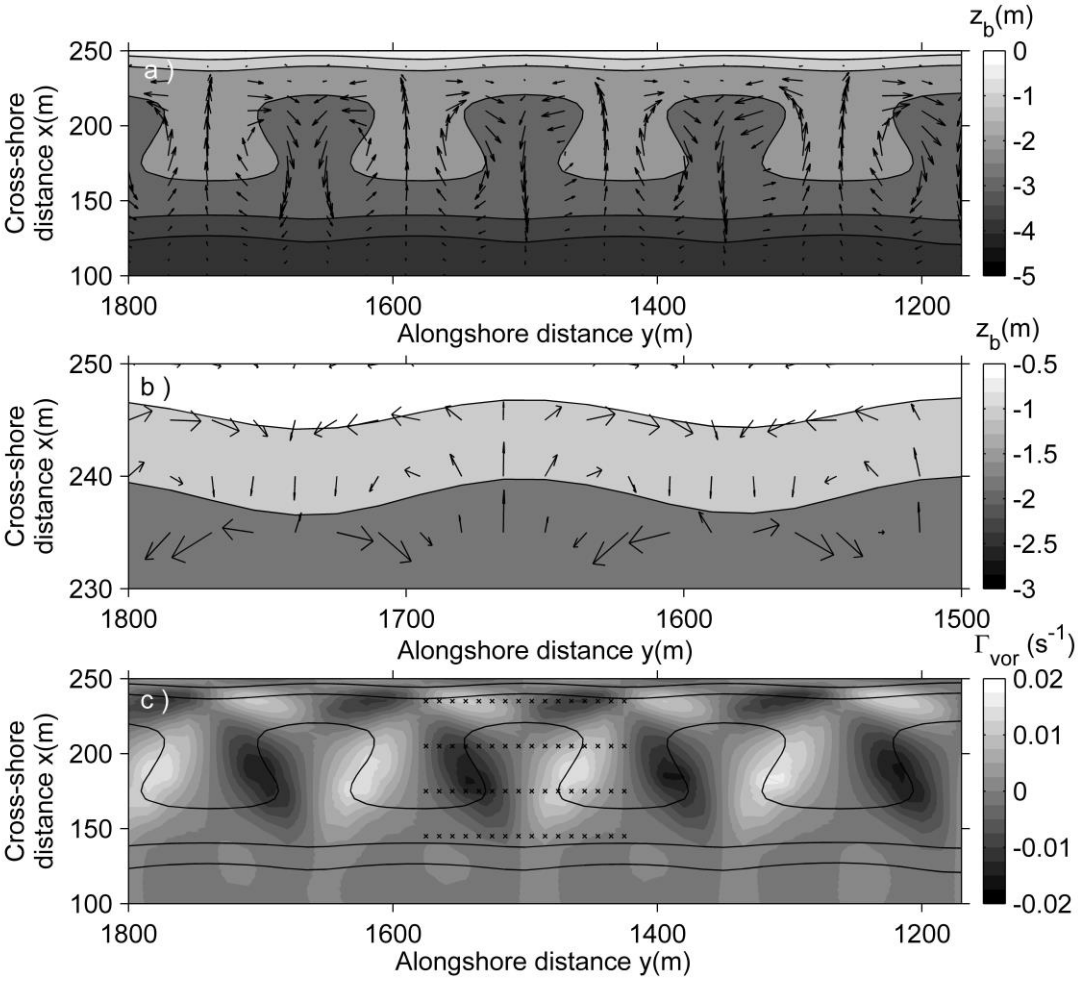

Figure 4.3 The seabed with superimposed currents at day 21.3 for $H_{rms}^{0} = 1.0\,m$, $\theta^{0} = 0^{\circ}$ in the area between (a) 100 m<x<250 m and 1170 m<y<1800 m and (b) 230 m<x<250 m and 1500 m<y<1800 m. (c) The vorticity corresponding to (a).

Figure 4.3a shows the bathymetry in the area of $100\,m < x < 250\,m$ and $1170\,m < y < 1800\,m$ together with the corresponding current circulation. Clearly, the classic rip current circulations with onshore flow over the shoals and strong offshore current at the troughs are apparent in the area of $x < 220\,m$ approximately. These circulations are named as main circulation, which is termed relatively to the secondary circulation exists close to the shoreline as the strength of secondary circulation is weak comparing to the main circulation. Figure 4.3b gives a clearer close up view of the secondary circulation that presented in Figure 4.3a. From this

figure, we can find that the rotation direction of secondary circulation is counter to the rotation direction of the main circulation, with the onshore current presented in the trough and offshore current over the shoals. The characteristics of rip current circulation can be analysed in more detail by examining the vorticity, defined as $\Gamma_{vor} = \partial v / \partial x - \partial u / \partial y$. Figure 4.3c shows the resulting vorticity pattern for the current circulation field that presented in Figure 4.3a. From this figure, we can clearly see that the exact pattern is four-quadrant circulation, i.e., four circulation cells cover the single rip channel, which is in line with the laboratory observations over a rip channelled beach (Haller et al., 2002; Kennedy and Thomas, 2004). The pair of circulation cells near the shoreline is relative small in space comparing to the pair of circulation cells seaward. The interface of the two circulation cells in each pair is near the center of trough where the absolute cross-shore current velocity is nearly its max. The maximum absolute vorticity occur near the center of each circulation cell.

The main reason for the circulation pattern observed here is actually the breaking of waves. When propagating to the shoreline and arriving at the sandbar (near $x = 170\,m$), a large amount of wave energy will dissipate due to the wave breaking. Comparing to the trough area, more wave energy dissipate over the shoal (Figure 4.4b). Therefore, the wave height over the shoal decreases faster than that at the trough, making the wave height is larger in the trough than over the shoal (Figure 4.4a). The higher waves penetrate the trough will final break near the shoreline, as can be seen from Figure 4.4b that more wave energy dissipation occur in the trough than over the bar for area within about $x > 220\,m$. In fact, the higher wave energy dissipation can cause an onshore current. The higher wave energy dissipation over the shoal near $x = 170\,m$ thus can generate onshore current over the shoal, which then flow back seaward through the trough, both of which form the main current circulation. Near the shoreline, the higher wave energy dissipation at the trough can thus generate an onshore current over the trough and cause the counter rotating secondary circulations.

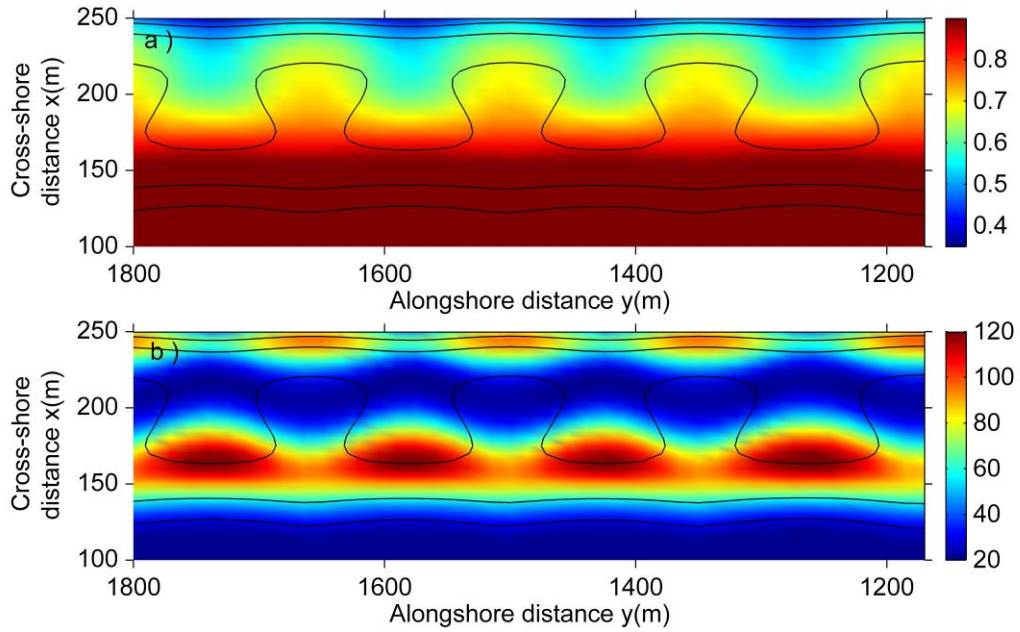

Figure 4.4 (a) Root mean square wave height and (b) wave energy dissipation over the domain 100 m<x<250 m and 1170 m<y<1800 m for $H_{rms}^{0} = 1.0\,m,\ \theta^{0} = 0^{\circ}$ at day 21.3. The unit of colorbar is meter in (a) and W/m^2 in (b).

For rip current circulation, an important issue is how the material such as sediment is transported within the surf zone of rip-channelled beach. To understand this issue, the Lagrangian behaviour of rip current circulations is investigated here by tracking the paths of artificial Lagrangian drifters in the hydrodynamic experiment. This hydrodynamic experiment is designed as follow: 64 artificial drifters are set in the domain of $140\,m \le x \le 230\,m$ and $1425\,m \le y \le 1575\,m$ with the interval length are $10\,m$ alongshore and $30\,m$ across shore (as shown in Figure 4.3c, i.e., the crosses). The bathymetry of default simulation under normal waves (case C2) at day 21.3 is frozen, which is used as the bathymetry for the hydrodynamic experiment. Then the same wave conditions as used in case C2 are imposed at the sea boundary, i.e., $H_{\mathrm{rms}}^{0} = 1\,m, \theta^{0} = 0^{\circ}$. The drifters are released after 15 minutes at which the current field is stable already. The paths of drifters are recorded for 12 hours. From this hydrodynamic experiment, we find that the three different types of rip current circulations distinguished from the field observations are all existed in the present

hydrodynamics experiment: 1) rip circulation, in which the drifter rotate around the center of circulation (Figure 4.5a); 2) sinuous alongshore current, in which the drifter moves up the beach over the shoal and roams down the beach across the trough in the cross-shore direction together with a movement alongshore (Figure 4.5c); 3) meandering current, in which the drifter roams up and down of the beach, with either staying in a particular rip cell or moving to the adjacent rip cell (Figure 4.5b). In fact, the meandering current is essentially a combination of rip current and sinuous alongshore current.

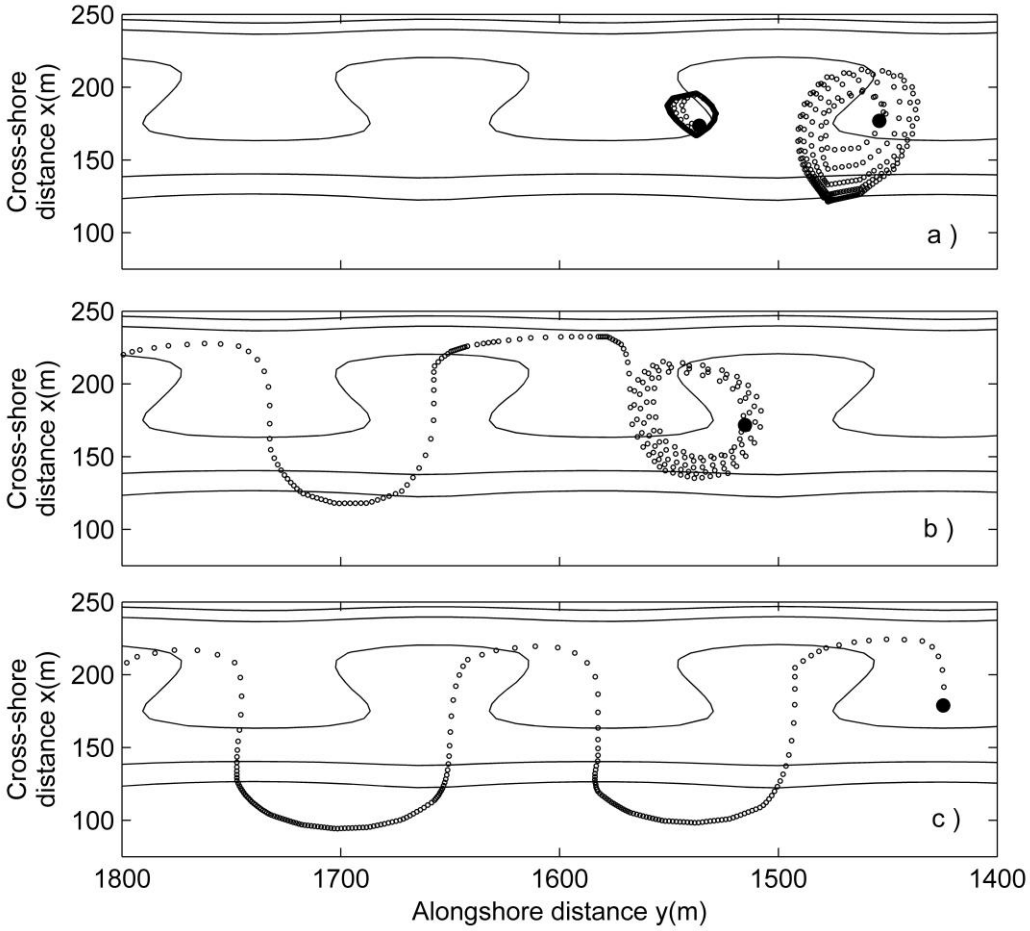

Figure 4.5 Representative paths of three different rip current circulations for $H_{rms}^{0} = 1.0\,m,\ \theta^{0} = 0^{\circ}$: (a) rip current, (b) meandering current, (c) sinuous alongshore current. The large filled dots indicate the origins of the drifters.

Figure 4.6a shows that most of the drifter paths fall into the rip current type (denoted as R-type), followed by the sinuous alongshore current type (denoted as S-type) and then the meandering type (denoted as M-type). On spatially, the R-type drifters mainly exist in the area corresponds to the Eulerian circulation cell (see Figure 4.3c), while the S-type drifters roughly exist in the area between the different Eulerian circulation cells where the absolute vorticity is small. The M-type drifters are generally located in between. This distribution pattern of different drifters can be seen in Figure 4.6b.

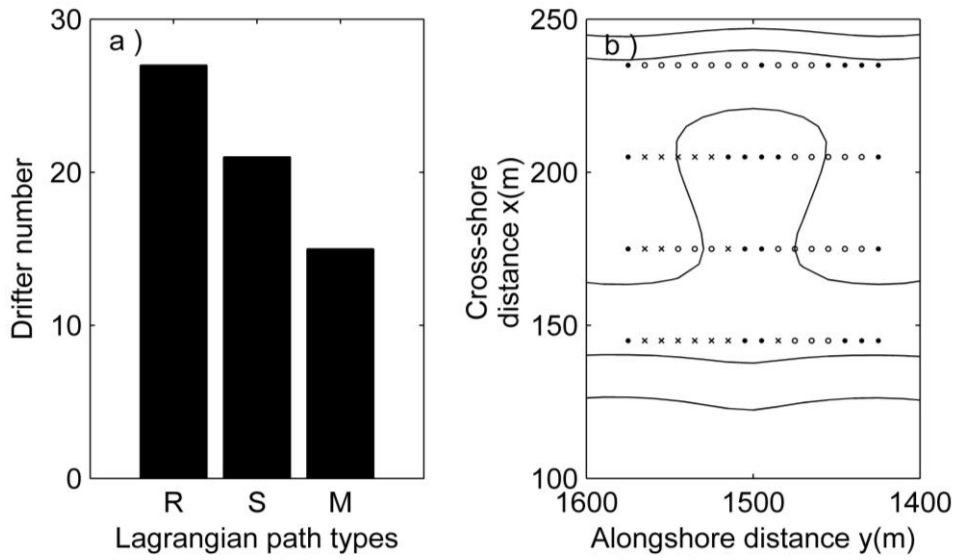

Figure 4.6 The numbers and locations of the three different rip current circulations. The open circles, filled circles and crosses in (b) represent R-, S- and M- type of circulation respectively.

Formation and evolution of rip channels

The morphological evolution processes of rip channels can be derived from Figure 4.7 in which the temporal evolution of growth rate Ω and rip channel three-dimensionality $\|h\|$ are shown. From day 0 to day 1, the growth rate Ω is negative (Figure 4.8a), which suggests the initial perturbation imposed on the alongshore

uniform barred-beach damps. Therefore, no rip channels are produced, which can be also seen from Figure 4.7a and Figure 4.7e. From day 1, the growth rate Ω starts to be positive and increases rapidly. The intense growth of growth rate Ω lasts until

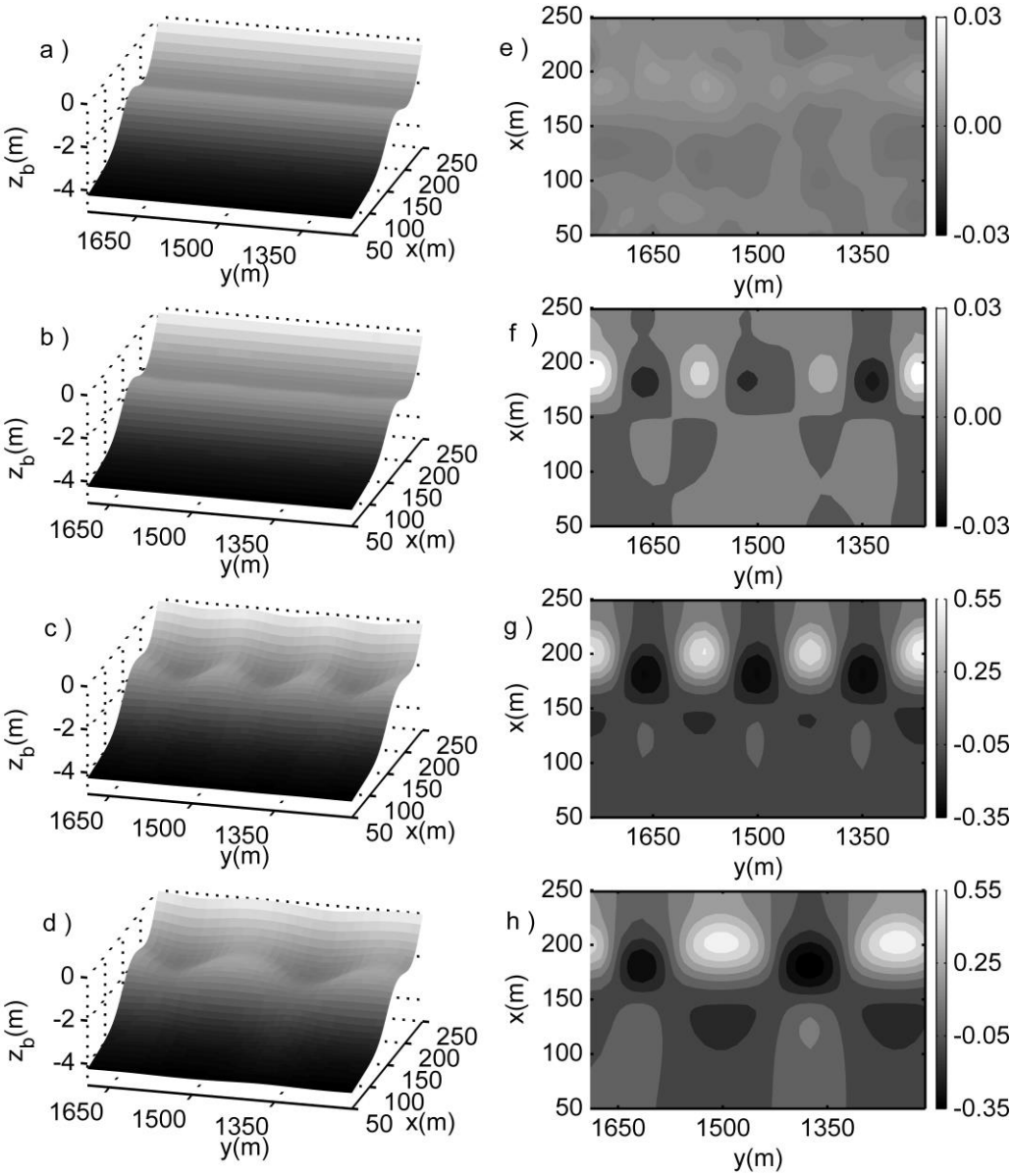

Figure 4.7 The seabed bathymetry (left panel) and bed perturbation (right panel) at day 1 (a and e), day 6 (b and f), day 21.3 (c and g) and day 100 (d and h) of simulation for $H_{rms}^{0} = 1.0\,m,\ \theta^{0} = 0^{\circ}$.

about day 6, the day of which the rip channels reach the namely response time, i.e., $t_r = 6\,days$ for this simulation. The grow rate at this time is denoted as the initial growth rate Ω_1 and is about $0.46\,day^{-1}$. Although the rip channels are still not clear on the snapshot of bathymetry at day 6, they can be already seen in the plot of the bed perturbation, the amplitude of which is about $3\,cm$. From day 6, the rip channel three-dimensionality continues to increase, while the growth rate Ω gradually decreases to nearly zero at day 21.3, i.e., the saturation time $t_s = 21.3\,days$. At this time, the rip channels are both evident from the snapshot of bathymetry and seabed perturbations (Figure 4.7c and Figure 4.7g). The amplitude of rip channel is about $0.45\,m$. From day 21.3 to the end of simulation, growth rate Ω is almost constant around zero and the rip channel three-dimensionality $\|h\|$ is nearly stable, which indicate that the global balance of the whole beach system has been reached. However, the dynamical evolution of shoals and troughs can still exist locally. For instance, merging of single shoals can be found by comparing the bathymetry at day21.3 and day 100, as can be deduced by comparing Figure 4.7c and Figure 4.7d.

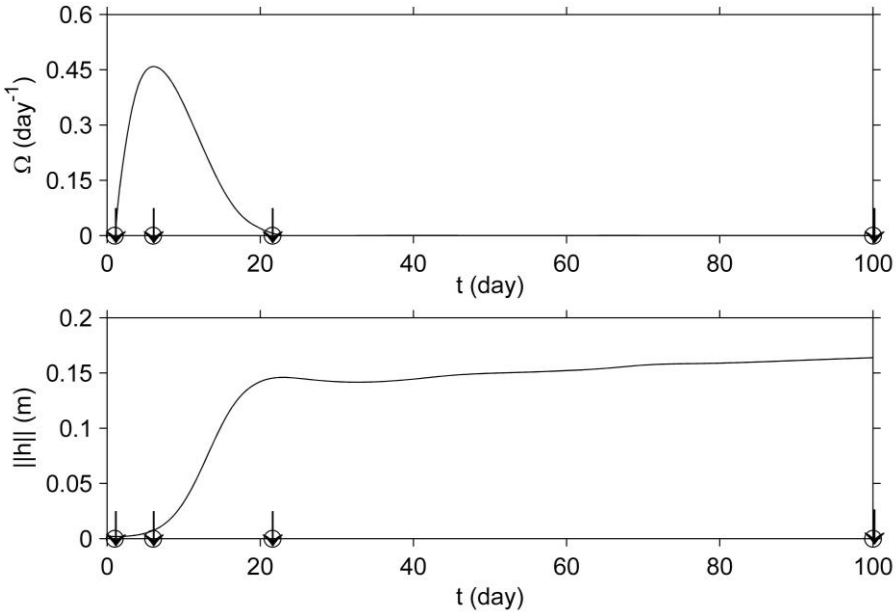

Figure 4.8 The evolution of (a) growth rate and (b) rip channel three-dimensionality for $H^0_{rms} = 1.0\,m,\ \theta^0 = 0^\circ$. The four points denoted by the arrows corresponds to day 1, day 6, day 21.3 and day 100 respectively.

Figure 4.9 gives the temporal evolution of the alongshore bed profile at $x = 190\,m$ and the predominant wavelength λ_m. As we can see from Figure 4.9b, the dominate wavelength of rip channel at the response time, i.e., the initial predominant wavelength $\lambda_1 = 158\,m$. The dominate wavelength increase later from 158 m to $200\,m$. In fact, the increase of dominate wavelength is largely caused by the merging of individual shoals and troughs. From Figure 4.9a, we can see that four merging occur in this simulation, e.g, at around $2800\,m$ at day 20. Figure 4.9a also shows that the rip channel generated under normal incidence waves is non-migration, as shoals and troughs remain parallel to the time axis.

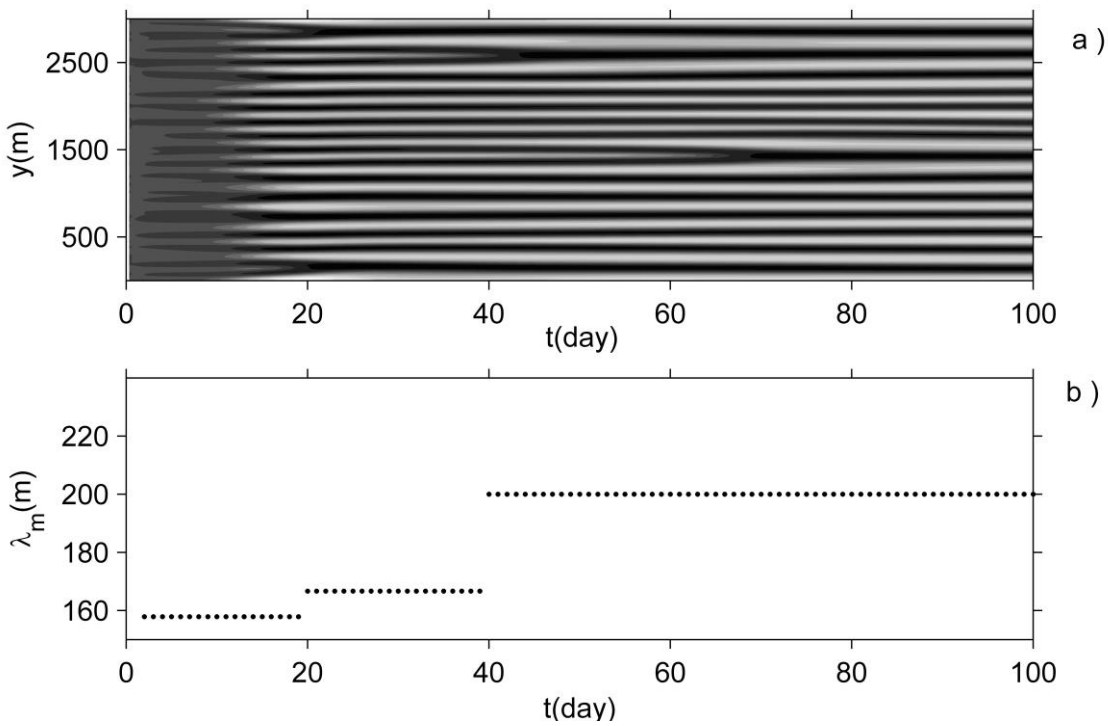

Figure 4.9 The temporal evolution of (a) alongshore bed profile $z_b(190, y, t)$ and (b) the predominant wavelength of rip channels λ_m for $H^0_{rms} = 1.0\,m,\ \theta^0 = 0^\circ$. Darker colours represent deeper areas.

4.4.2 Emergence and dynamics of rip channels under oblique waves

Hydrodynamic and morphological characteristics

Similar to the default simulation under normal waves, the snapshot of bed morphology of the whole modelling domain at the saturation time ($t_s = 28\,day$) for the default simulation under oblique incident wave, i.e., case C5, is displayed in Figure 4.10a. From this figure, we can see that fourteen rip channels exist with a mean wavelength $\lambda_{mean} \approx 214\,m$. Different to the simulation under normal waves, the generated rip channels under oblique waves are not shore-normal but oblique to the shoreline, as the head of shoal at the seaward side locates in the down current direction with respective to the shoreward head of shoal (compare Figure 4.10a and Figure 4.2a). Figure 4.10c gives the spectrum of $|F_z(k_l)|$ for the alongshore bed profile $z_b(190, y, 28)$ and shows that the predominant wavelength of the resulted rip channels at day 28 is $\lambda_m = 230\,m$.

The current circulation and the corresponding vorticity in the area of $100\,m < x < 250\,m$ and $1170\,m < y < 1800\,m$ are displayed in Figure 4.11a and Figure 4.11c respectively. Owing to the wave obliquity, an alongshore uniform current appears on the initial alongshore uniform beaches. Along with the beach evolving, this current is deflected onshore over the shoal and is thrown offshore in the trough, forming a strong rip circulation (Figure 4.11a). From Figure 4.11c, we can see that the four-quadrant circulation pattern is also presented, being similar with that observed in the simulation under normal waves (see Figure 4.3c). However, the circulation cells are now a little oblique to the shoreline, which may be resulted by the alongshore currents that generated by the wave obliquity. In fact, the current pattern close to the shoreline has been changed significantly. For instance, the convergence (divergence) of current over the shoal (trough) area at $230\,\mathrm{m}<x<250\,\mathrm{m}$ and $1500\,\mathrm{m}<y<1800\,\mathrm{m}$ is replaced by current that meandering alongshore (compare Figure 4.3b and Figure 4.11b).

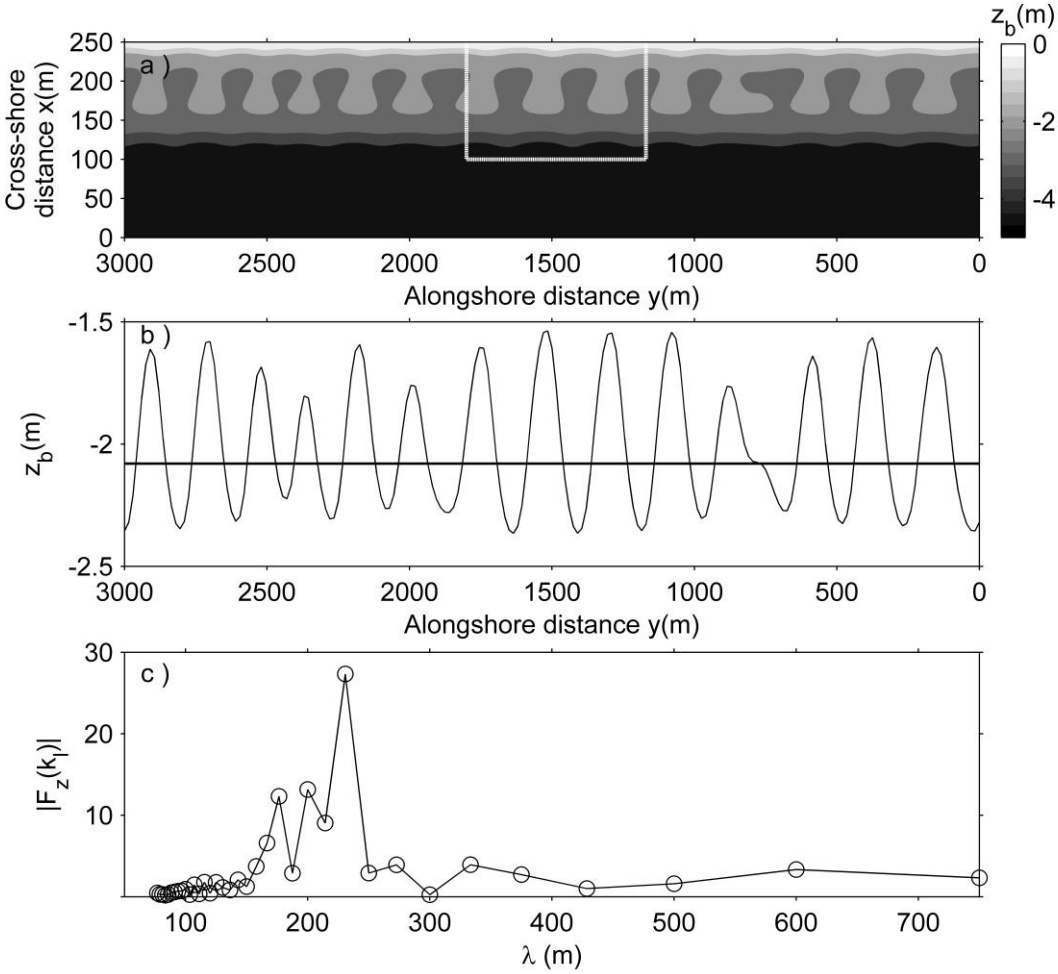

Figure 4.10 (a) Snapshot of rip channel morphology after 28 days of simulation for $H_{rms}^{0} = 1.0\,m,\ \theta^{0} = 4^{\circ}$. (b) The alongshore bed profile at $x = 190\,m$ for day 0 (thick line) and day 28 (thin line). (c) The spectrum of $|F_z(k_l)|$ for $z_b(190, y, 28)$.

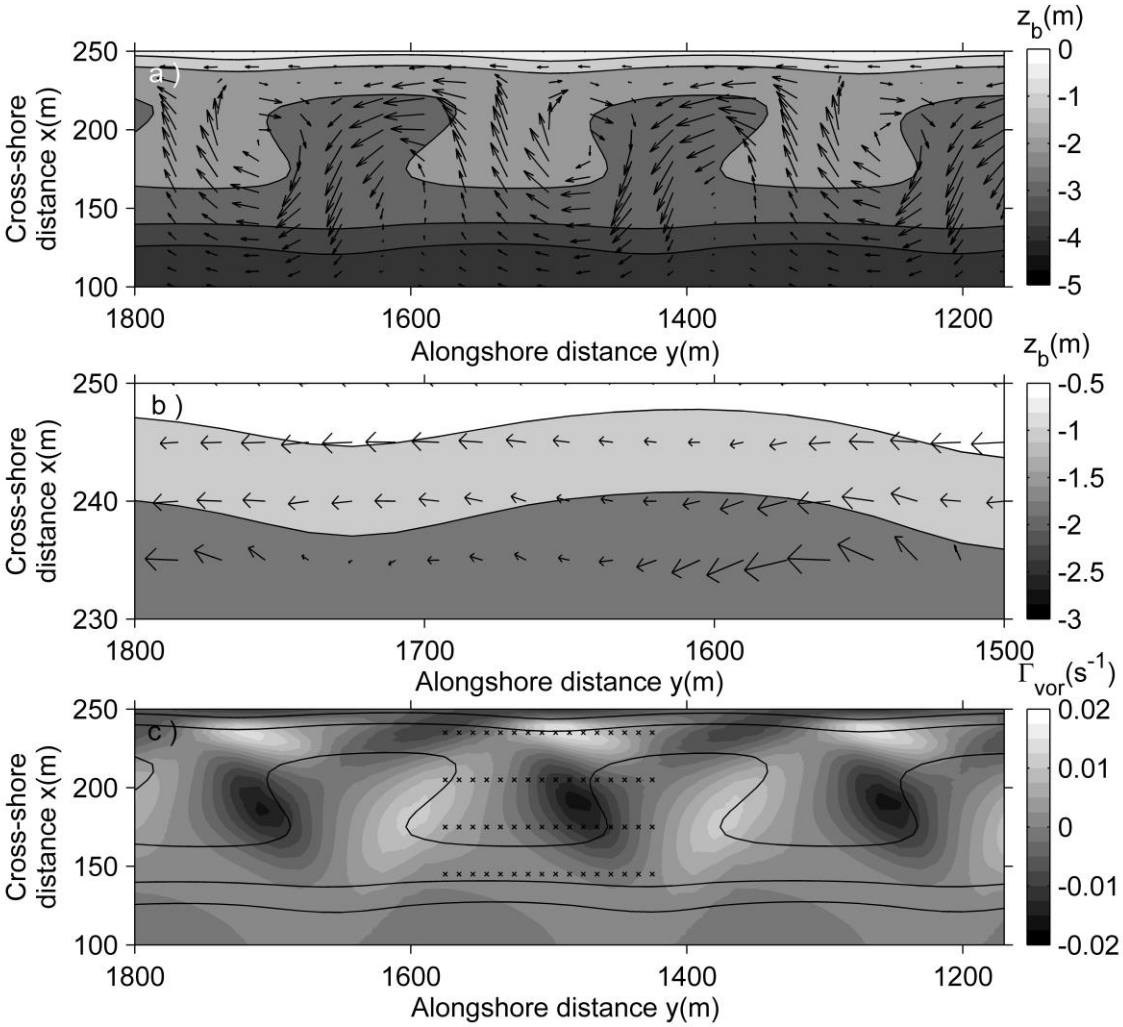

Figure 4.11 The seabed with superimposed currents at day 28 for $H^0_{rms} = 1.0\,m$ and $\theta^0 = 4^\circ$ in the area of (a) 100 m<x<250 m and 1170 m<y<1800 m and (b) 230 m<x<250 m and 1500 m<y<1800 m. (c)The vorticity corresponds to (a).

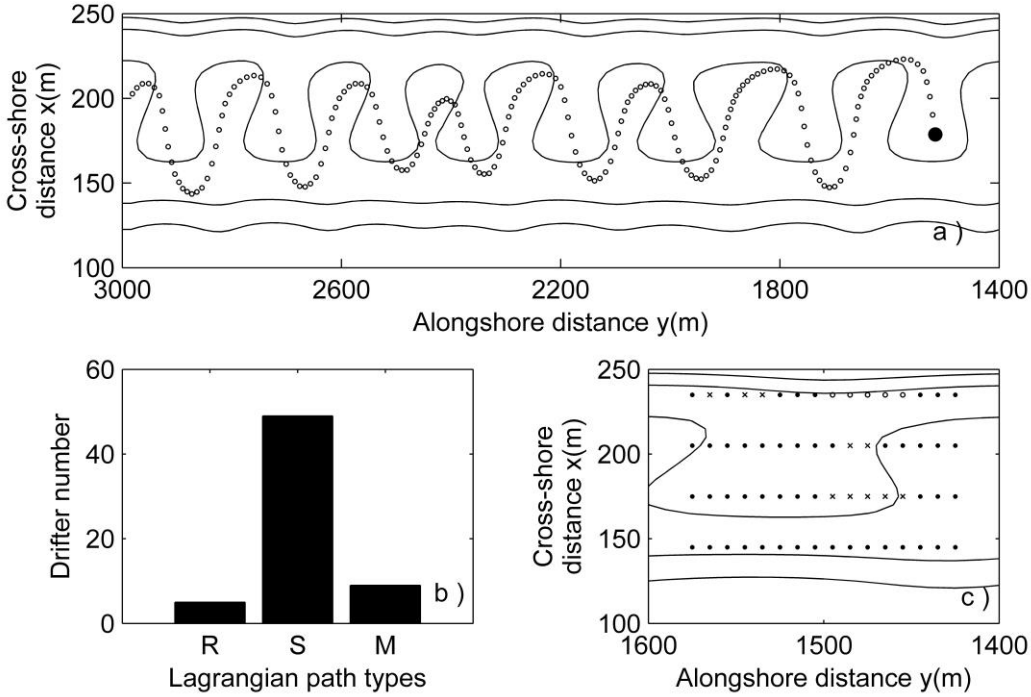

Figure 4.12 Hydrodynamic experiment for $H_{rms}^{0} = 1.0\,m,\ \theta^{0} = 4^{\circ}$. (a) Lagrangian path of drifter with its origin at $x = 170\,m,\ y = 1485\,m$ (filled circle). (b) Numbers and (c) spatial distribution of drifters for three types of rip current circulations. The open circles, filled circles and crosses in (b) represent R-, S- and M- type of circulation respectively.

The Lagrangian behaviour of current circulation under oblique waves is quite different to that under normal waves. As can been seen from Figure 4.12b, the number of drifter paths that fall into the sinuous alongshore current type is 49, which overwhelm the drifter paths falling into the other two types of current circulations. Spatially, the R-type drifters only exist around the center of the inner circulation cell, while the S-type drifters spread over both shoals and troughs (Figure 4.12c). Moreover, the alongshore migration ability of S-type and M-type drifters are more vigorous under oblique waves comparing to that under normal waves. For instance, the S-type drifters can migrate alongshore more than $1500\,m$, while they move only about $400\,m$ under normal waves.

Formation and evolution of rip channels

The temporal evolution of growth rate Ω and rip channel three-dimensionality $\|h\|$ for the default simulation under oblique waves (case C5) is displayed in Figure 4.13. Meanwhile, the snapshots of bathymetry and bed perturbation at four selected time steps are given in Figure 4.14. These two figures clearly reveal the morphological evolution of rip channels for the default simulation under oblique waves.

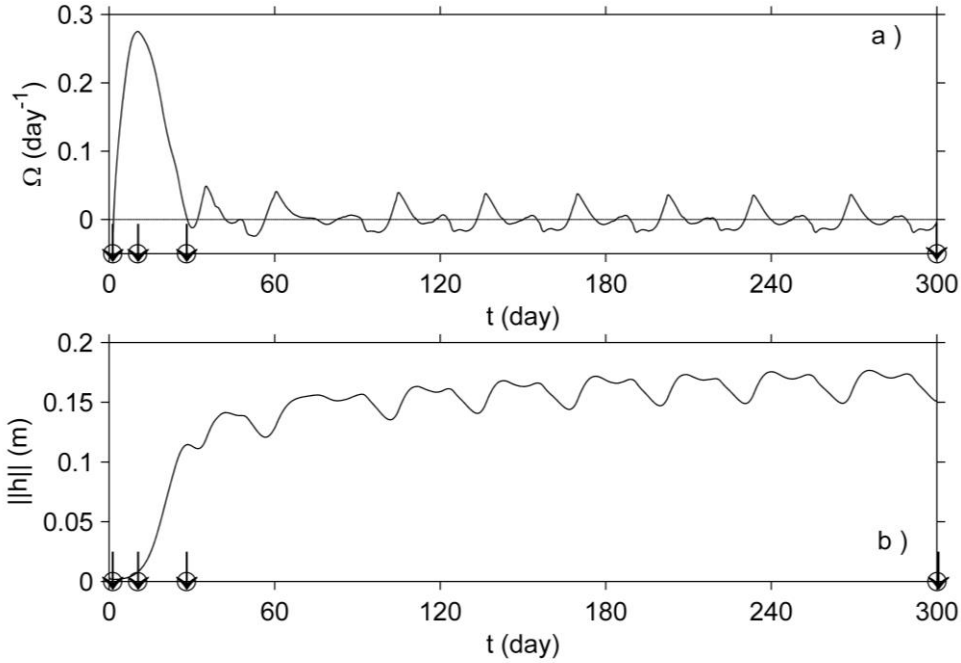

Figure 4.13 The evolution of (a) growth rate and (b) rip channel three-dimensionality. The four points denoted by the arrows corresponds to day 1.3, day 10.3, day 28 and day 300 respectively.

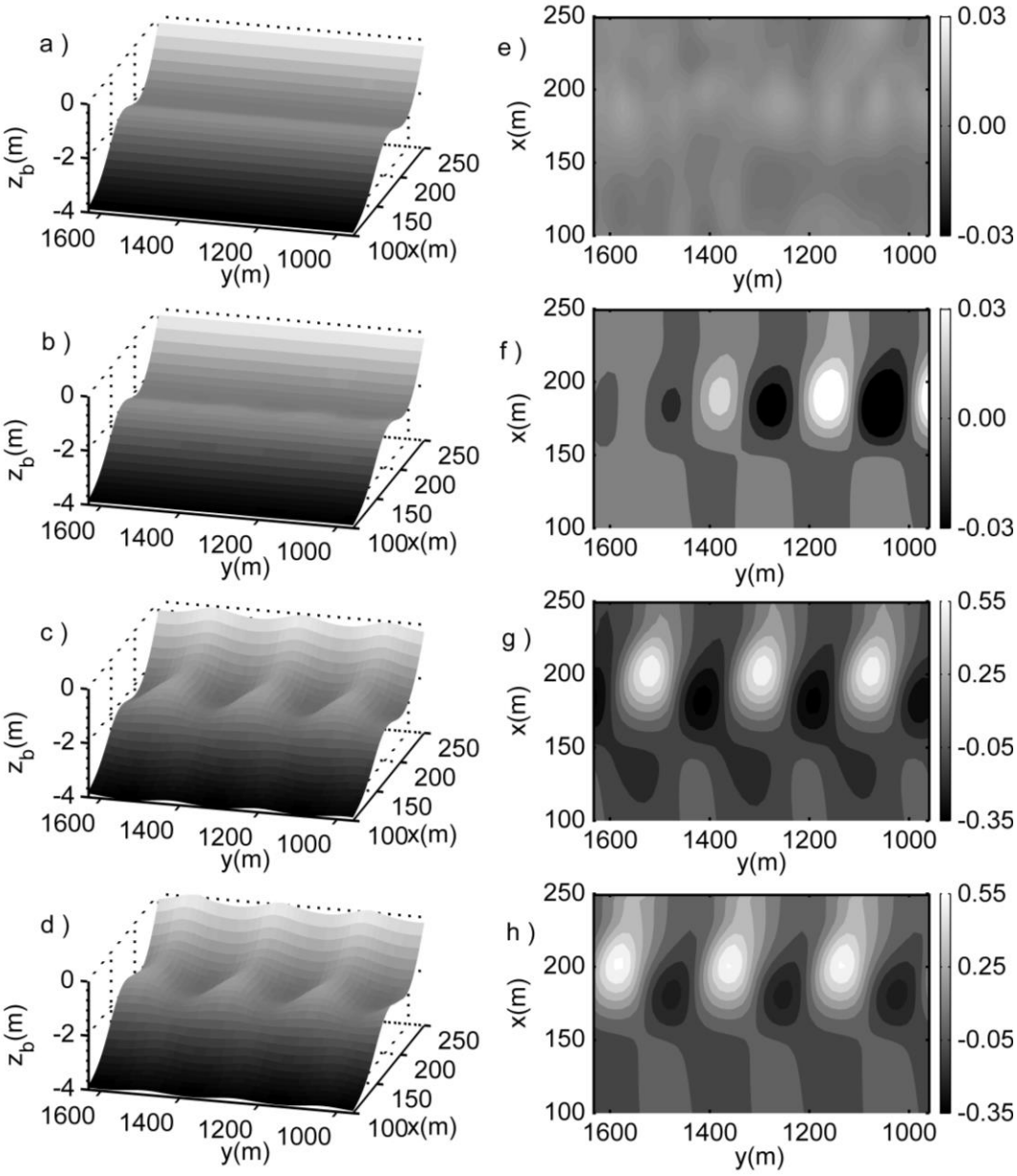

Figure 4.14 The seabed bathymetry (left panel) and bed perturbation (right panel) at day 1.3 (a and e), day 10.3 (b and f), day 28 (c and g) and day 300 (d and h) of simulation with $H_{rms}^{0} = 1.0\ m,\ \theta^{0} = 4^{\circ}$.

Similar to the default simulation under normal waves, the rip channels not emerge in the first several days (Figure 4.14a and Figure 4.14e), as initially the growth rate is negative. This negative growth rate suggests that the amplitude of the initial added perturbation decreases. From day 1.3 to day 10.3, the growth rate increase intensely

and finally reach its peak at $t_r = 10.3\,day$ with the initial growth rate $\Omega_1 = 0.28\,day^{-1}$. At day 10.3, it can be found that the rip channels have already emerged from the initial patternless seabed (see Figure 4.14f). In addition, Figure 4.14f reveal that the emerged rip channels are not normal to the shoreline. From day 10.3, the growth rate Ω gradually decreases and reaches nearly zero at $t_s = 28\,day$, while at the same time the rip channel three-dimensionality increase significantly. From Figure 4.14g, we can see that the obliquity of rip channels is more obvious than that in Figure 4.14f. In addition, we find that the trough and shoals at the seaside of the sandbar present an up-current orientation, which is opposite to the orientation of troughs and shoals in the shoreward side of the sandbar. It should be noted that the same orientation pattern has also been reported in the previous modelling studies (e.g., Garnier et al., 2008; Thiébot et al., 2012).

Comparing to the morphological evolution processes before the saturation time (in terms of the evolution of growth rate and rip channel three-dimensionality) for the default simulations under normal and oblique waves (as that presented in Figure 4.8 and Figure 4.13), we can find that despite the exact value of growth rate and rip channel three-dimensionality is not the same, the general trend of the evolution of growth rate and rip channel three-dimensionality are same for the normal and oblique waves. Specifically, the growth rate first increases to reach the peak (i.e., the initial growth rate) and then decreases to almost zero, while the rip channel three-dimensionality continues to increase and finally reach its maximum value at the saturation time. However, the variation trend of growth rate and rip channel three-dimensionality is not the same for normal and oblique waves after the saturation time. For normal waves, the growth rate is nearly constant to be zero (Figure 4.8a) and the rip channel three-dimensionality keeps almost stable (Figure 4.8b). But for oblique waves, the growth rate is perturbed around zero (Figure 4.13a). Simultaneously, the rip channel three-dimensionality is not stable (Figure 4.13b), which decreases when the growth rate is negative and increases when the growth rate is positive.

Figure 4.15a gives the temporal evolution of the bed level at the alongshore section $x = 190\,m$. We can see from this figure that the trajectories of shoals and

troughs of rip channels are no longer parallel to the time axis, which reveals the rip channels generated under oblique waves can migrate in the alongshore direction. Therefore, it is not the same to the non-migration rip channels that formed under normal incident waves. In the present case, the generated rip channels migrate with a speed of about $c_m = 7\ m\ day^{-1}$ towards the down-current direction. Figure 4.15b shows the evolution of the predominant wavelength of rip channel λ_m. In the present case, the predominant wavelength is 231 m, which dominants until the end of simulation.

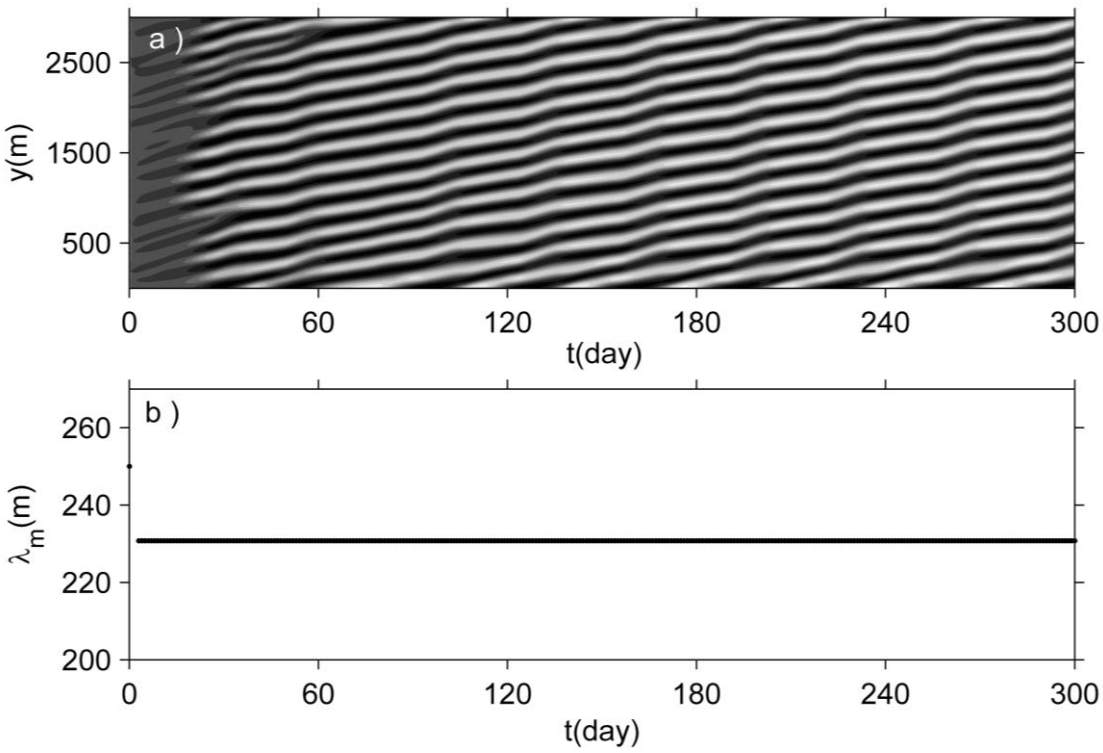

Figure 4.15 The temporal evolution of (a) alongshore bed profile $z_b(190, y, t)$ and (b) the predominant wavelength of rip channels λ_m for $H^0_{rms} = 1.0\ m,\ \theta^0 = 4^\circ$. Darker colours represent deeper areas.

4.5 Discussion

4.5.1 Comparison with field observations and previous numerical studies

The values of rip channel response indicators predicted by the modified XBeach model for the eight simulations carried out here are listed in Table 4.2. Specifically, the indicators listed in this table include Ω_1, t_r, t_s λ_1, $A_{\max}$, c_m, $\|h\|$,and λ_m / W_{bar}. It should be noted that the rip channel wavelength used here equals to the initial predominant wavelength λ_1. $\|h\|$ and $A_{\max}$ is obtained at the saturation time rather than at the end of simulation, which is to improve the comparability of results by avoiding the nonlinear dynamics after saturation time. λ_m / W_{bar} is the ratio of rip channel wavelength to its offshore distance W_{bar}, which is a common indicator used in the field observation of rip channels (van Enckevort et al., 2004).

From this table, we can see that the predicted predominant wavelength of rip channels is between 158 m to 333 m, which is quite consistent with the observed length of rip channels from the Duck beach, USA (i.e., about 250 m, see detail in van Enckevort et al., 2004). Furthermore, The predicted value of the ratio between wavelength and the offshore distance of rip channels are ranged in 2-4, which falls within the range of value that obtained from the fields (between 1 to 10).

In addition, Table 4.2 also gives a detailed comparison of the predicted rip channel response indicators for the two default simulations (i.e., case C2 and C5) using XBeach and MORFO55 model, respectively. Overall, the predictions from these two models agree very well, in terms of the growth rate, predominant wavelength of rip channel, rip channel amplitude. However, the migration speed predicted by XBeach is obviously smaller (less than half) than that predicted by MORFO55. Although not sufficient in demonstrating the superiority of XBeach model it is of interest to note that MORFO55 model was often found to over-predict the migration speed compared to that observed in the field (Garnier et al., 2006; Ribas and Kroon, 2007).

Table 4.2 The values of rip channel response indicators for the eight simulations

Case No	H^0_{rms} (m)	θ^0 (deg)	Ω_1 (day^{-1})	t_r (day)	t_s (day)	λ_1 (m)	$\|\| h \|\|$ (m)	$A_{\max}$ (m)	c_m $(m\ day^{-1})$	λ_m / W_{bar}
C1	0.8	0	0.15	14.67	46.00	158	0.06	0.4	0	2
C2	1	0	0.46 **(0.55)**	6.00	21.33	158 **(180)**	0.15	0.52 **(0.44)**	0 **(0)**	2
C3	1.2	0	0.66	4.67	16.00	158	0.18	0.65	0	2
C4	1	2	0.37	8.00	22.00	176	0.13	0.53	3.49	2
C5	1	4	0.27 **(0.20)**	10.33	28.00	231 **(220)**	0.11	0.56 **(0.44)**	6.92 **(21)**	3
C6	1	6	0.20	15.33	35.67	231	0.11	0.51	9.65	3
C7	1	8	0.14	21.67	50.33	273	0.11	0.50	10.08	3
C8	1	10	0.09	29	71.67	333	0.09	0.44	12.4	4

Note the values in brackets are that predicted by Garnier et al.(2008) using MORFO55.

Despite the response time and saturation time was not reported directly in the study of (Garnier et al., 2008), these values can be estimated from the rip channel three-dimensionality evolution curve in Figure4d in their study (Garnier et al., 2008). Roughly, the estimated saturation time in Garnier et al. (2008) is about 30 days, which is actually similar to the saturation time obtained here.

It is important to note that the predicted response time and saturation time seems is large compared to that observed in field. Nowadays, the best technology to track the formation and evolution of rip channels in field is the digital imaging technology, shore-based video techniques like the Argus system (Smit et al., 2007). However, even adopting this kind of technology, it is still difficult to obtain high quality estimation on the response time and saturation time, which is partly because the Argus technology is highly influenced by the illuminating condition and weather condition. Fortunately, it is not difficult to estimate the residence time of the morphological patterns from the Argus system. The residence time is the time length of a given morphological pattern can survive before it disappears and transits into another type of morphological pattern, which can be estimated by qualitatively comparing Argus image from different times. This time scale varies from one site to another.

Previous field observations (Lippmann and Holman, 1990; Ranasinghe et al., 2004) show that the residue time for LBT beach is generally 1 to 5 days, while for the Duck beach, it is only about 2 days. This means that beginning from the alongshore uniform barred beach (LBT state) the rip channel may become observable in about 2 days. However, it can be seen from Figure 4.8b and Figure 4.8f that even for the normal waves, under which the growth rate is large comparing to that under oblique waves, the rip channel is still not quite easy to be detected after 6 days evolution and their amplitude is only about 3 cm. Therefore, it is reasonable to conclude that the response time and saturation time predicted here is large comparing to the one exist in field. Garnier et al. (2008) ascribed this mismatching in rip channel growth time between numerical model and field observation to ignoring the existence of previous rhythmic morphological features like ripples. However, our simulations designed to

investigate the effects of sediment size, as given in the following chapters, reveal that this mismatching can also be explained in the perspective of sediment size. The detail of this explanation will be presented in the following chapters, at which this point will be revisited.

4.5.2 Dynamical equilibrium

Our simulations present here show that the process to reach the equilibrium state is complex and may only approximately reached, which is in line with previous studies (Garnier et al., 2006; Garnier et al., 2008; Klein and Schuttelaars, 2005). As can be seen from Figure 4.9, the equilibrium state of rip channel system has been reached. However, this equilibrium is 'dynamical', which means that the single shoals and trough may still be in movement and can merge or split, while the whole system is nearly stabilized. Under oblique waves, we find that the growth rate is not stable but oscillates around zero. In fact, this type of oscillation has also been reported in the study of oblique bars near the shoreline, which is carried out by Garnier et al. (2006). Besides the oscillation occurs in growth rate, Garnier et al. (2008) reported that the predominant wavelength of rip channels for oblique waves is not stable after the saturation time. Although this change in predominant wavelength does not appears in our default case for oblique waves as presented in Figure 4.13, it is actually occur in our simulations carried out here as well. For instance, when the wave angle at the sea boundary is set to $6°$, the predominant wavelength of rip channel λ_m is $230\,m$, which dominates until ~130 days. Then, it can be seen that the predominant wavelength λ_m fluctuates around $230\,m$ to $272\,m$ and does not show a trend to stabilize (Figure 4.16).

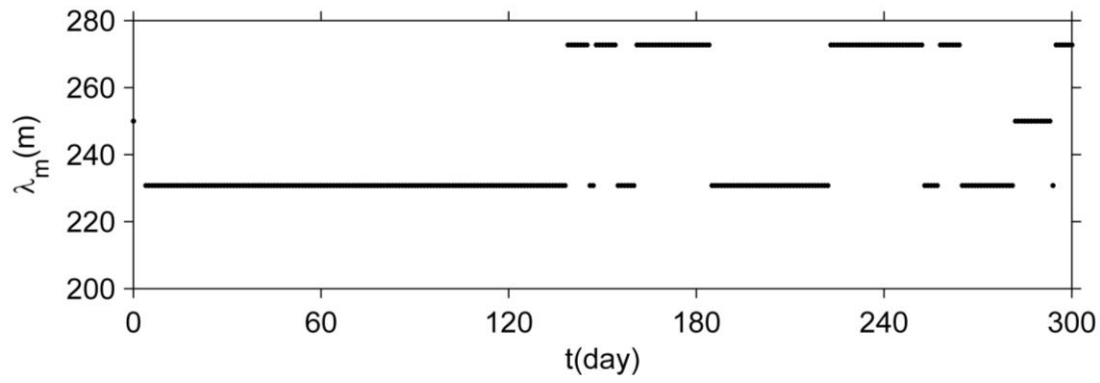

Figure 4.16 The temporal evolution of the predominant wavelength of rip channels λ_m for $H_{rms}^0 = 1.0\,m,\ \theta^0 = 6^\circ$.

4.6 Summary

In this chapter, the modified XBeach model has been used to simulate the long-term morphodynamic evolution of rip channels through self-organisation mechanism on a barred beach. Within the model framework used here, the emergence of rip channels from initially patternless barred beach has been successfully generated, which is resulted from the interaction of seabed bathymetry and hydrodynamic conditions, i.e., from self-organization mechanism. The typical morphodynamic behaviours of rip channels, such as the merging/ splitting and alongshore migration of rip channels, have also been well reproduced. A detailed comparison of the prediction from the modified XBeach model and the previous widely used numerical model MORFO55 shows that the dynamical and geometrical properties of rip channels predicted by the modified XBeach model are consistent with that predicted by MORFO55, with the predicted migration speed is much closer to the field observation. Therefore, it is reasonably to conclude that the XBeach model within the established modelling framework as used here can be an effective modelling tool in studying the self-organization behaviour of rip channels.

Chapter 5

The grain size effects on rip channel dynamics for beach with uniform sediment

5.1 Introduction

In nature, beach sediments are seldom uniform and their grain size may vary significantly through various temporal and spatial scales (Gallagher et al., 2011; MacMahan et al., 2005; Short, 1985). However, before tackling such more complex problem involving variation of sediment distribution a beach consists of sediments that can be characterised by a single median size needs to be firstly understood.

Although Calvete et al. (2005) has pointed out that the sediment size is important to the dynamics of rip channels, their work is limited to normal incident waves and the initial evolution of rip channels. Similar conclusion was reached by Smit et al. (2008) based on a nonlinear morphodynamic model. However, neither work has provided a full account of the role of sediment size on the properties of saturation and nonlinear dynamics of rip channels.

In this chapter, the modified XBeach model is applied to investigate the impact of changing median grain size on the formation and evolution of rip channels on a barred beach, covering both the key geometrical properties of rip channels and their overall evolution characteristics.

This chapter is organized as follow: in Section 5.2, the configurations of numerical experiments are illustrated. In Section 5.3 the main results of numerical simulations are presented and comprehensive analysis on the sediment size effects are conducted. A discussion on the modelling results is given in Section 5.4. The summary of this chapter is drawn in section 5.5.

5.2 Model set-up

As mentioned in Chapter 4, there are eight simulations using eight different hydrodynamic conditions carried out in Chapter 4. In this Chapter, these simulations are extended by changing the sediment size. For each hydrodynamic condition, twelve different grain sizes covering the range of sediments from very fine to very coarse sand, i.e., [0.1 0.18 0.25 0.28 0.31 0.35 0.41 0.5 0.6 0.71 1.2 1.5] mm, are applied. Therefore, 96 simulations in total are carried out here. The other modelling configurations such as the initial beach bathymetry and computational domain are exactly same as that used in Chapter 4.

Table 5.1 Input parameters for six representative simulations

Case No	H_{rms}^{0} (m)	θ^{0} (deg)	T (s)	Simulation timelength (day)	d_g (mm)
S1	1	0	9	100	0.18
S2	1	0	9	100	0.25
S3	1	0	9	100	0.71
S4	1	6	9	300	0.18
S5	1	6	9	300	0.25
S6	1	6	9	300	0.71

Among these 96 simulations, six simulations that using three different sediment grain sizes and two different wave conditions are selected as representative simulations to demonstrate the effects of sediment size on the temporal evolution of rip channels. Specifically, the three selected grain sizes of sediment are $d_g = 0.18\,mm$, $0.25\,mm$, $0.71\,mm$, respectively. The two selected offshore wave

conditions are $H_{rms}^{0} = 1.0\,m, \theta^{0} = 0^{\circ}$ and $H_{rms}^{0} = 1.0\,m, \theta^{0} = 6^{\circ}$. The detail input parameters for these six simulations are listed in Table 5.1.

5.3 Modeling results

5.3.1 Rip channel temporal evolution for different sediment sizes

The growth rate evolution for the three selected sediment grain size with $H_{rms}^{0} = 1.0\,m$ and $\theta^{0} = 0^{\circ}$, i.e., case S1, S2 and S3, are shown in Figure 5.1a. It can be seen that the general trend of growth rate Ω for different sediment size is the same, i.e., the growth rate increases first and then decrease gradually to about zero after reaching the peak. Finally, the growth rate is stable, which remains nearly constant until the end of simulation. The maximum growth rate is 0.55 day^{-1} for $d_g = 0.18\,mm$, which is larger than that for $d_g = 0.25\,mm$ (0.46 day^{-1}) and $d_g = 0.71\,mm$ (0.27 day^{-1}). Meanwhile, the response time and saturation time for $d_g = 0.18\,mm$ ($t_r = 5.3\,day$ and $t_s = 18\,day$) are both smaller than that for $d_g = 0.25\,mm$ ($t_r = 6\,day,\ t_s = 21.3\,day$) and $d_g = 0.71\,mm$ ($t_r = 8.3\,day$ and $t_s = 35\,day$).

Figure 5.1b gives a detailed comparison of rip channel three-dimensionality evolution for the three simulations under $H_{rms}^{0} = 1.0\,m$ and $\theta^{0} = 0^{\circ}$. It shows that the rip channel three-dimensionality $\| h \|$ is largest for $d_g = 0.18\,mm$ and smallest for $d_g = 0.71\,mm$, which lasts until ~30 days. After this time, rip channel three-dimensionality $\| h \|$ for $d_g = 0.71\,mm$ exceeds that for the other two sediment sizes and becomes the largest. Notice that rip channel three-dimensionality $\| h \|$ at the response time is very small (less than 10%) for all cases compared to that at the saturation time.

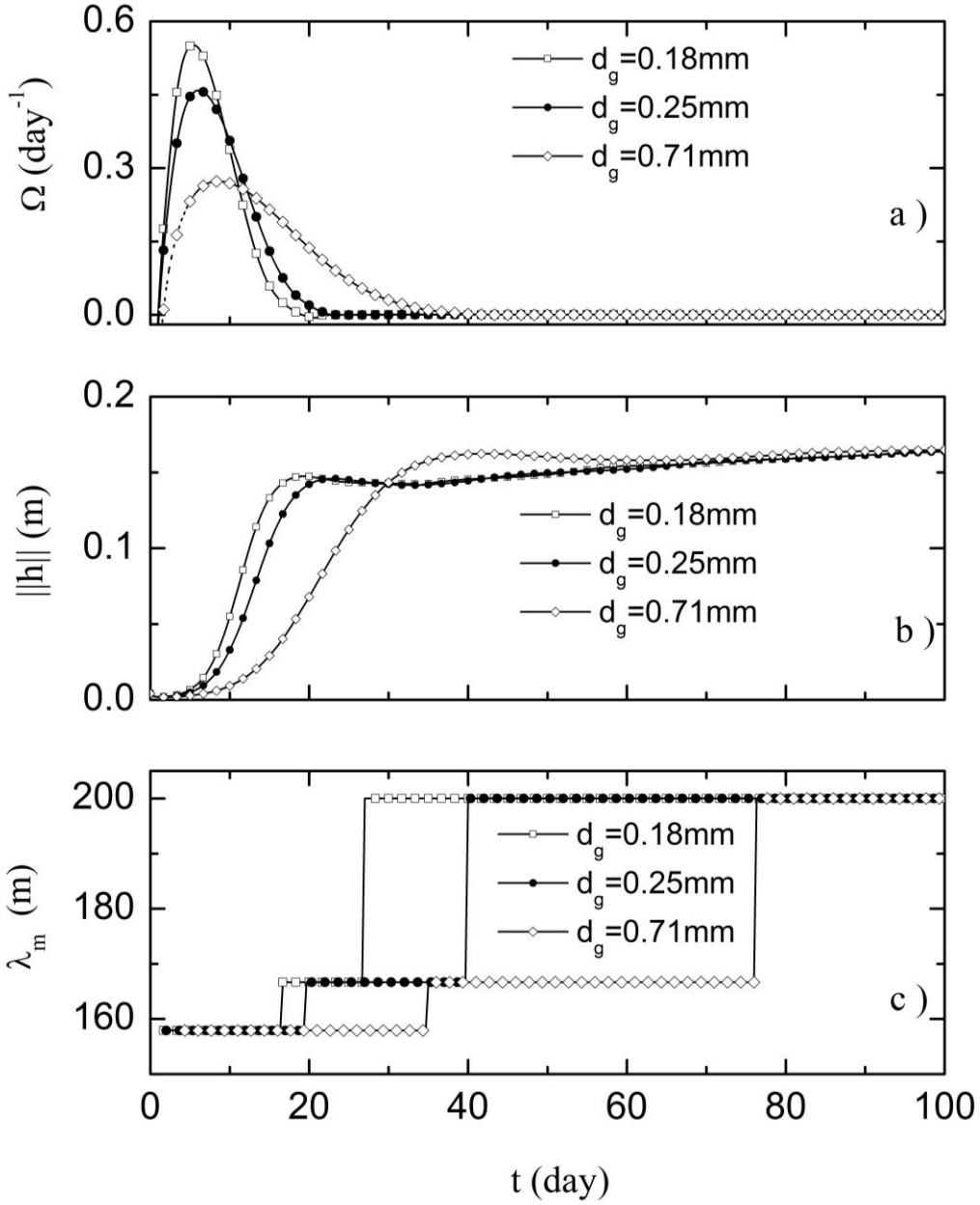

Figure 5.1 Temporal evolution of (a) growth rate, (b) rip channel three-dimensionality and (c) the predominant spacing for different sediment grain size with $H_{rms}^{0} = 1.0\,m, \theta = 0^{\circ}$.

Figure 5.1c shows that the evolution of predominant wavelength is similar for different sediment sizes under $H_{rms}^{0} = 1.0\,m$ and $\theta^{0} = 0^{\circ}$: it increases from $158\,m$ at the initial stage to $200\,m$ at the end of simulation.

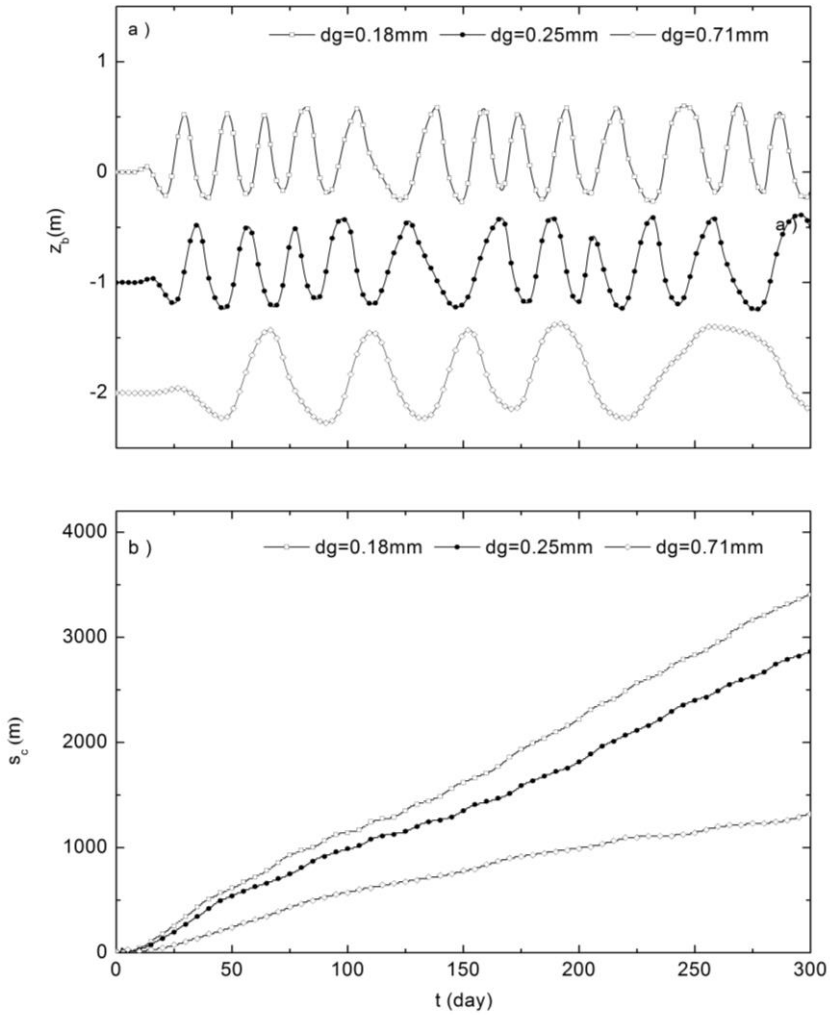

Figure 5.2 Temporal evolution of (a) the bed level at $(x, y) = (190\text{m}, 1500\text{m})$ and (b) the selected shoal crest position for different sediment grain size with $H_{rms}^{0} = 1.0\,m$ and $\theta^{0} = 6^{\circ}$. Note that the bed level $z_b(190, 1500, t)$ in (a) has been shifted $1\,m$ and $2\,m$ downward for $d_g = 0.25\,mm$ and $d_g = 0.71\,mm$ respectively.

Figure 5.2 illustrates the response of rip channels migration property to the sediment grain size. The temporal variation of bed level $z_b(190,1500,t)$ for simulations with the three selected sediment size is shown in Figure 5.2a. From this figure, we can see that the migration speed is largest for $d_g = 0.18\,mm$ followed by that for $d_g = 0.25\,mm$ and $d_g = 0.71\,mm$, as evidenced from the number of bed level

oscillation. In fact, the migration speed can be further quantified from Figure 5.2b, in which the trajectories of selected shoal crest S_c over the simulation period are displayed. In the modelled 300 days, the selected bar crest migrates 3405 m for $d_g = 0.18\,mm$, 2865 m for $d_g = 0.25\,mm$ and 1320 m for $d_g = 0.71\,mm$, respectively. Thus, the migration speed is 11.4 m/day for $d_g = 0.18\,mm$, 9.7 m/day for $d_g = 0.25\,mm$ and 4.4 m/day for $d_g = 0.71\,mm$.

5.3.2 Parameter trend of rip channel response indicators

The variation trend of rip channel response indicators for all 96 simulations are analyzed. Except for the response time t_r and saturation time t_s , the other rip channel response indicators need to be specified at what time their values are used. In the present study, for growth rate and predominant wavelength of rip channels, their values at the response time are selected, denoting as the initial growth rate Ω_1 and initial predominant wavelength λ_1 . The choice of the initial growth rate Ω_1 is because it is the peak of growth rate evolution curve and can serves as a representative for the entire growth rate evolution curve. The choice of initial predominant wavelength λ_1 rather than the end of simulation is because such choice can avoid the complex variation of wavelength caused by the unexpected merging and splitting of individual shoals and troughs and increase the comparability. Similarly, the rip channel three-dimensionality at the saturation time $\| h \|_{ts}$ is chose rather than choosing the value at the end of simulation. The mean migration speed over the whole modeling temporal length is chosen to represent the migration speed.

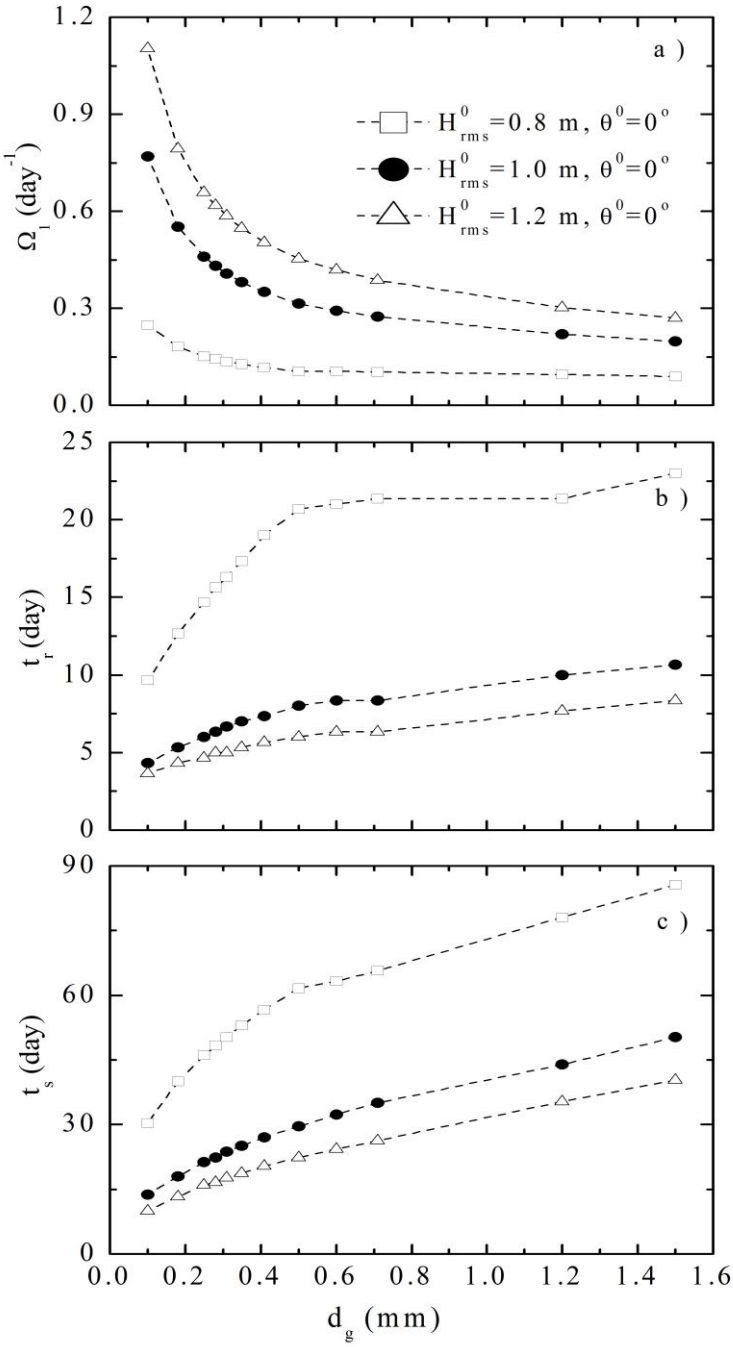

Figure 5.3 Sensitivity of rip channel dynamical characteristics to sediment grain size for $\theta^0 = 0^\circ$. (a) Initial growth rate, (b) response time and (c) saturation time.

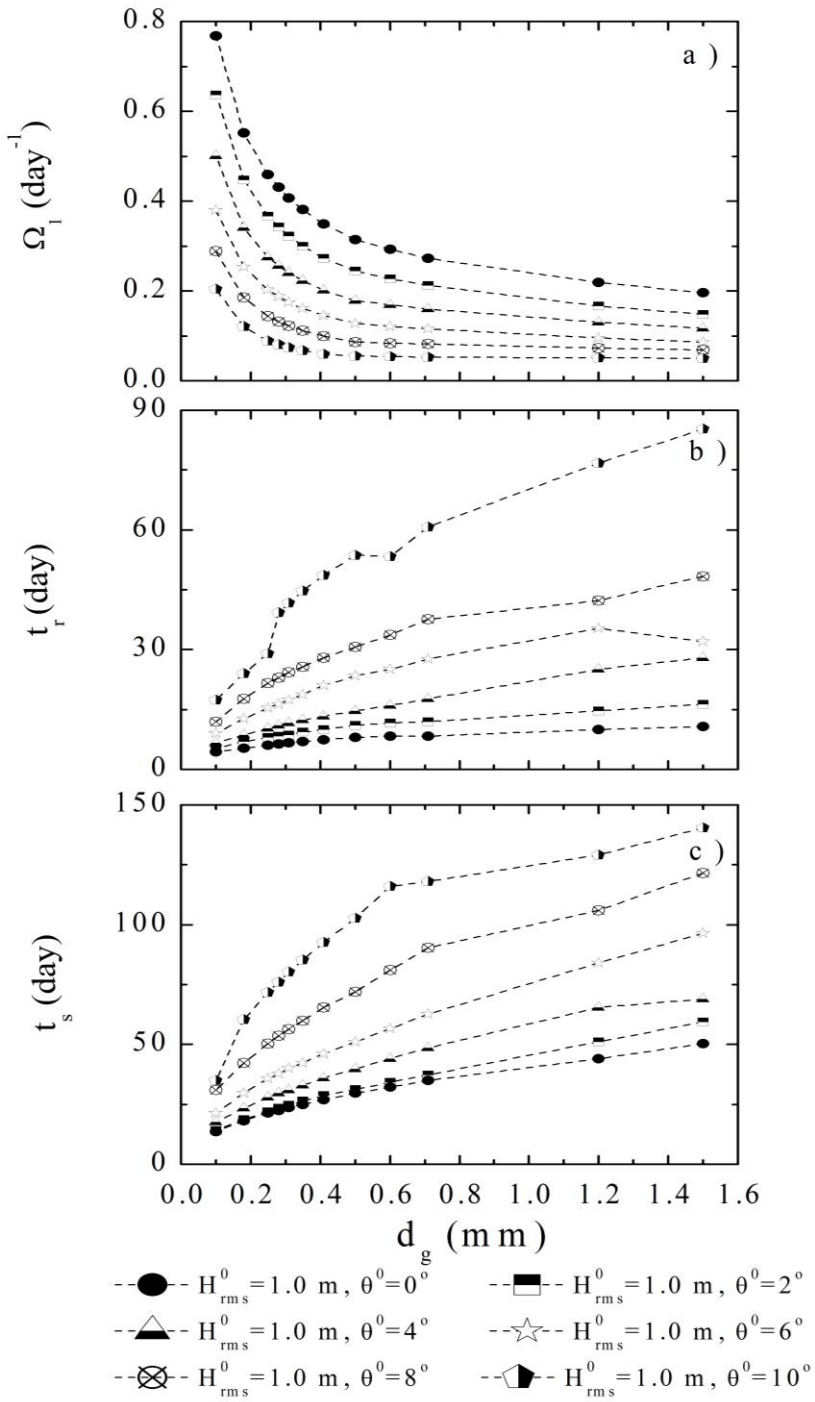

Figure 5.4 Sensitivity of rip channel dynamical characteristics to sediment grain size for $H^0_{rms} = 1.0\,m$. (a) Initial growth rate, (b) response time and (c) saturation time.

The indicators that represent the temporal evolution of rip channel for all 96 simulations are shown in Figure 5.3 and Figure 5.4 as a function of the sediment grain size. As can be seen from Figure 5.3a and Figure 5.4a, the grain size has a strong impact on the initial grow rate Ω_1 for both normal and oblique incident waves, which decreases markedly with increasing grain size. Keeping grain size the same, the initial growth rate Ω_1 increases with either increasing H^0_{rms} or decreasing θ^0, the trend of which broadly agrees with previous modelling studies (Calvete et al., 2005; Garnier et al., 2008). The variation trends for response time t_r (Figure 5.3b and Figure 5.4b) and saturation time t_s (Figure 5.3c and Figure 5.4c) are similar, both of which have opposite trends to that of the initial growth rate Ω_1. The large response time and saturation time tend to be associated with small wave height, coarse sediment and large wave obliquity. This finding that both response time and saturation time increase with increasing wave obliquity is also in agreement with modelling results of Castelle and Ruessink (2011) and Smit et al. (2008).

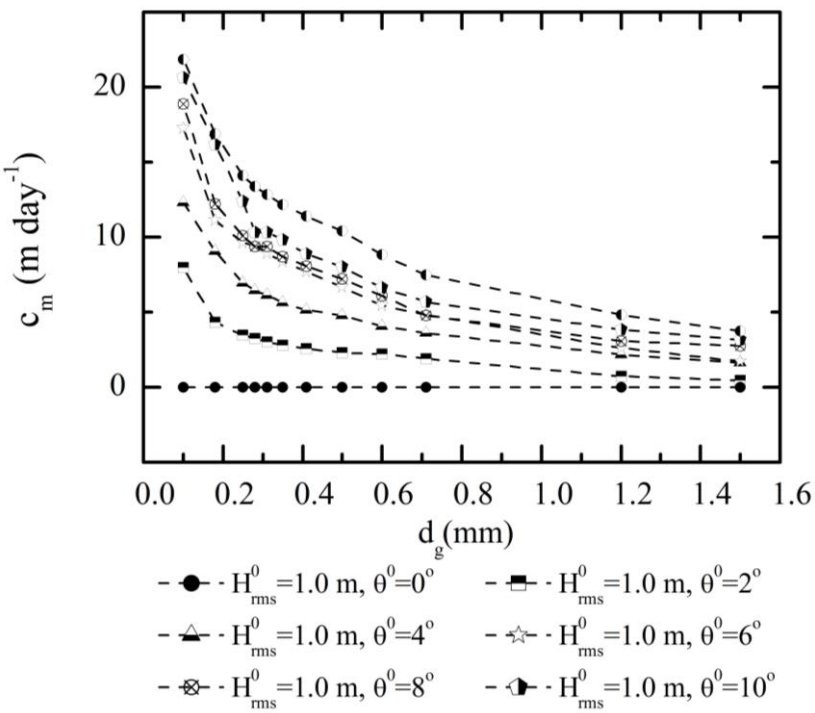

Figure 5.5 Sensitivity of migration speed to sediment grain size and offshore wave conditions.

Moreover, a notable dependence of migration speed on sediment grain size can be seen from Figure 5.5. Under the same wave conditions, migration speed can be an order lager for fine sediment than that for coarse sediment. For instance, in the case of $\theta^0 = 6^o$ the migration speed is 17 m/day for $d_g = 0.1\,mm$ and is only 1.7 m/day for $d_g = 1.5\,mm$.

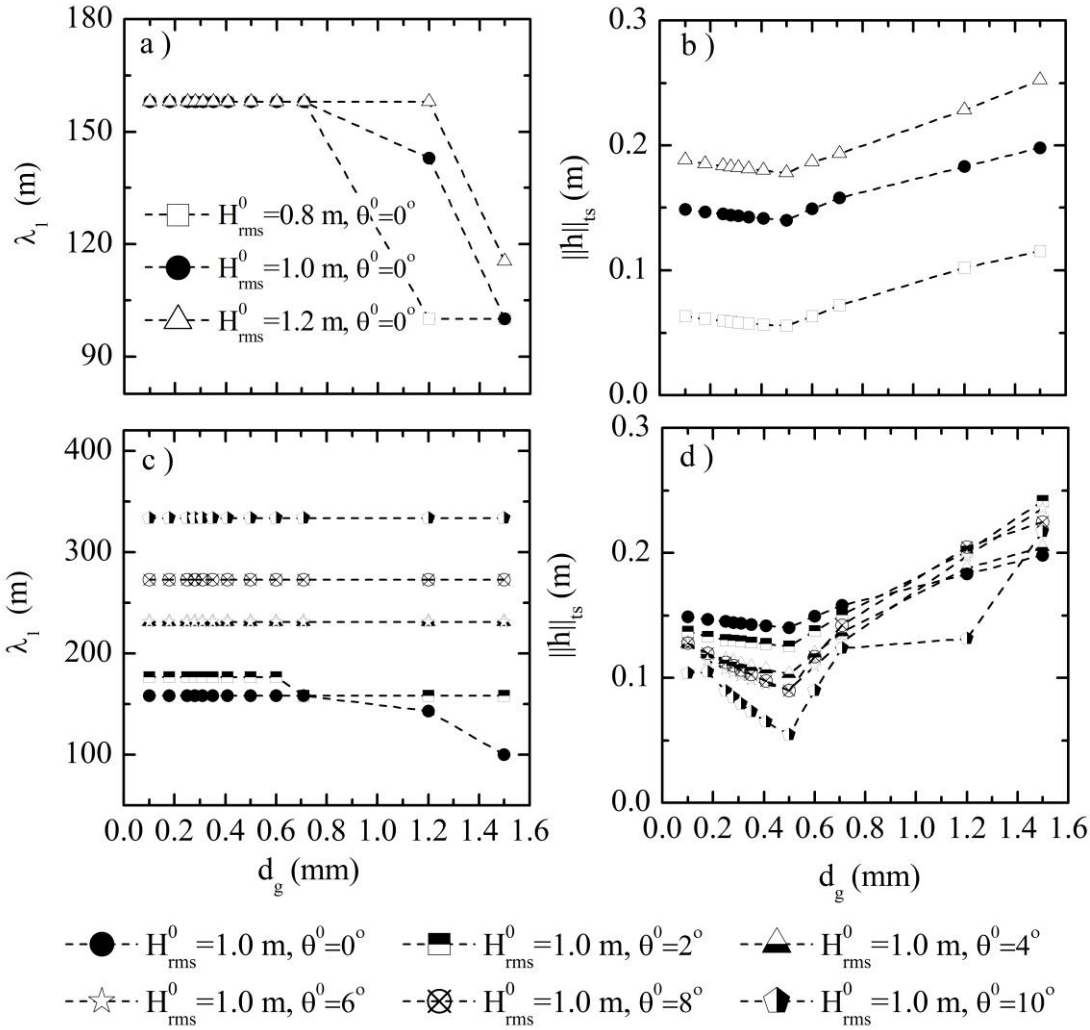

Figure 5.6 Sensitivity of rip channel geometrical characteristics to sediment grain size and offshore waves (up: wave height, down: wave angle). The filled circles in left and right panels represent the same simulations, i.e., $H^0_{rms} = 1\,m$ and $\theta^0 = 0^o$.

The variations of rip channel geometrical properties, including the initial predominant spacing λ_1 and rip channel three-dimensionality $\| h \|_{ts}$, for all 96 simulations are given in Figure 5.6. As shown in Figure 5.6a and Figure 5.6c, sediment grain size hardly affects the initial predominant wavelength λ_1. For most simulations presented here, λ_1 is kept the same when varying the sediment grain size. For the effect of wave conditions, we find wave height has only a limited influence on the predominant wavelength λ_1, while λ_1 increases significantly with increasing wave angle. For instance, the predominant wavelength λ_1 for $\theta^0 = 10^o$ is nearly double of that for $\theta^0 = 0^o$

Figure 5.6b and Figure 5.6d show the variation trends of $\| h \|_{ts}$. When increasing the sediment grain size, $\| h \|_{ts}$ decreases first and then increases for both normal and oblique waves. The transition of decrease and increase occur at sediment grain size around $d_g = 0.5\, mm$. Not surprisingly, wave height has a significant influence on $\| h \|_{ts}$ (Figure 5.6b), which increases significantly as H^0_{rms} increase. This is consistent with results obtained by Garnier et al. (2008). Moreover, $\| h \|_{ts}$ roughly decreases when wave obliquity increases (Figure 5.6d).

5.3.3 Sediment size effect on rip channel dynamical characteristics

Growth rate

By inserting the sediment transport expression into the sediment conservation equation, we can obtain that:

$$(1-p)\frac{\partial z_b}{\partial t} + \nabla \bullet (\alpha \vec{v}) - \nabla \bullet (\Gamma \nabla h) = 0, \tag{5.1}$$

in which $\Gamma = \alpha \gamma u_{rms}$ is the bed diffusive coefficient. In Equation (5.1), the term $\partial z_b / \partial t = \partial (z_0 + h) / \partial t = \partial h / \partial t$ as z_0 is constant over time. Using this relationship, Equation (5.1) can be rephrased as:

$$(1-p)\frac{\partial h}{\partial t}+D\vec{v}\nabla C-C\frac{\partial D}{\partial t}-\nabla\bullet(\Gamma\nabla h)=0, \tag{5.2}$$

where $C=\alpha/D$ is the depth-averaged concentration. Considering that the flow is quasi-steady and C is usually on order of 0.001, thus Equation (5.2) can be simplified as:

$$(1-p)\frac{\partial h}{\partial t}=-D\vec{v}\nabla C+\nabla\bullet(\Gamma\nabla h). \tag{5.3}$$

Equation (5.3) is called Bottom Evolution Equation (BEE) and is first derived by Falqués et al. (2000).

Garnier et al. (2006) established an effective way to understand the morphodynamic evolution of bedform as so called "global analysis" method, which is based on the BEE. This method takes the variables over the whole modelling domain into account and is carried out by applying two main manipulations, i.e., an overbar notation and calculation of L_2 norm, on the BEE. Specifically, the overbar notation reads, for any function $f=f(x,y)$,

$$\overline{f}=\frac{1}{L_xL_y}\int_0^{L_x}\int_0^{L_y}f\ dxdy. \tag{5.4}$$

The L_2 norm of function f is defined as:

$$\|f\|=\left(\overline{f^2}\right)^{1/2}. \tag{5.5}$$

Applying these two manipulations on the BEE, Garnier et al. (2006) obtained that the instantaneous growth rate of bedforms can be approximated as:

$$\Omega=\frac{P-\Delta}{\|h\|^2}, \tag{5.6}$$

in which $P=-\frac{1}{(1-p)}\overline{hD\vec{v}\nabla C}$ is the production term and $\Delta=-\frac{1}{(1-p)}\overline{h\nabla(\Gamma\nabla h)}$ is the damping term.

Here, the "global analysis" proposed by Garnier et al. (2006) is used to analysis the growth rate. First, the feasibility of this method is studied. From Figure 5.7, we can see that the initial growth rate Ω_1 is approximately same as the instantaneous grow rate at $t = t_r$ calculated using the global analysis method. This confirms that the global analysis method is appropriate for the analysis of initial growth rate here. Furthermore, it also suggests that the factors affect the instantaneous grow rate at $t = t_r$ should be same as the factors that affect the initial growth rate Ω_1.

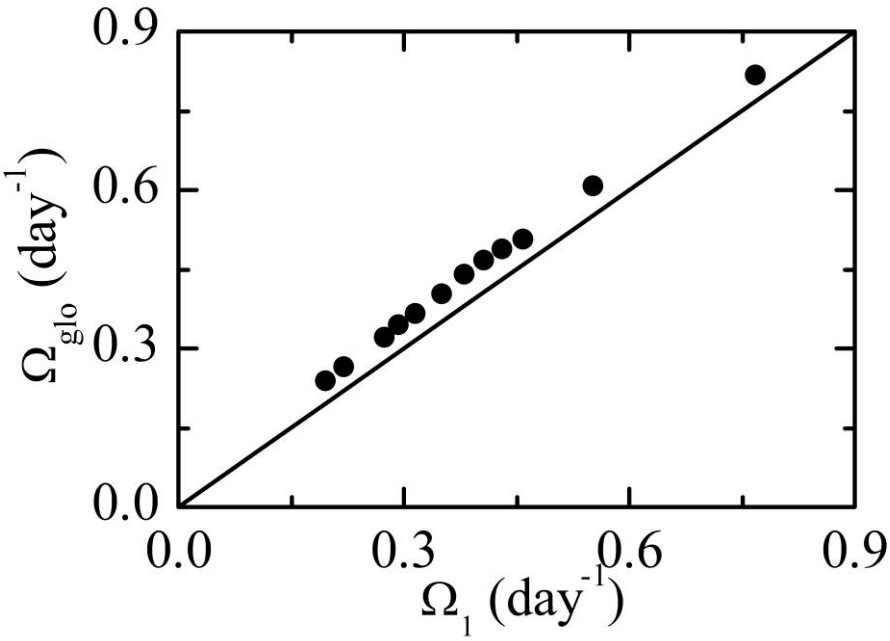

Figure 5.7 Comparison of initial growth rate Ω_1 and the growth rate Ω_{glo} that calculated using global analysis method for $H^0_{rms} = 1.0\,m$ and $\theta^0 = 0^o$.

For the instantaneous growth rate at $t = t_r$, we assume that the variables involved in Equation (5.6) can be spitted into a basic state quantity ($\overrightarrow{v_0}$ and C_0) plus a perturbation term($\vec{v}'$ and C'). Considering the rip channel three-dimensionality at $t = t_r$ is not large (see, e.g., Figure 5.1b), it is reasonable to expect that the magnitude of the perturbation term is small compared to those of the basic state. Thus, the production term in Equation (5.6) can be linearized into:

$$P = -\frac{1}{(1-p)}\frac{\overline{hDu'\frac{\partial C_0}{\partial x}}}{\|h\|^2} - \frac{1}{(1-p)}\frac{\overline{hDv_0\frac{\partial C'}{\partial y}}}{\|h\|^2}, \tag{5.7}$$

The first and second term on the right hand side of Equation (5.7) are the cross-shore and longshore components of the unitary production term $P/\|h\|^2$, which are denoted as $P_x/\|h\|^2$ and $P_y/\|h\|^2$ respectively. In our simulations here the cross-shore component of unitary production term $P_x/\|h\|^2$ is responsible for over 95% of the total unitary production term $P/\|h\|^2$ and $P_y/\|h\|^2$ has only a negligible contribution (e.g., see Figure 5.8a).

From Equation (5.6), we can see that the growth rate depends on a number of factors such as the sediment concentration and its gradient, current speed, water depth. For simulations that varying sediment size, the sediment concentration and its gradient will be directly influenced (denoted as the direct influence of sediment size), which can cause an influence on the growth rate. This change may, however, subsequently result in the response of seabed are different for simulations with different sediment size, which means a different seabed bathymetry at time $t = t_r$. Such changes will potentially generate difference in terms like current speed, water depth, which can pose as another group of factors lead to the change in growth rate, denoted as indirect influence of sediment size. In below, we will determine which one is the key factor that controls the growth rate variation for varying the sediment size in our simulations. To do so, two series of extra simulations (hydrodynamic) with respect to that presented in Figure 5.8a have been carried out. In the first series of simulations, we kept the sediment size the same ($d_g = 0.25\,mm$), thus the direct influence of sediment grain size is excluded. In the second series of simulations, we kept seabed bathymetry the same, which is extracted from the simulation presented in Figure 5.8a with $d_g = 0.25\,mm$ at $t = t_r$, denoted as $z_b(t = t_r, d_g = 0.25)$. By doing so, the indirect influence of sediment grain size is excluded.

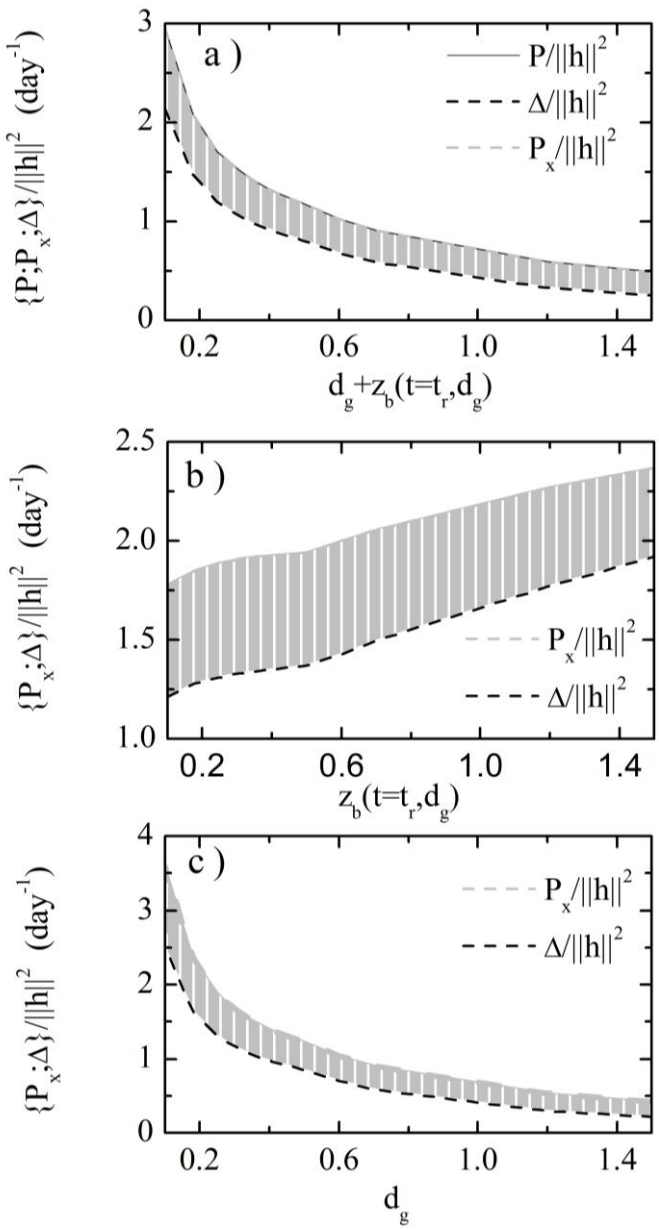

Figure 5.8 Global analysis of growth rate for $H^0_{rms} = 1.0\,m$ and $\theta^0 = 0^o$. $\Delta / \| h \|^2$, $P / \| h \|^2$ and $P_x / \| h \|^2$ computed as a function of (a) both sediment grain size and bathymetry, (b) only bathymetry and (c) only sediment grain size. Note that the x-axis for all plots indicates the value for variable d_g.

The results of instantaneous growth rate calculated by the "global analysis" method for these two series of simulations are presented in Figure 5.8b and Figure 5.8c respectively. By comparing Figure 5.8b and Figure 5.8c with Figure 5.8a (both

influences are included), we can see that the variation trends and magnitudes of $P_x / \| h \|^2$ and $\Delta / \| h \|^2$ are similar in Figure 5.8a and Figure 5.8c, but both of them are different to Figure 5.8b. Thus, we can conclude that the direct influence related to the change of sediment and its concentration gradient caused by sediment grain size is the main reason for the variation of growth rates in simulations that varying grain size.

Subsequently, we set out to find a quantitative relationship between wave condition (wave angle) and initial growth rate Ω_1, which provides as a base to encapsulate the effect of sediment grain size. For simulations presented here, the cross-shore component of production term dominates over the longshore component as shown in Figure 5.8a. This situation is the same as the results presented by Garnier et al. (2013). By analyzing the relationships between currents and seabed and the variation of production and damping terms for varying wave angle, Garnier et al. (2013) pointed out that the inhibition of the rip channel formation, i.e., decrease of growth rate, is mainly because of the decay of the rip intensity and the decreasing correlation between the cross-shore current and the seabed bathymetry caused by the shift of rip current. For small angles, both rip current intensity and shift distance are roughly proportional to the offshore wave angle. This implied that growth rate decreases nearly proportional to wave angles. Moreover, we find that a critical wave angle exists in our simulations as when offshore wave angle is larger than $\theta_{crit} = 11^o$, the growth rate is almost equal to zero for all sediment sizes, especially for coarse sediments. Considering these findings, we tried to relate the growth rate as a function of offshore wave angle. We found that growth rate is well related to the indicator $1 - \theta / \theta_{crit}$ (Figure 5.9a). When wave angle increases, the indicator $1 - \theta / \theta_{crit}$ decreases and correspondingly the predicted growth rate decreases, showing the same variation trend as that presented in Figure 5.3d.

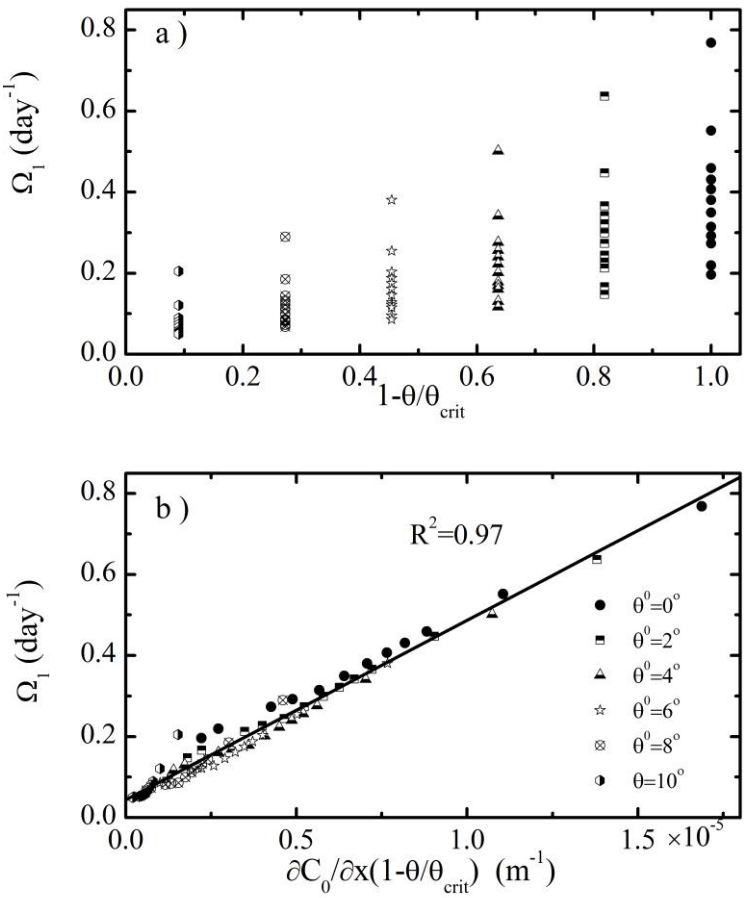

Figure 5.9 Initial growth rate versus (a) $1-\theta/\theta_{crit}$ and (b) $\partial C_0/\partial x(1-\theta/\theta_{crit})$.

Until now, the grain size effect on the growth rate has still not yet been encapsulated. Thus large scatter exists inside the results with the same wave angle but different sediment grain size (Figure 5.9a). According to the results of global analysis that the main influence of varying sediment grain size on the growth rate seems to be through changing the sediment concentration and its gradient (see Figure 5.8). Based on Equation (5.6) and Equation(5.7), we decided to relate grain size with growth rate using the cross-shore gradient of sediment concentration, as it contributes mostly to the production term when varying the sediment size, i.e., the term that responsible for the growth of rip channels. Figure 5.9b shows that the indicator $\partial C_0/\partial x(1-\theta/\theta_{crit})$, which is the product of local gradient of sediment concentration on the bar crest at the basic state and the indicator $1-\theta/\theta_{crit}$, is perfectly correlated

with the growth rate for all simulations and can well encapsulates effects of both sediment grain size and offshore wave obliquity.

Response time

Figure 5.10 displays the response time as a function of initial growth rate. It can be inferred from this figure that the variation of response time and initial growth rate is possibly not independent. Generally, the larger is the initial growth rate, the shorter the response time. This suggests the growth rate evolution curve that has a higher peak would generally appear to be narrower and vice versa.

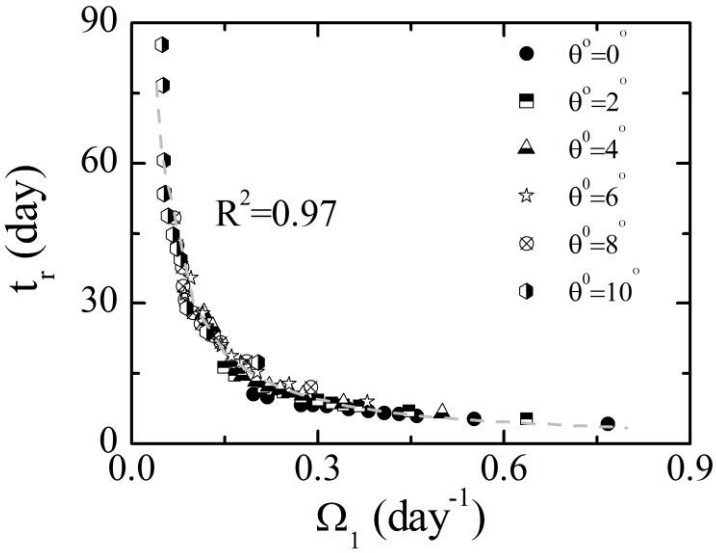

Figure 5.10 Initial growth rate versus response time for simulations with $H^0_{rms} = 1.0\,m$.

Subsequently, we tried to link the response time to sandbar geometry properties, hydrodynamic condition, sediment concentration on the bar crest, using the predictor suggested by Smit et al.(2008), i.e., the ratio of the alongshore sediment transport rate on the bar crest to the active volume of sandbar Vol_a.

Using the transportation formulation of Bailard (1981), Smit et al.(2008) deduced that the alongshore sediment transport rate can be approximate as:

$$q_y = C_1 u_{rms}^2 v_y, \tag{5.8}$$

where C_1 is a dimensional scaling coefficient and is commonly related to the sediment size, v_y is the alongshore current speed on the bar crest at the basic state. Using linear wave theory and assuming shallow water waves, the root-mean square wave orbital velocity $u_{rms} = H_{rms}(g/D)^{1/2}$. Based on this relationship and saturated surf zone hypothesis ($H_{rms} = \gamma_b D$), Smit et al. (2008) simplified the ratio of the alongshore sediment transport rate on the bar crest to the active volume of sandbar Vol_a into $C_1 g \gamma_b H_{rms}^0 v_y / Vol_a$.

When keeping the offshore wave height and period the same as simulations that presented in Figure 5.11, the active volume is nearly the same. Thus in this situation the indicator $C_1 g \gamma_b H_{rms}^0 v_y / Vol_a$ can be further simplified to $C_1 v_y$. In the simulations presented in Smit et al. (2008) , the sediment size is not changed. Thus, the indicator can be further simplified into v_y. Figure 5.11a shows that the response time increase when the alongshore velocity on the bar crest increases for simulations with $H_{rms}^0 = 1.0\,m$, which is consistent with that suggested by Smit et al.(2008). However, possibly because the sediment size is changed in our simulations, the response time exhibits a large spread for the simulations under same wave obliquity but with different grain size. In order to reduce this spreading, we restored the simplified predictor into its original form, i.e., the ratio of alongshore sediment transport rate on the bar crest to the active volume of sandbar. This indicator is now based on the simulation output directly and calculated as $DC_0 v_y / Vol_a$, in which the influence of grain size is taken into account (i.e., via sediment concentration). Surprisingly, the scatter existed in Figure 5.11a does not disappear. Moreover, the response time tends to decrease when the ratio of sediment transport to the active volume of sandbar increases (Figure 5.11b). This trend is opposite to that suggested by Smit et al.(2008). The point will be discussed in later.

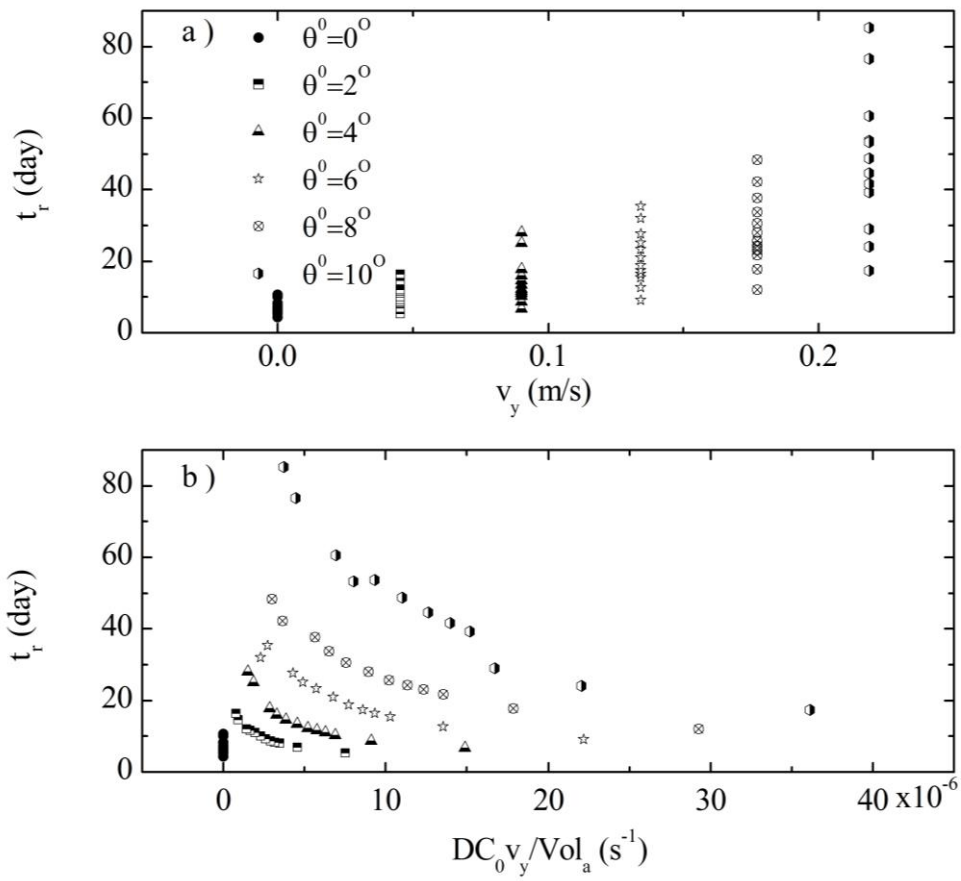

Figure 5.11 Response time versus (a) alongshore current speed on the bar crest and (b) sediment transport rate divided by the active volume of sandbar for $H_{rms}^{0} = 1.0\,m$.

Migration speed

Extending the "global analysis" technique of Garnier et al.(2006), Vis-Star et al.(2008) introduced a method to calculate the instantaneous migration speed of rip channels as:

$$(1-p)\,c_m = \frac{\overline{\dfrac{\partial z_b}{\partial y}\nabla q_s}}{\left\| \dfrac{\partial z_b}{\partial y} \right\|^2}. \tag{5.9}$$

We find that the instantaneous migration speed obtained from equation (5.9) is similar to the mean migration speed calculated by measuring the distance of rip channels migrate alongshore in a specific time length. Based on this, it is reasonable to say that the global analysis method is suitable here to examine the main factor that influences the migration speed of rip channels for varying sediment size.

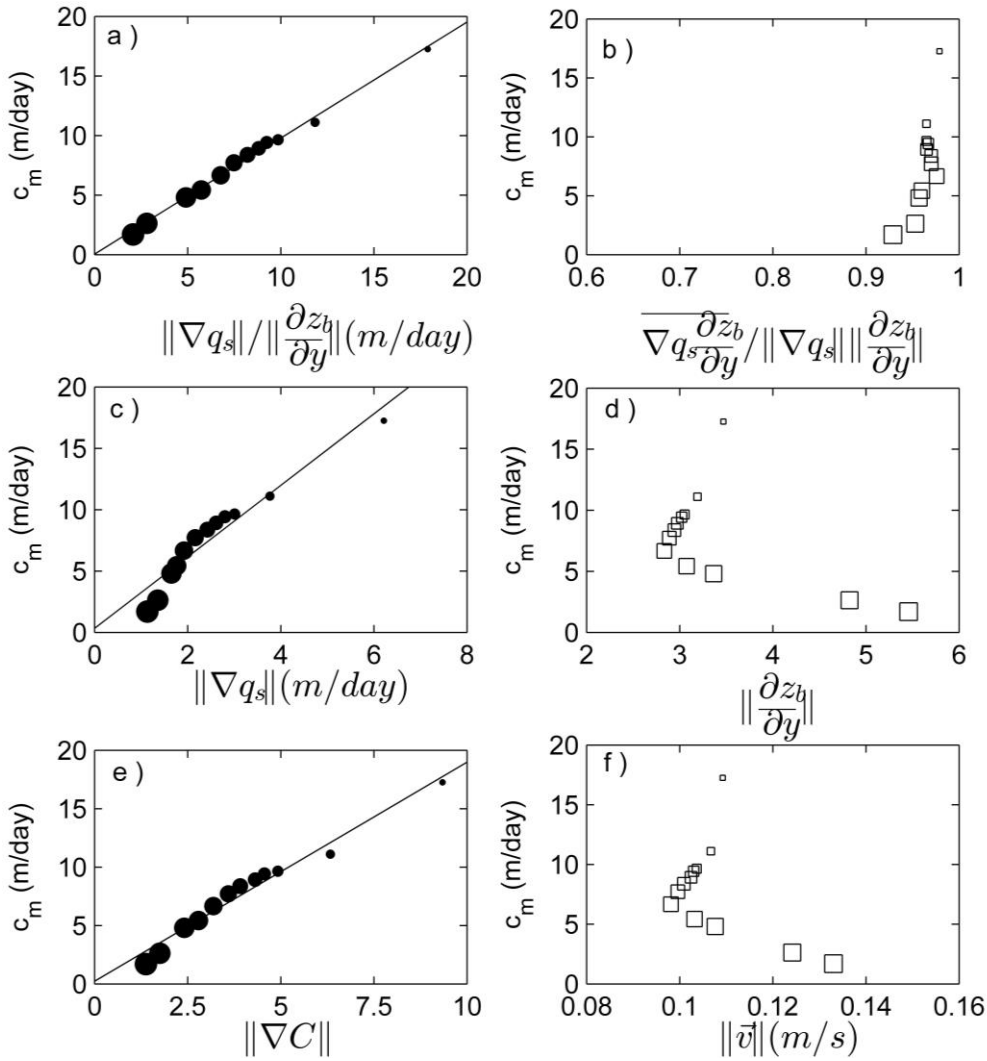

Figure 5.12 Global analysis of migration speed for $H_{rms}^0 = 1.0\,m$ and $\theta^0 = 6^\circ$. Migration speed as a function of (a) $\|\nabla q_s\| / \|\partial z_b / \partial y\|$, (b) $\overline{\nabla q_s \cdot (\partial z_b / \partial y)} / \|\nabla q_s\| / \|\partial z_b / \partial y\|$, (c) $\|\nabla q_s\|$, (d) $\|\partial z_b / \partial y\|$, (e) $\|\nabla C\|$ and (f) $\|\vec{v}\|$.

Similar to the growth rate, both direct and indirect influence by changing sediment size exist for the rip channel migration speed. Therefore, the contribution of these two aspects will be investigated in the following. To be concise, the simulations with $H_{rms}^{0} = 1.0\,m$ and $\theta^{0} = 6^{o}$ are taken as example to illustrate this analysis. Figure 5.12 gives the variations of different terms that are potentially responsible for the migration speed in simulations with the incident wave condition is $H_{rms}^{0} = 1.0\,m$ and $\theta^{0} = 6^{o}$. According to equation(5.9), migration speed is determined by the ratio and the correlation between the gradient of sediment transport rate and the alongshore derivative of bed level (it should note that the bed porosity has been included in the sediment transport flux to simplify the notation), i.e., $\|\nabla q_s\| / \|\partial z_b / \partial y\|$ and $\overline{\nabla q_s \cdot (\partial z_b / \partial y)} / \|\nabla q_s\| / \|\partial z_b / \partial y\|$. As shown in Figure 5.12b, the term $\overline{\nabla q_s \cdot (\partial z_b / \partial y)} / \|\nabla q_s\| / \|\partial z_b / \partial y\|$ is almost unchanged when varying the grain size, which stays between 0.9 and 1.0 with a mean value of 0.96. In contrast, $\|\nabla q_s\| / \|\partial z_b / \partial y\|$ increases significantly when grain size decreases. Furthermore, this term correlated well with the migration speed ($R^2 = 0.99$). This suggests the term $\|\nabla q_s\| / \|\partial z_b / \partial y\|$ controls the variation of migration speed (Figure 5.12a). Similarly, we further separate the ratio of the gradient of sediment transport rate to the alongshore derivative of bed into $\|\nabla q_s\|$ and $\|\partial z_b / \partial y\|$. As can be seen from Figure 5.12d, $\|\partial z_b / \partial y\|$ decreases first and then increases again when grain size increases. Obviously, this trend is not consistent with that of migration speed. Thus, subsequent analysis is focused on the term $\|\nabla q_s\|$, which is further divided into $\|\vec{v}\|$ and $\|\nabla C\|$. Considering the variation of $\|\vec{v}\|$ is similar to that of $\|\partial z_b / \partial y\|$ (thus not same as migration speed) and migration speed is significantly correlated with $\|\nabla C\|$ (Figure 5.12e), we can conclude that the variation of migration speed when varying grain size is most likely because of the change of stirred sediment concentration, which decreases (increases) for coarser (finer) sediments.

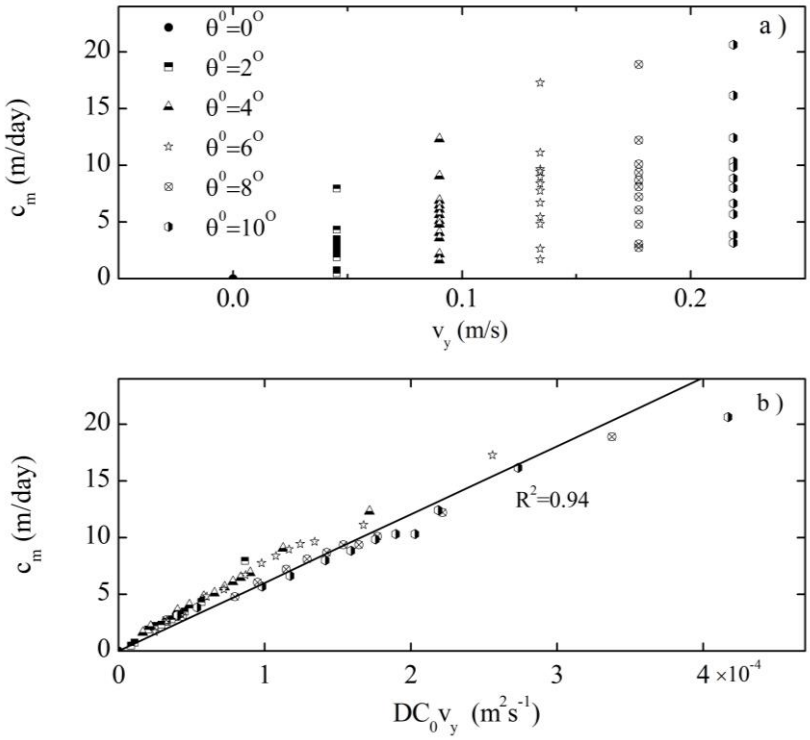

Figure 5.13 Migration speeds versus (a) alongshore current velocity and (b) alongshore sediment transport rate on the bar crest for $H_{rms}^{0} = 1.0\,m$.

Similar to the growth rate, we then try to relate the migration speed to local hydrodynamic condition and sediment concentration on the bar crest at the basic state. Firstly, we attempt to relate the migration speed with longshore current velocity on the bar crest, as according to Ruessink et al.(2004) the longshore current is the driving force behind the migration of rip channel. The result is presented in Figure 5.13a, in which we can see the migration speed broadly increase with longshore current velocity on the bar crest. However, relationship including only the alongshore current velocity is not enough to reflect variation of migration speed due to the change of sediment grain size. In the following, we test the assumption that the grain size affects the migration speed through the sediment transport rate, which decreases as sediment grain size increases. This assumption is inspired by the recent study of Orzech et al.(2013), who found the predicted sediment transport rate is strongly correlated with the measured migration speed. As can be seen from Figure 5.13b, the migration speeds for all simulations follow similar trend and are strongly

correlate with the alongshore sediment transport rate, in which the influence of sediment concentration is taken into account. This illustrates the importance of sediment grain size on the migration speed of rip channels.

5.3.4 Sediment size effects on rip channel geometrical characteristics

Rip channel three-dimensionality

Based on Equation (4.7) and the definition of saturation time, rip channel three-dimensionality at the saturation time $\| h \|_{ts}$ as that displayed in Figure 5.6b and Figure 5.6d can be calculated as:

$$\| h \|_{ts} = \| h \|_0 \, (\Pi_{t=0}^{t=t_s} (1 + 2\Omega_t))^{0.5}, \tag{5.10}$$

where Π represents the multiple multiplication. Intuitively, one may expect that a larger growth rate corresponds to a larger rip channel three dimensionality at the saturation state, but our results show that this is not necessary right. As actually, $\| h \|_{ts}$ is not only dependent on the growth rate but also the saturation time, which can be deduced from Equation (5.10). Both increase of growth rate and saturation time can potentially cause $\| h \|_{ts}$ to increase and vice versa. Unfortunately, the variation trends of growth rate and saturation time is opposite to each other (Figure 5.14) and thus a competition exists between these two effects. Notice that it is the first time that the importance of the saturation time on rip channel threes-dimensionality has been identified. An interesting example to demonstrate this effect is the case of increasing sediment size from 0.5 mm to 0.71 mm which leads $\| h \|_{ts}$ to increase with the corresponding growth rate decreases (see Figure 5.1b). Figure 5.6b and Figure 5.6d show that there is an observed minimum value in $\| h \|_{ts}$ at sediment size $d_g = 0.5\, mm$. In fact, $\| h \|_{ts}$ attains this minimum value is unsurprising. As $\| h \|_{ts}$ depends on growth rate and saturation time, its value and the occurrence of minimum should depend on the variation trends of these two variables to sediment size. In fact the growth rate in our cases presented here is largely controlled by the

coefficient of sediment transport A_s which is a monotonously decreasing function of sediment size while saturation time are affected by both the coefficient of sediment transport A_s and the critical current velocity of motion u_{cr}, the latter of which has a minimum at $d_g = 0.5\,mm$.

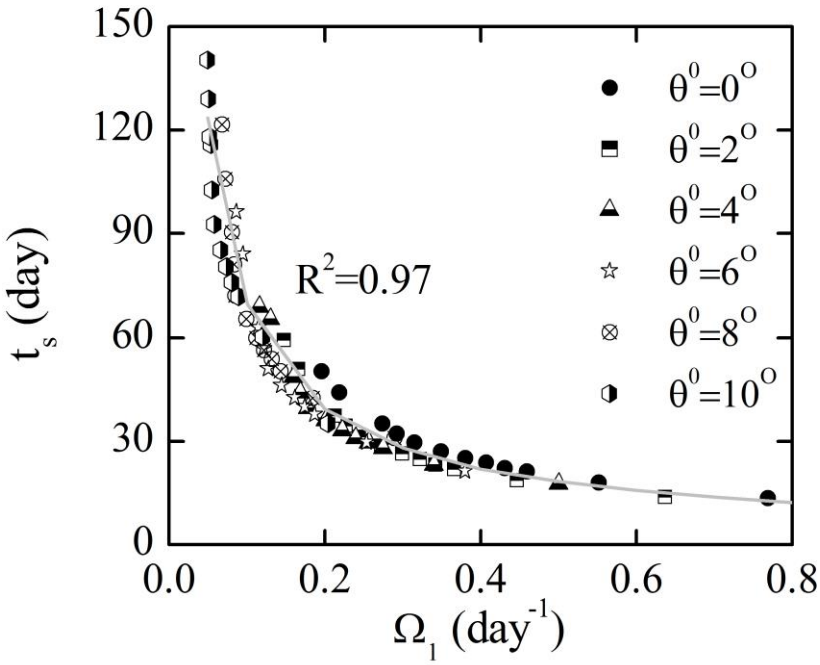

Figure 5.14 Initial growth rate versus saturation time for simulations with $H^0_{rms} = 1.0\,m$.

5.4 Discussion

we have explored the predictor proposed by Smit et al.(2008) for determining the response time of rip channels, as in this predictor, the effect of sediment size can be implicitly accounted for through its influence on the transport rate. However, we found this predictor is unable to explain the variation trends of the response time for the range of sediment grain size considered. Further research is needed to elucidate the relationship between the response time and sediment size. Although not yet proposed such a predictor, some inspiration can be derived from the present study,

i.e., it may be productive is to explore the relationship between the response time and growth rate, as we found these two parameters are somewhat related. Comparing to the response time, the variation of growth rate can be analysed on a more physically sound basis by using the global analysis method.

The response time was found in some earlier studies to have some correlations with rip channel spacing, i.e., the response time is longer for rip channel with a wider spacing (van Enckevort et al., 2004), but the present results show no such relationship between these two indicators. For instance, for increasing response time, the wavelength of rip channels can either stay nearly the same (for varying sediment grain size) or increase significantly (for varying wave angle). This lack of correlation between these two indicators can also been implicitly deduced from the results of simulations that vary the seabed bathymetries as reported by Calvete et al. (2007). In this study, Calvete et al. (2007) found that the predominant wavelength of rip channels is not determinedly dependent on the growth rate (note that the growth rate is somehow related with the response time).

With the help of global analysis method, a relationship that correlates the growth rate with the wave conditions and sediment grain size has been established. As in the present simulations the formation of rip channels are mostly dependent on the "bed-surf" mechanisms (Falqués et al., 2000), while in other conditions the "bed-flow" mechanisms may dominant the rip channel formations (Thiébot et al., 2012). Therefore, further efforts need to make in order to develop a relationship that is capable of incorporating both mechanisms still needs to be developed.

5.5 Summary

In this chapter, the influence of sediment grain size on the dynamical evolution and geometrical properties of rip channels on beach with uniform sediment are investigated. We find that the grain size can affect a number of aspects of rip channel dynamics. With increasing grain size, both longshore migration speed and growth rate decrease significantly, while the response and saturation times increase. On the

other hand, the influence of grain size on the geometrical properties of the rip channel seems to be much less pronounced, as the wavelength of the channels hardly changes and the three-dimensionality features only vary slightly. The “global analysis” method is applied to investigate the mechanism underlying the variations of growth rate and migration speed for varying sediment size. The calculations reveal that these variations are mainly caused by the amount of sea bed sediments being stirred up which is clearly grain-size-dependent.

Chapter 6

The grain size effects on rip channel dynamics for beach with non-uniform sediment

6.1 Introduction

So far, all numerical simulations that aim to investigate the self-organization behaviour of rip channels crudely assume the grain size on the studied beach is uniform and constant, which is apparently contradicted with many field studies. Simplification of a real beach with such complex variations in grain size over both temporal and spatial scales into a beach that with statistically equal mean grain size is problematic. This is because such reduction implicitly assumes the actual dynamics of rip channels are either similar to those within an environment comprised of uniform sediments or equivalent to the linear summation of results determined for individual grains with an overall distribution, validity of which is lack of evidence.

In the present chapter, we aim to demonstrate that the coastal sediment heterogeneity is critical to the evolution of individual alongshore non-uniform sandbar features and also the coupling behaviour among different morphological patterns on beach. We performed systematic simulations with both uniform and non-uniform sediments on an idealized barred beach using the modified Xbeach model, in which a module that solves the sedimentation and erosion of multiple sediment size is incorporated.

This chapter is organized as follow: in Section 6.2, the module for solving the sedimentation and erosion for multigrain seabed is introduced. In Section 6.3, the configurations of numerical experiments are illustrated. In Section 6.4 the main results of numerical simulations are presented, where a detail comparison and a comprehensive analysis of predicted dynamics of rip channels for uniform and non-uniform beach is conducted. In Section 6.5, the results of simulations present here

are compared with previous observations. In the final Section, the summary for this chapter are drawn.

6.2 Multigrain sedimentation/erosion module

To study the morphodynamic evolution of beaches with non-uniform sediments, a module that solves the sedimentation and erosion of multigrain seabed has been incorporated. The framework of this module is adapted from that proposed by Hirano (1971), who was the first to developed the morphodynamic model for non-uniform sediment and proposed the active layer concept. This framework proposed by Hirano (1971) and its variants have been widely used in the study of morphodynamics for seabed with non-uniform sediments (Roos et al., 2007; van der Wegen et al., 2011; Vis-Star et al., 2009).

Following the framework proposed by Hirano (1971), the seabed is discretized into N_l numerical layers (substrates), with the thickness of each layer is $D_z(i)$. These numerical layers are stacked atop each other and are allocated between seabed and a specified base with its elevation at z_{c0}. Thus, the seabed level can be calculated as:

$$z_b = z_{c0} + \sum_{i=1}^{n_l} D_z(i). \tag{6.1}$$

In each layer, it consists of N_g different sediment classes. For each sediment class, we note down its grain size $d_g(i, j)$, sediment mass $m_g(i, j)$ and therefore the associated fraction $p_g(i, j)$ calculated as:

$$p_g(i, j) = \frac{m_g(i, j)}{\sum_{j=1}^{N_g} m_g(i, j)}. \tag{6.2}$$

Given these properties, we can calculate the mean grain size $\overline{d_g}(i)$ of each layer:

$$\overline{d_g}(i) = \sum_{j=1}^{N_g} d_g(i, j) p_g(i, j). \tag{6.3}$$

The total sediment transport rate for non-uniform sediments is calculated independently for each fraction without considering the interaction between different sediment classes, e.g., hiding/exposure effect. For each sediment class, we compute the depth-integrated saturated sediment concentration $C^*(j)$ according to Equation (3.26). However, the actual concentration may "starve" due to the fraction availability reduced in mixed sediment. The actual depth-integrated sediment concentration of each sediment class $C(j)$ is calculated as:

$$C(j) = p_g(1, j) C^*(j), \tag{6.4}$$

where $p_g(1, j)$ is the percentage of sediment class j in the active layer (the layer assigned on the top of substrates stack). Then, we compute the sediment transport rate for each fraction $\overrightarrow{\mathbf{q}_\mathbf{j}}$ based on Equation (3.32) and Equation (3.33), which is inserted into Equation (3.15) to calculate the bottom level changes for each sediment class Δz_j.

Figure 6.1 indicates that the numerical layers can be divided into active layer, transition layer, variable layer and underlying layer. In present work, the thickness is constant for all layers, except the variable layer (the k_v-*th* layer), which located at a certain depth beneath the active layer. The layers locate between the active layer and variable layer are named as the transition layers. The thickness of variable layer decreases (increases) in the case that the seabed erosion (deposition) takes place. The layers below the variable layer are passive with their properties not changed. In addition, Figure 6.1 also schematically illustrates what happens to the substrates when the bed evolves. Except the variable layer, the thicknesses of other layers do not change. However, the fractional compositions of layers can evolve including that of active layer, transition layer and variable layer. Together with the seabed evolution, the transition layers and the active layer move simultaneously with the seabed level: upward in the case of deposition and downward in the case of erosion.

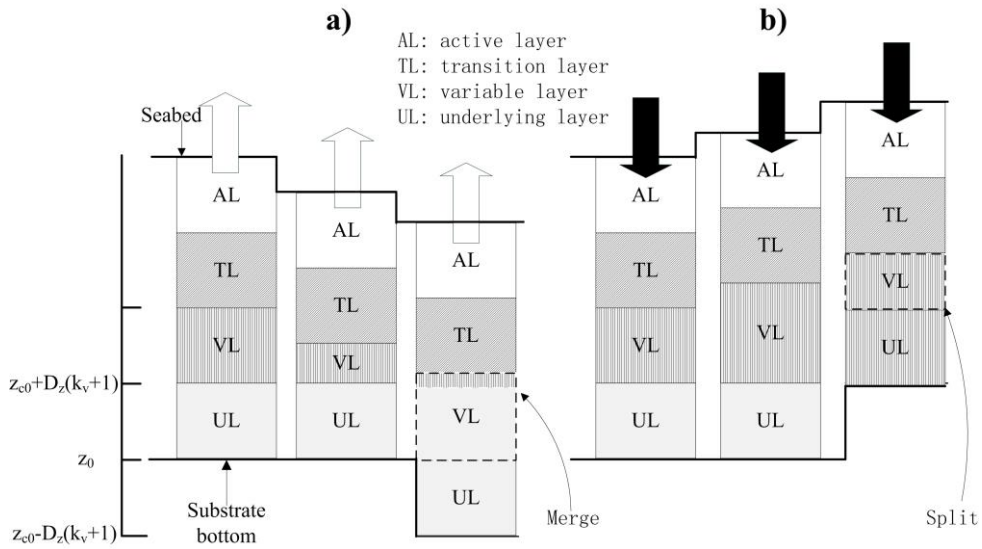

Figure 6.1 Schematic representation of the vertical stacked substrate layers and the evolution of bed layers. The white arrows in (a) indicate erosion and the black arrows in (b) indicate the deposition.

This vertical movement cause a sediment exchange flux with advection velocity equal to the bed level change and consequently may cause changes in the sediment fraction. The fractional composition of sediment classes are updated based on the mass balance. In the case of deposition, it calculated as:

$$
\begin{aligned}
&Active\ layer: p_g^{t+1}(1,j) = \frac{\Delta z_j}{D_z(1)} + \frac{D_z(1)-\Delta z}{D_z(1)} p_g^t(1,j) \\
&Transition\ layer: p_g^{t+1}(i,j) = \frac{D_z(i)-\Delta z}{D_z(i)} p_g^t(i,j) + \frac{\Delta z}{D_z(i)} p_g^t(i-1,j) \\
&Varible\ layer: p_g^{t+1}(k_v,j) = \frac{D_z^t(k_v)p_g^t(k_v,j)+\Delta z p_g^t(k_v-1,j)}{D_z^t(k_v)+\Delta z},
\end{aligned}
\tag{6.5}
$$

In the case of erosion, it reads:

$$
\begin{aligned}
&Active\ layer: p_g^{t+1}(1,j) = \frac{D_z(1)p_g^t(1,j)+\Delta z_j}{D_z(1)} - \frac{\Delta z}{D_z(1)} p_g^t(2,j) \\
&Transition\ layer: p_g^{t+1}(i,j) = \frac{D_z(i)+\Delta z}{D_z(i)} p_g^t(i,j) - \frac{\Delta z}{D_z(i)} p_g^t(i+1,j) \\
&Varible\ layer: p_g^{t+1}(k_v,j) = p_g^t(k_v,j).
\end{aligned}
\tag{6.6}
$$

Simultaneously, the thickness of the variable layer is updated at each time step:

$$D_z^{t+1}(k_v) = D_z^t(k_v) + \Delta z. \tag{6.7}$$

Note that the variable layer is allowed to split or merged in order to avoid its thickness being too thin or too thick. Once the thickness is smaller than the critical value, Δz_{merg} , the variable layer then merged with its lower neighbour layer. Simultaneously, the bottom of substrates moves down to $z_{c0} = z_{c0} - D_z(k_v + 1)$ by adding a new substrate beneath the old substrate bottom in order to keep the number of substrates constant. Similarly, the variable layer splits into two layers once the critical thickness Δz_{split} is exceeded. At the same time, the substrates bottom shifts upwards to $z_{c0} = z_{c0} + D_z(k_v + 1)$.

6.3 Simulations set-up

The cross-shore geometrical properties of initial alongshore uniform bathymetry is similar as that used in Chapter 4 and Chapter 5, which, as mentioned before, is idealized but representative of the barred beach that observed at Duck, North Carolina (Yu and Slinn, 2003). However, the modelling domain is reduced to $L_x = 240\,m$ and $L_y = 450\,m$, with the origin moved 10 m shoreward. The reason of reducing the modelling domain is to reduce the computation time, as the module for modelling the morphodynamics of seabed with non-uniform sediment needs large amount of computation. The grid size is much smaller comparing to that used in the previous two chapters, with $\Delta x = 3\,m$ and $\Delta y = 1.5\,m$. Decrease the grid size is because we want to well resolve the small morphological features near the shoreline, i.e., the wavelength of the transverse bar is usually around $O(10\,m)$. Since our focus here is to explore the role played by the sediment grain size and its distribution on the dynamical behaviour of rip channels on sand beach system, the wave conditions at the offshore boundary is set to be the same for all simulations, i.e., using waves with wave height $\mathrm{H}_{\mathrm{rms}}^{\mathbf{0}} = 1.2\,\mathrm{m}$, wave period $\mathrm{T} = 7.5\,\mathrm{s}$ and wave angle $\theta^{\mathbf{0}} = 0^{\circ}$.

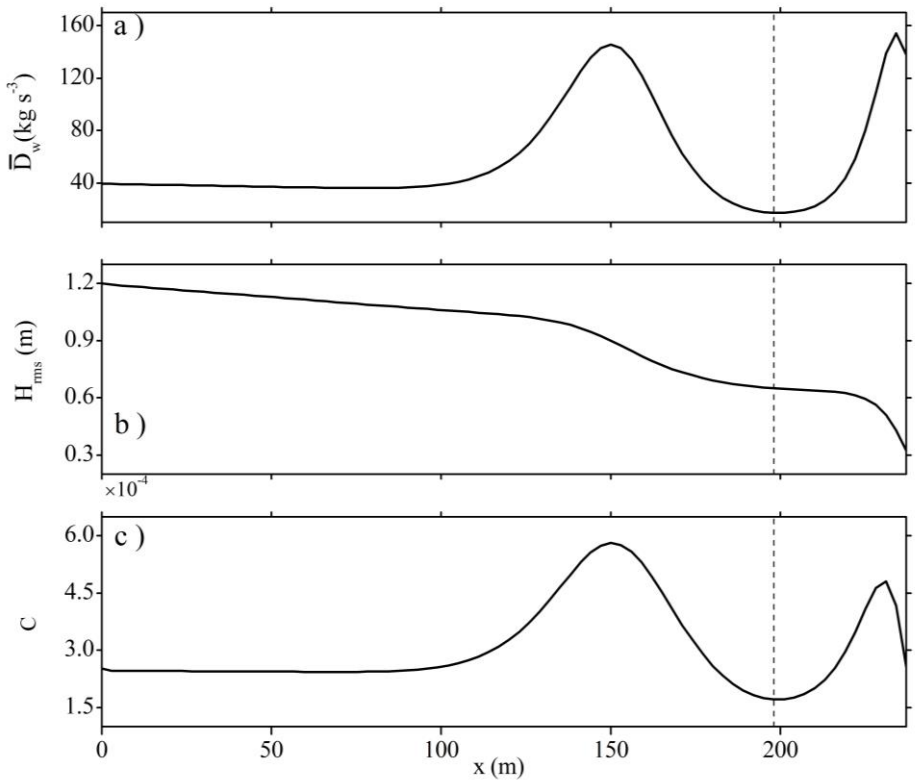

Figure 6.2 The cross-shore variation of (a) wave energy dissipation, (b) wave height and (c) depth-averaged sediment concentration on the initial alongshore uniform bathymetry for simulation with uniform sediment (0.25 mm) with $H_{rms}^{0} = 1.2\ m$, $T = 7.5\,s$, $\theta^{0} = 0^{\circ}$. The dashed line is at $x = 195\,m$.

The cross-shore variation of wave energy dissipation, wave height, and depth averaged sediment concentration on the initial alongshore uniform bathymetry for the simulation using uniform sediment with its grain size equal to 0.25 mm is displayed in Figure 6.2. It can be clearly seen that the wave energy dissipates significantly around two locations (the formula of Thornton and Guza (1983) is used to calculate the wave energy dissipation), with one is near the sandbar crest (the cross-shore coordinate is about 150 m) and another is near the shoreline. Corresponding to these two locations, the wave height decreases remarkably and two peaks of depth-averaged sediment concentration appear. In fact, these two peaks of depth-averaged sediment concentration are ascribed to be the reason for the

formation of two kinds of rip channel systems (Garnier et al., 2008). Specifically, the peak near the sandbar crest is usually correlated to the formation of crescentic bars, while the one near the shoreline is often linked to the emergence of transverse bars. In the previous chapters, the transverse bars near the shoreline are not emerged from the initial alongshore patternless seabed, which is mainly because the damping effect due to downslope transport is too large.

In this chapter, the bed slope coefficient used near the shoreline is reduced to $\gamma = 2$ with the aim to make the transverse bar near the shoreline can emerge, as reduce the bed slope coefficient would result a decrease in the damping effect and promote the instability of seabed. It should be noted that the bed slope coefficient is still set to be $\gamma = 5$ in the area far offshore. The boundary between area that uses $\gamma = 5$ and area that uses $\gamma = 2$ is at $x = 195\,m$, which is nearly at the trough that locates between the two maxima of depth-averaged sediment concentration, as denoted by the dashed line in Figure 6.2.

Simulations using both uniform and non-uniform sediments are performed. In simulations using uniform sediments, single grain size is used. In this situation, eight simulations in total are carried out, with sediment grain sizes varying from 0.1 mm to 0.5 mm, i.e., [0.1 0.18 0.25 0.28 0.31 0.35 0.41 0.5] mm. In simulations using non-uniform sediments, two grain sizes are used. Specifically, the simulations using non-uniform sediment can be divided into two types. In first type, the mean sediment size of sediment (determined by the grain size and fractional composition of each sediment class, see Equation(6.3)) over the whole modelling domain is not changed, i.e., Case A1-A3. The mean grain size is set to be equal to 0.25 mm, while the grain size of individual sediment grain size is not the same among different simulations (see Table 6.1). In the second type, the mean sediment size is specified to vary in the

Table 6.1 The compositions of grain size for simulations using non-uniform sediments

Case number	Grain size of fine fraction (mm)	Grain size of coarse fraction (mm)	Fraction of finer sediment	Fraction of coarser sediment	Mean grain size over the modelling domain
A1	0.25	0.25	0.500	0.500	0.25
A2	0.18	0.28	0.300	0.700	0.25
A3	0.1	0.5	0.625	0.375	0.25
Case number	Grain size of fine fraction (mm)	Grain size of coarse fraction (mm)	Starting point of mean grain size decrease (m)	End point of mean grain size decrease (m)	Mean grain size over the modelling domain
B1	0.1	0.5	213	165	0.1796
B2	0.1	0.5	213	150	0.1876
B3	0.1	0.5	213	135	0.1956
B4	0.1	0.5	198	165	0.1956
B5	0.1	0.5	198	150	0.2037
B6	0.1	0.5	198	135	0.2130

cross-shore direction, while it is kept the same in alongshore direction. The sizes of two individual sediment grains that comprise the non-uniform sediment are 0.1 mm and 0.5 mm, respectively. The mean grain size of the mixed non-uniform sediment is set to be equal to 0.5 mm near the shoreline, which then decrease from a certain distance from the shore boundary seaward to a specified location and finally keeps constant at 0.1 mm. In total, six simulations are carried out for this situation (see Table 6.1 for detail), with the mean grain size over the whole modelling domain ranges from 0.1796 mm to 0.2130 mm.

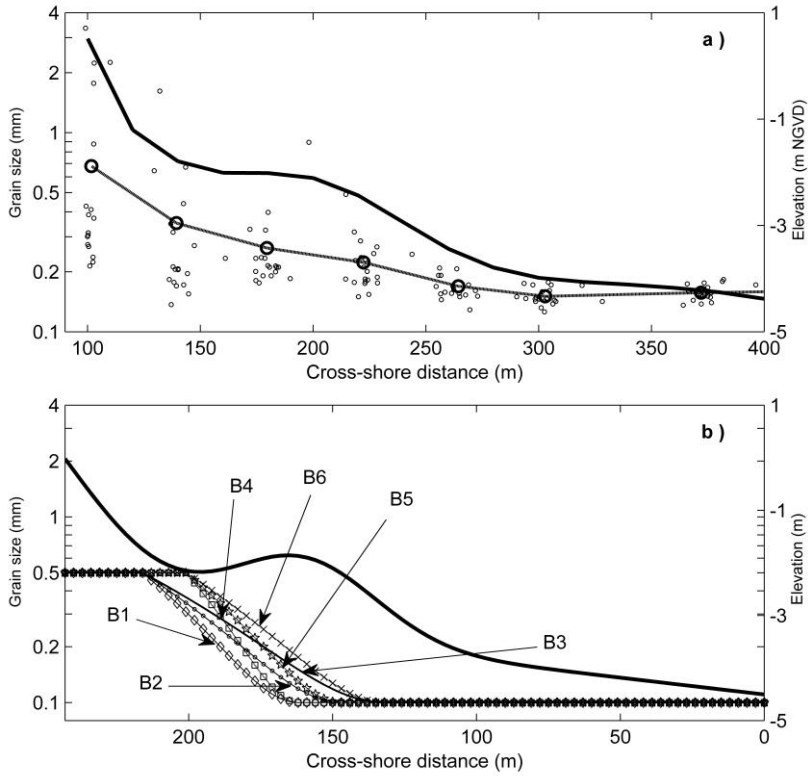

Figure 6.3 Bathymetry (thick solid line) and the cross-shore distribution of sediment grain size for that (a) observed on Duck beach, in North Carolina, USA and (b) used in the numerical simulations with non-uniform sediments. The small circles in (a) indicate the grain size of sediment samples and their corresponding cross-shore positions, whereas the seven large circles indicate the mean grain size for seven representative locations.

It should be noted that the cross shore variations of mean sediment size for these six simulations are generally in consistent with that observed on the Duck Beach, in North Carolina, USA (Figure 6.3), i.e., decreasing in the seaward direction, with the shapes of mean grain size curve are concave upward (Stauble and Cialone, 1996).

6.4 Modeling results

The results of representative cases for the three different types of simulations, i.e., the simulation that 1) using uniform sediment, 2) using non-uniform sediment but its mean grain size is same over the modelling domain, 3) using non-uniform sediment but the mean grain size varies in the cross-shore direction, are described first. Then a detail comparison of the predicted dynamical behaviour of rip channels is conducted. Finally, the variation of dynamical properties of rip channels (mainly growth rate and coupling time) is analysed.

6.4.1 Representative simulation using uniform sediment

The grain size of the representative simulation using uniform sediment is $0.25\,mm$. Here, the growth rate and predominant wavelength are calculated independently for the two types of rip channel systems (the crescentic bar and transverse bar). Specifically, the growth rate for the crescentic bar is calculated by accounting the variables in the domain of $0\,m \le x \le 195\,m$, i.e., the rip channel three-dimensionality $\| h \|$ used in Equation (4.7) is calculated as:

$$\|\mathrm{h}\| = \left(\frac{1}{195} \frac{1}{L_y} \int_0^{195} \int_0^{L_y} h(x,y,t)^2 \, dxdy \right)^{1/2} . \tag{6.8}$$

Similarly, the rip channel three-dimensionality $\| h \|$ used to calculate the growth rate for the transverse bar is written as:

$$\|\mathrm{h}\| = \left(\frac{1}{42} \frac{1}{L_y} \int_{198}^{240} \int_0^{L_y} h(x,y,t)^2 \, dxdy \right)^{1/2} , \tag{6.9}$$

which takes the variable in the domain between $198\,m \le x \le 240\,m$ into account. The predominant wavelength for the crescentic bar and transverse bar are calculated by applying Fourier transform on alongshore bathymetry section at $x = 165\,m$ and $x = 225\,m$ respectively.

Figure 6.4 shows the temporal evolution of growth rate and predominant wavelength for both crescentic bar and transverse bar in the default simulation with uniform sediment ($d_g = 0.25\,mm$). From this figure, we can see that at the beginning 2 days, the crescentic bar is not emerged as during this time the growth rate for the crescentic bar is negative. The non-existence of crescentic bar at this period of time can also be inferred from Figure 6.5a, in which the contour line for $x < 210\,m$ is still quite strait. In contrast, it can be seen that the transverse bar near the shoreline has already been formed. This can be inferred from, for instance, the contour line for $x > 210\,m$, which is no longer strait but meanders alongshore (Figure 6.5a). The detailed information on the emergence process of transverse bar during this time can be seen in Figure 6.4. Clearly, this figure shows that the growth rate increases dramatically and reaches its first maxima (marked as $\Omega_i = 2.6\,day^{-1}$) at about day 1 and then decreases. The predominant wavelength of transverse bar is $32\,m$. After day 2, the growth rate for crescentic bar begins to be positive and continues to increase until about day 7, at which it reaches its maxima value (marked as $\Omega_o = 0.76\,day^{-1}$). At day 7, the crescentic bar appears with its predominant wavelength is $150\,m$ (Figure 6.5b). From day 2 to day 7, the transverse bar is relative stable, as the growth rate is small and the predominant wavelength keeps constant (Figure 6.4). Between day 7 and day 10, the growth rate of crescentic bar is still very large, which suggests the growing up of crescentic bar. It is interesting to note that at the same time the growth rate of transverse bar increases again and reaches its second peak at about day 10. The second peak occurring in the growth rate curve of transverse bar is possibly a result of the onshore migration of crescentic bar. The predominant wavelength of transverse bar between day 7 and day 10 is $150\,m$, which is same as that for the crescentic bar (Figure 6.4). After day 10, both

the growth rates of transverse bar and crescentic bar decrease and approach to zero. At the same time, the predominant wavelengths of crescentic bar and transverse bar keep constant, both of which are $150\,m$. From Figure 6.5c and Figure 6.5f, we can see that the initially emerged small-scale transverse bars in the trough of crescentic bar are all disappear and the small-scale transverse bars are replaced by large-scale transverse bars. This transition seems to be related with the continual increasing and shoreward moving crescentic bar, as the predominant wavelength of transverse bar and crescentic bar are the same.

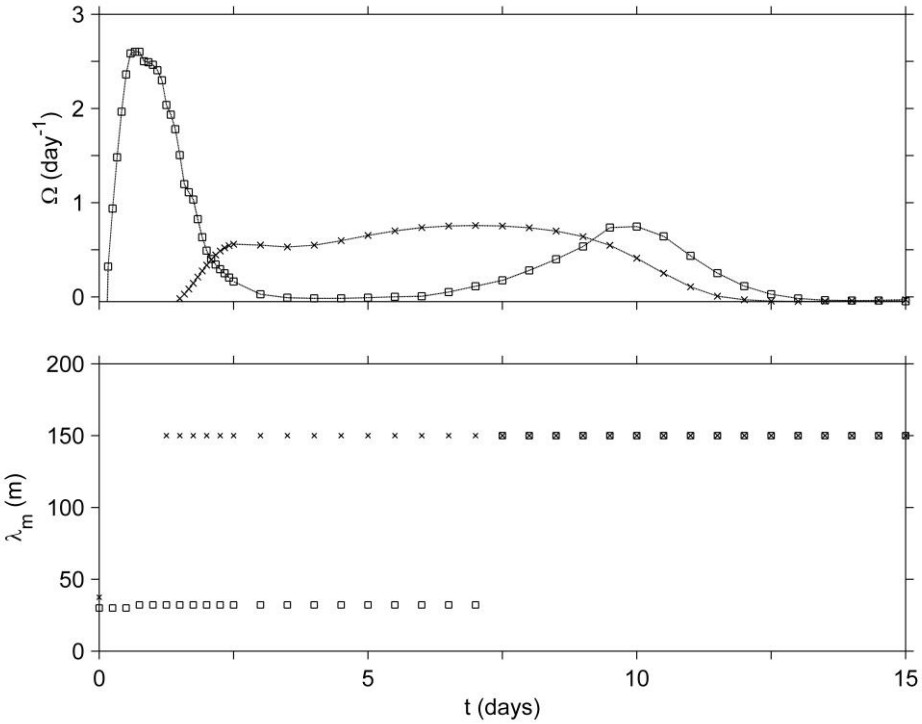

Figure 6.4 The temporal evolution of growth rate and predominant wavelength for simulation using uniform sediment ($d_g = 0.25\,mm$). The crosses and squares represent variables for the crescentic bar near the sandbar crest and transverse bar near the shoreline respectively.

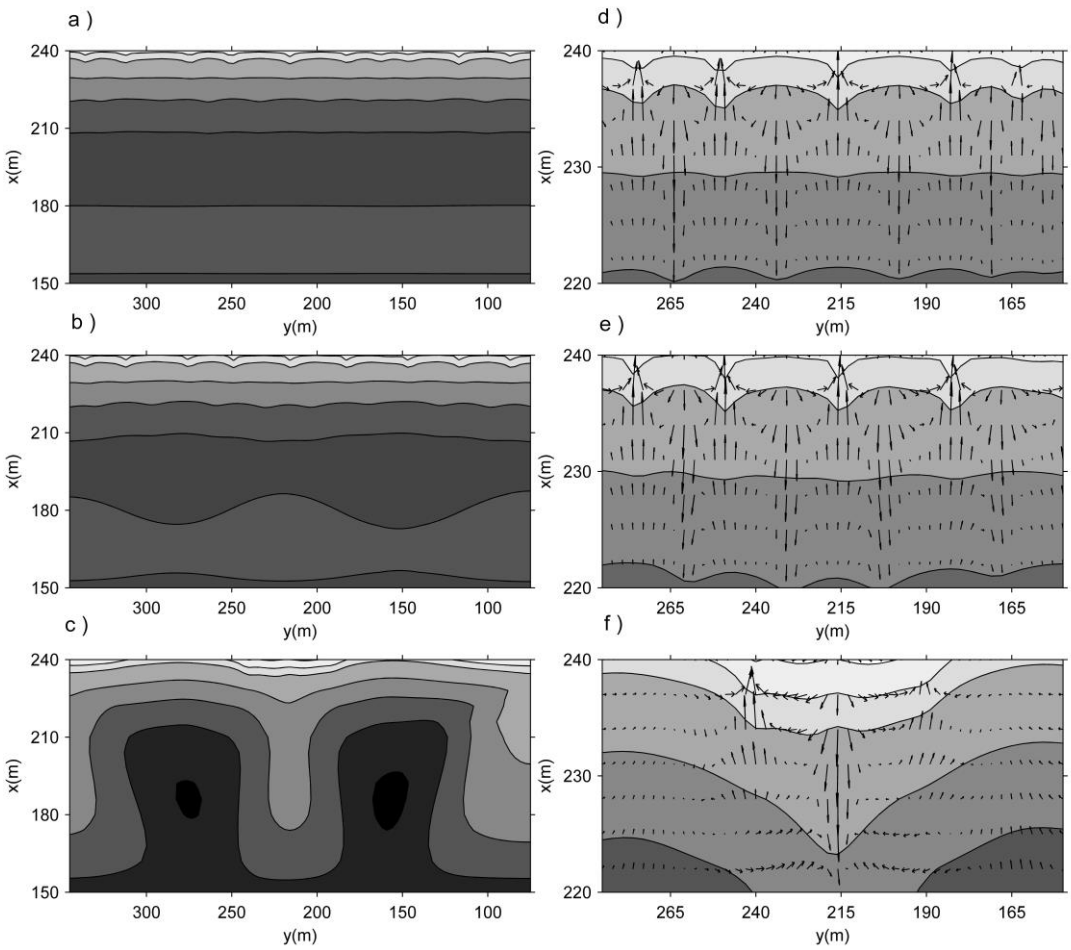

Figure 6.5 The snapshot of seabed in the area between (left panel) 150 m<x<240 m and 75 m<y<345 m and (right panel) 220 m<x<240 m and 150 m<y<285m for (a,d) day 2, (b,e) day 7 and (c,f) day 12.5. The darker colour indicates deeper area.

To test whether the transition of transverse bars from small-scale to large-scale is related to the evolution of crescentic bar, we have run an additional simulation, in which the seabed within $0\,m \le x \le 195\,m$ is frozen by turning off the sediment transport in this area. By doing so, the cresentic bar is not emerged and thus its potential effect on the evolution of transverse bar is excluded. From Figure 6.6, we can see that by turning off the evolution of crescentic bar, the second peak in the growth rate curve for transverse bar disappears and the predominant wavelength of transverse bar after 7.1 days is 32 m only, being same as that of the initially emerged transverse bar. Therefore, we can conclude that the evolution of crescentic bar do

affect the evolution of the transverse bar near the shoreline. Figure 6.6 shows the influence exerted by the crescentic bar begins observable at day 7.1, the time of which will be denoted as the coupling time t_c below. To test whether the interplay between transverse bar and crescentic bar is reciprocal, we have run a simulation in which the evolution of transverse bar is excluded by turning off the sediment transport in area of $x > 195\,m$. It is shown that the evolution of crescentic bar is negligible affected by the evolution of transverse bar, as both the growth rate and predominant wavelength of the crescentic bar is not sensitive to whether the evolution of transverse bar is turned on (Figure 6.6c and Figure 6.6d) .

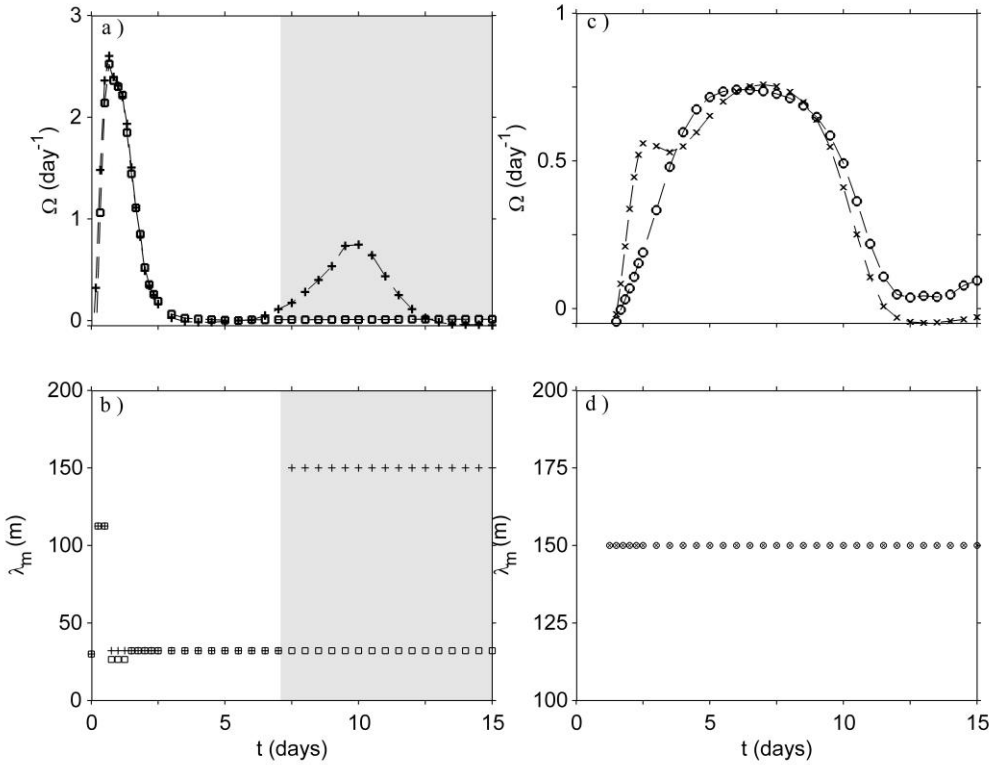

Figure 6.6 The evolution of (a, c) growth rate and (b, d) predominant wavelength for (left panel) transverse bar and (right panel) crescentic bar. The squares in left panel are for simulation with crescentic bar being frozen and the circles in right panel are for simulation with transverse bar being frozen. The pluses in left panel and crosses in right panel are for simulation with seabed not being frozen.

6.4.2 Representative simulations using non-uniform sediment

Figure 6.7 displays the temporal evolution of rip channel indicators for four simulations, which are case A1, case A2, case B4 and the default simulation with uniform sediment ($d_g = 0.25\,mm$) respectively. At first, the correctness of the module that used here to simulate the evolution of multigrain seabed is checked. This is done by comparing the predicted values for case A1 and the default simulation with uniform sediment ($d_g = 0.25\,mm$). Since the individual sediment sizes of both fractions in case A1 is $0.25\,mm$, it is indeed that case A1 is physically equivalent with the simulation with uniform sediment $d_g = 0.25\,mm$. Therefore, it is expected that the rip channel indicator predicted from this case should be the same as that predicted by the simulation using uniform sediment with $d_g = 0.25\,mm$. From Figure 6.7, we can see that the rip channel indicators perfectly agree for these two simulations, which confirms the correctness of the module for modelling the erosion and sedimentation of seabed with non-uniform sediments. From Figure 6.7, we can also see that the predicted values of rip channel response indicators of crescentic bar and transverse bar for case A2 are similar with that obtained from case A1. For example, the growth rate Ω_o for crescentic bar is 0.82 day^{-1} for case A2, which is only slightly larger than that predicted for case A1 ($0.76\,day^{-1}$). However, Figure 6.7 indicates that the predicted growth rate for case B4 is significantly different to the other three cases. The growth rate Ω_o for B4 is 1.76 day^{-1} and is larger that two times of the value for the other three cases (Figure 6.7a). Meanwhile, the growth rate Ω_i for B4 is 1.35 day^{-1} and is only about half of the value for the other three cases. From Figure 6.7b we can also see that the presence time of the second peak in the evolution curve of transverse bar growth rate for B4 is earlier comparing to that for the other three cases. Corresponding with the anticipatory of the second peak in the growth rate, the coupling time for the transverse bar is also shorter for case B4 (Figure 6.7c).

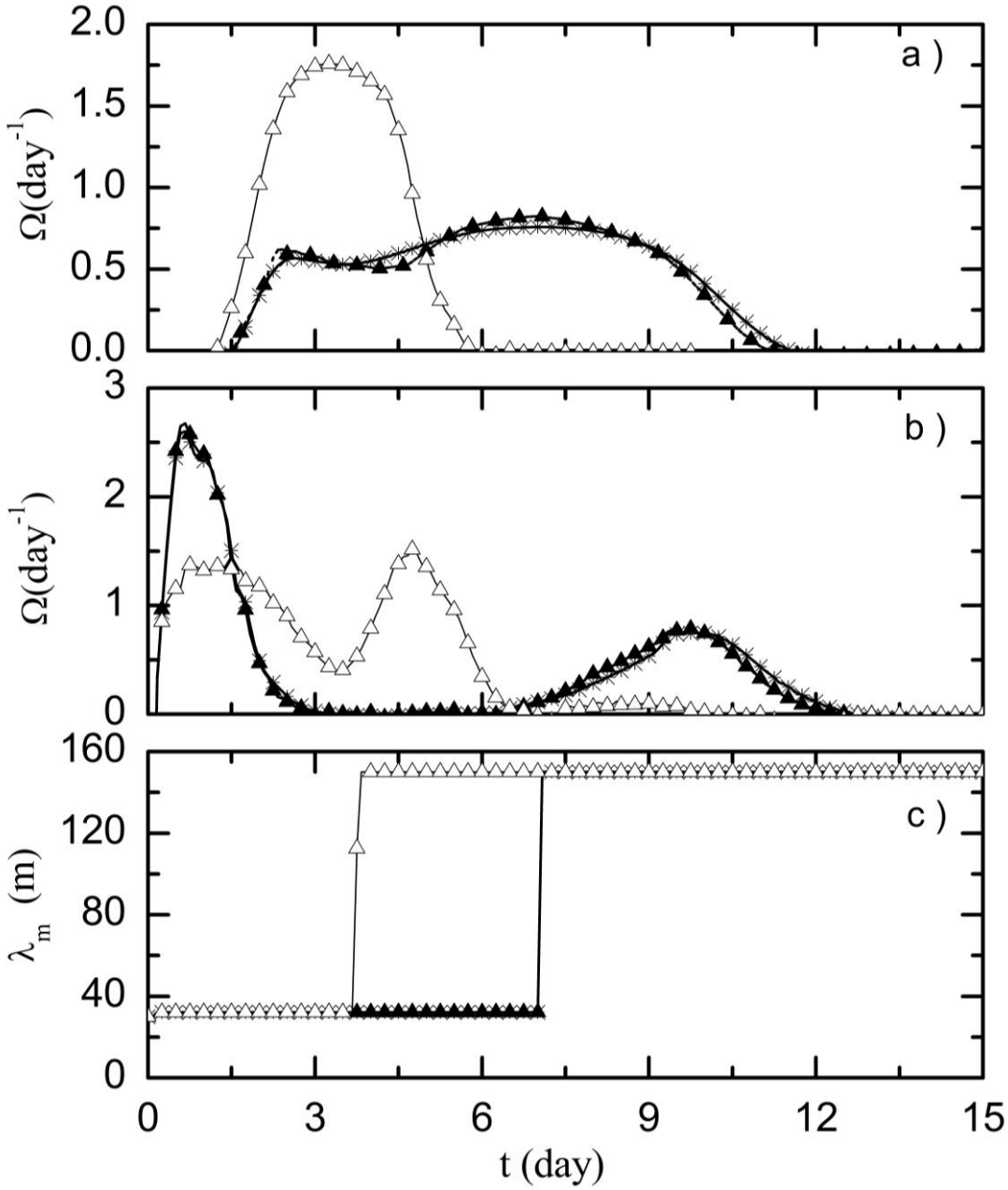

Figure 6.7 The temporal evolution of rip channel response indicators for four selected simulation cases, i.e.,A1 (crosses), A2 (filled triangles), B4 (open triangles) and the default uniform sediment simulation with $d_g = 0.25\,mm$ (pluses). The rip channel indicators are the growth rate of crescentic bar (a), growth rate of transverse bar (b) and the predominant wavelength of transverse bar (c).

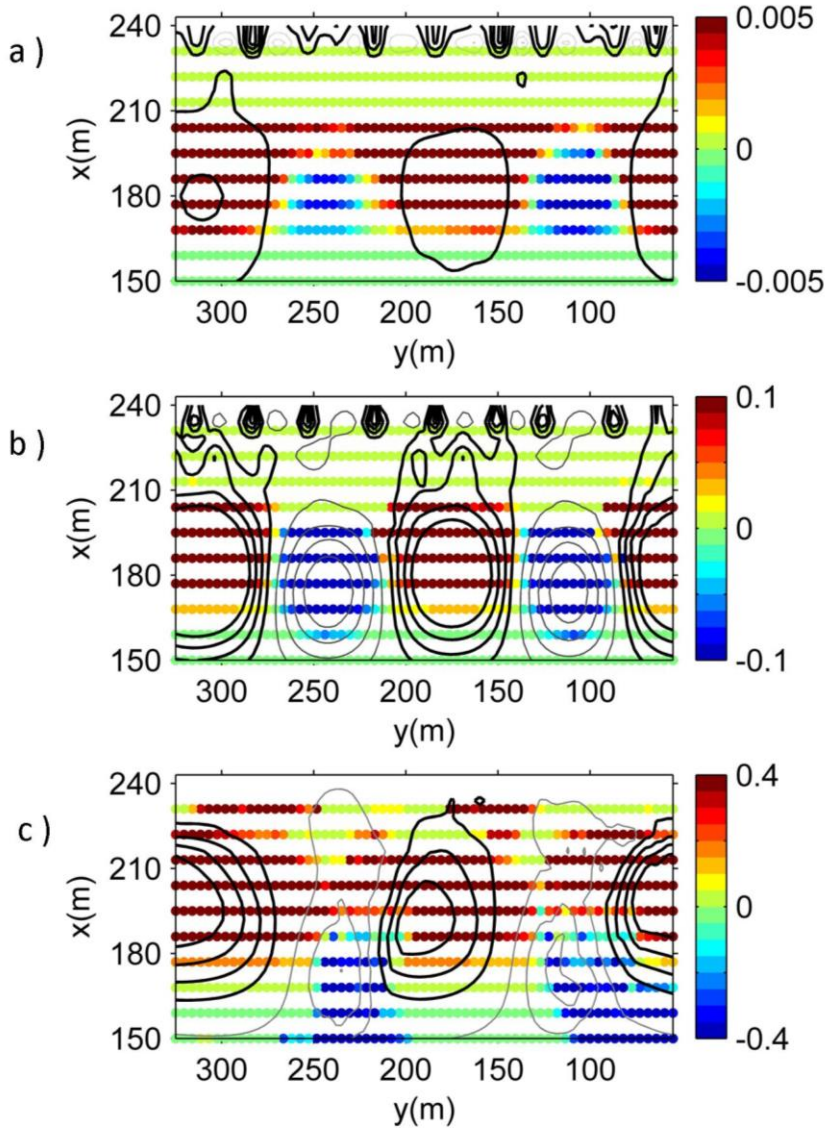

Figure 6.8 Fractional variation for fine sediment and the corresponding seabed at $55\,m \le y \le 325\,m$ and $150\,m \le x \le 240\,m$ for case B4 on (a) day 2, (b) day 4 and (c) day 10. The black thick lines indicate the area of sedimentation and grey thin lines indicate the erosion area. The colorbar indicates the change of fine sediment fraction.

Figure 6.8 displays three snapshots of the variation in the fraction of seabed fine sediment component ($d_g = 0.1\,mm$) and the corresponding seabed bathymetry for case B4. At day 2, the fraction of fine sediment component increases at the area corresponding to the shoal of crescentic bar and decreases in the trough of crescentic bar (Figure 6.8a). Since this change, the mean grain size is no longer alongshore uniform. In detail, the mean grain size decreases on the shoal of crescentic bar and coarsening in the channels. However, the change in the fraction of fine sediment component at this time is very small (about $\pm 0.5\%$). Meanwhile, the fraction of fine sediment component is relative stable at area $x > 200\,m$. As the crescentic bar keeps on growing (deduced from the growth rate evolution curve as shown in Figure 6.7), the mean sediment size in its trough is continuing to be coarsening, while the opposite variation occurs on the shoal of crescentic bar. This variation can be seen by comparing Figure 6.8b with Figure 6.8a as the variation range of the fine sediment fraction significantly increase (from about $\pm 0.5\%$ to nearly $\pm 10\%$). In Figure 6.8b, we can see that the transverse bar at day 4 have not been coupled to the outer crescentic bar and the variation of mean sediment size in the shoreward area ($x > 200\,m$) is still quite small. However, Figure 6.8c shows that both fine sediment fraction and seabed has changed significantly at day 10 compared to day 4 as shown in Figure 6.8b. Specifically, at day 10, the initial formed transverse bars disappeared and are replaced with transverse bars that have same alongshore length scale as that presented at the outer crescentic bar. Moreover, the fine sediment component fraction increases in area close to the shoreline ($x > 200\,m$), especially in the areas corresponding to the rip current feeder.

The variation of mean grain size can be explained as result of rip current circulation and cross-shore distribution of sediment size. Along with the development of crescentic bar, the onshore current over the shoal of crescentic bar can bring sediment from offshore to shoreward. As the sediment is finer in the offshore area (Figure 6.3), the shoreward transport over the shoal can consequently cause a fining in the mean grain size. For the trough area, the current is offshore directed, which can bring the coarse sediment near the shore to seaward. This shoreward origin

sediment mixed with the local sediment at the seaside and consequently can cause an increase in the mean grain size. Along with the onshore migration of crescentic bar, the alongshore variation of mean sediment size becomes obvious. Because of this variation, the alongshore mixing of sediments with different mean grain size occurs clearly, which is driven by the current in the rip feeder.

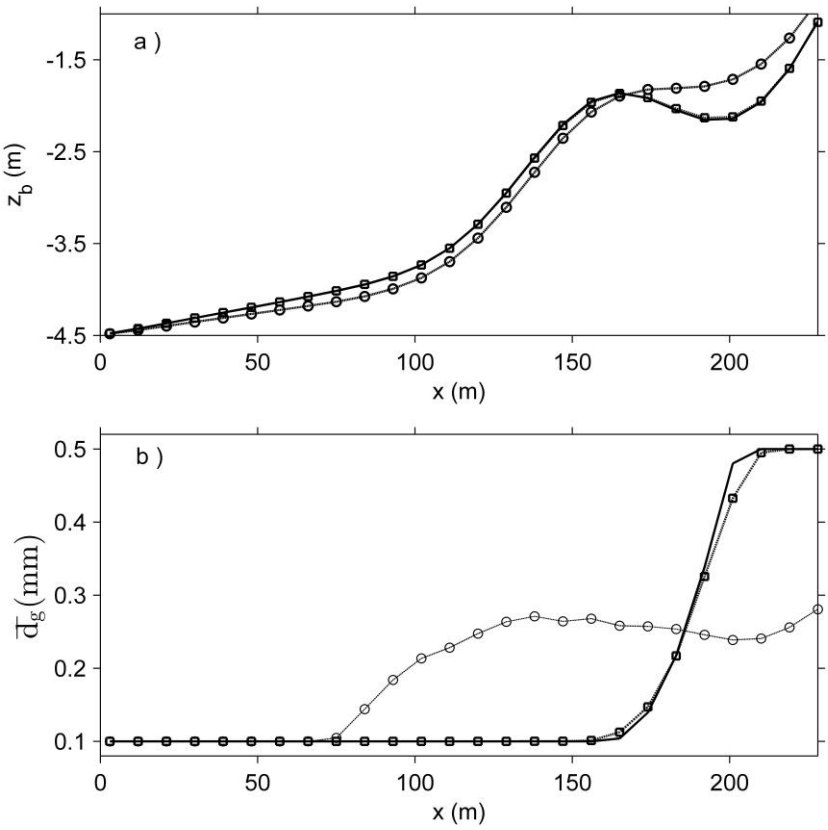

Figure 6.9 The alongshore-averaged (a) bed profile and (b) mean sediment grain size at day 0 (solid line), day 4 (solid line with squares) and day 10 (solid line with circles) for case B4.

Figure 6.9 gives the alongshore-averaged seabed profile and mean sediment grain size for case B4 at day 0, day 4 and day 10 respectively. From this figure, we can see that the depth at area $x < 165\,m$ increases, while the depth at area $x > 165\,m$ decreases. This suggests that the alongshore averaged sandbar migrates onshore, along with which the mean sediment size near the shoreline decreases and the mean sediment size at the seaside increases. Specifically, the mean sediment sizes in the

outer surf zone ($70\,m < x < 165\,m$) are found to increase from 0.1 mm up to $0.27\,mm$. But furthering offshore the mean sediment size is nearly unchanged, while the seabed variation is observable (Figure 6.9a). For area $x > 165\,m$, the mean sediment grain size decreases (up to $0.25\,mm$).

It should be noted that in case there is no initial cross-shore gradient of mean sediment size, the sediment size change as the evolution of seabed is very small. For instance, the alongshore averaged mean sediment size at day 10 for case A2 only changes about 5% compare to its initial value (Figure 6.10).

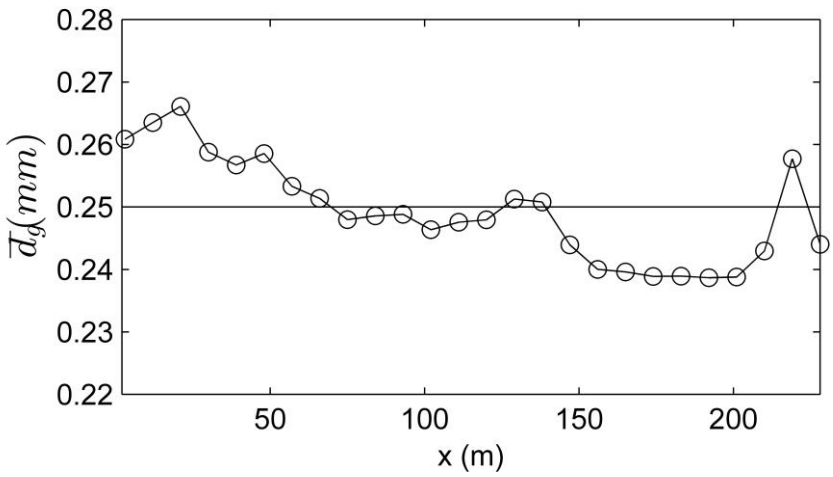

Figure 6.10 Alongshore-averaged mean sediment size for case A2 at day 0 (solid line) and day 10 (solid line with circles).

6.4.3 Temporal evolution of crescentic bar and coupling time

Figure 6.11a displays the saturation time of crescentic bar as a function of the growth rate Ω_o. Similar to that found in Chapter 5, we can see from Figure 6.11a that the saturation time of crescentic bar is highly related with the growth time of crescentic bar, which decreases as the growth rate Ω_o increases. Meanwhile, Figure 6.11b shows that the coupling time is also highly correlated with the growth rate of crescentic bars, which suggests that the coupling time is dependent on the temporal evolution of crescentic bars. As can be seen from Figure 6.11a and Figure 6.11b, the

saturation time of crescentic bar and coupling time for simulations with non-uniform sediment that has an initial cross-shore gradient (Case B1-B6) is much smaller that for the other simulations.

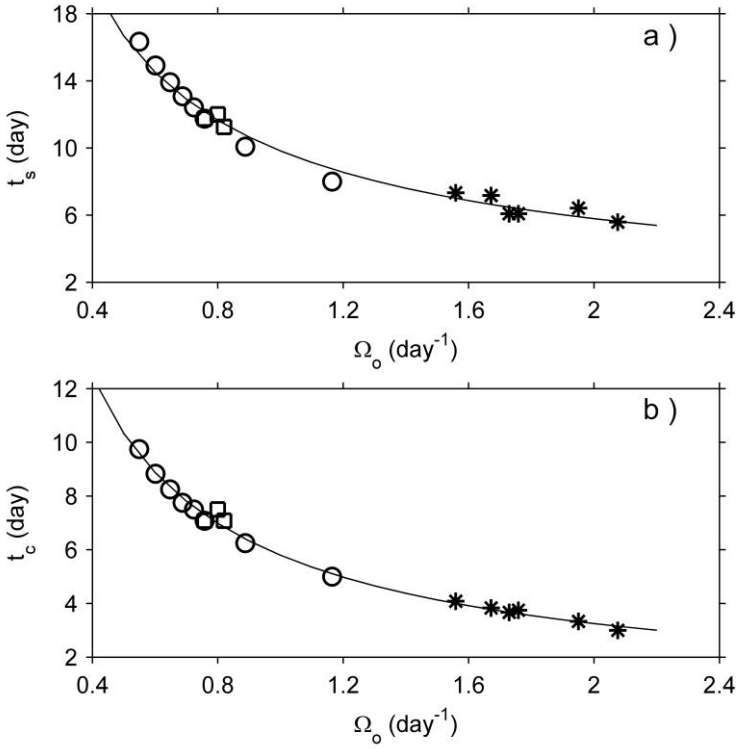

Figure 6.11 Saturation time of crescentic bar (a) and coupling time (b) as a function of the growth rate for crescentic bar. The circles indicate simulations using uniform sediment. The squares for case A1-A3. The stars indicate case B1-B6.

This observation is much clearer in Figure 6.12, in which the saturation time of crescentic bar and coupling times for different simulations are displayed as a function of sediment size (here, $\overline{d_g}$ represents the mean sediment size for simulations using non-uniform sediment and d_g represents the sediment size used in simulations with uniform sediment). For Case A1-A3, the variation of saturation time, coupling time and growth rate for crescentic bar are very small, all of which are nearly same as that obtained from the simulations using uniform sediment with same grain size, i.e., 0.25 *mm* here. However, we also find that the saturation time, coupling times and growth rate for simulations of B1-B6 are significantly different to that obtained

from the simulations using uniform sediment size. From Figure 6.12a we can see that the saturation time of crescentic bar for simulations of B1-B6 is between 5.6 day to 7.2 day, which is significantly smaller than the simulations using uniform sediment (from 8 to 16.3 day). Figure 6.12b shows that the coupling time for simulations using uniform sediment is ranged between 5 day and 9.75 day, while the coupling time for Case B1-B6 ranges between 3 day and 4.08 day. Therefore, interestingly, the coupling time for simulations of B1-B6 all locate outside the range of coupling time that restricted by the simulation using uniform sediment size (Figure 6.12b). Similarly, the entire predicted growth rate for the crescentic bar are also outside of the value range framed by the simulation using uniform sediment size. Specifically, Ω_o ranges between 0.54 day^{-1} and 1.16 day^{-1} for simulations using uniform sediment, while it is between 1.56 day^{-1} and 2.08 day^{-1} for simulations of B1-B6. From Figure 6.12, we can clearly see that in some cases (simulation B1-B6) the temporal evolution properties (e.g., saturation time, coupling time and growth rate) predicted for beach with non-uniform sediment are not a simply averaged value of that obtained from the simulations using uniform sediment.

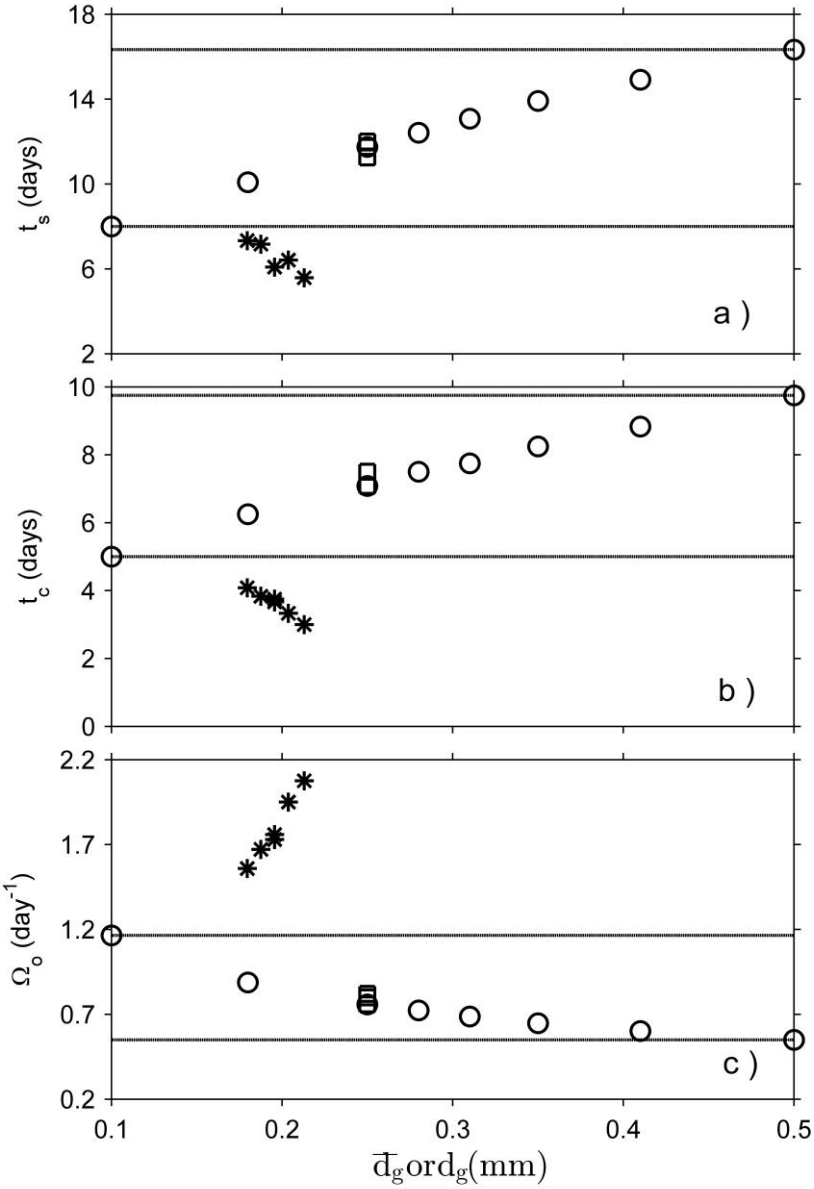

Figure 6.12 (a) Saturation time of crescentic bar, (b) coupling time and (c) growth rate of crescentic bar as a function of (mean) sediment size. The circles indicate simulations using uniform sediment. The squares for case A1-A3. The stars indicate case B1-B6.

Because the observed variation in the temporal evolution properties for simulations B1-B6 are anomalous, we will then set out to explore the underlying mechanism for such a phenomenon. As we found that the saturation time of crescentic bar and coupling time is dependent on the growth rate of crescentic bar, we will then focus

on investigating the reasons for the anomalous change in the growth rate of crescentic bar for Case B1-B6. To do so, we will first set up a series of hydrodynamic experiments to separate roughly the main factors responsible for the anomalous change. In order to keep in concise, case B4 is chosen as a representative case for Case B1-B6. Then, the spatial and local properties of the main factor will be analyzed in detail.

The results of hydrodynamic experiment (for more information on setting up this type of experiment, see Chapter 5) are shown in Figure 6.13. Specifically, in Figure 6.13a, we have included both effects of seabed and sediment concentration. The variation in this sub-figure is quite similar to that shown in Figure 6.12c. In Figure 6.13b, the bed effects are excluded, as we have set the same bed bathymetry for the experiments presented in Figure 6.13b. In order to avoid difficulty in arranging the spatial distribution of sediment fraction, the bathymetry obtained from B4 is used. As we can see, by using this bathymetry the growth rate Ω_o for simulations using uniform sediment decreases, while the variation trend is still same as that presented in Figure 6.12c. The decrease in growth rate Ω_o for simulations using uniform sediment suggests that the amplitude of bed bathymetry of B4 may be small compared to the other simulations (this is because small amplitude tends to reduce the strength of currents). In Figure 6.13c, the effects of sediment concentration are excluded, as we set the sediment size uniformly to be 0.25 *mm* for all experiments presented in Figure 6.13c. We can see that, by excluding the effects of sediment concentration, the variation trend of growth rate Ω_o changes significantly. Especially, the growth rate Ω_o for B4 is now smaller rather than larger to the other simulations. Based on these observations, we can conclude that the anomalous change in the growth rate Ω_o is resulted by the change in sediment concentration.

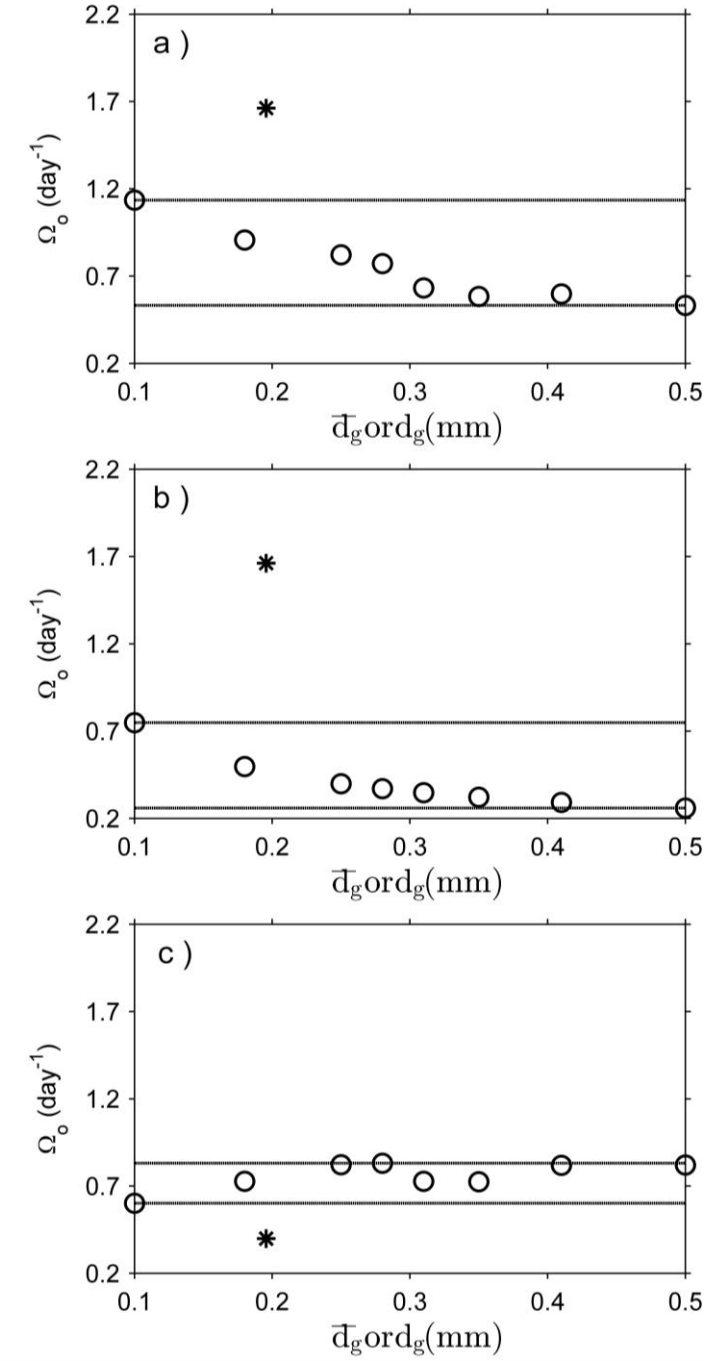

Figure 6.13 Hydrodynamic experiments. (a) Both bed effects and sediment concentration effects are included. (b) Only sediment concentration effects are included. (c) Only bed effects are included.

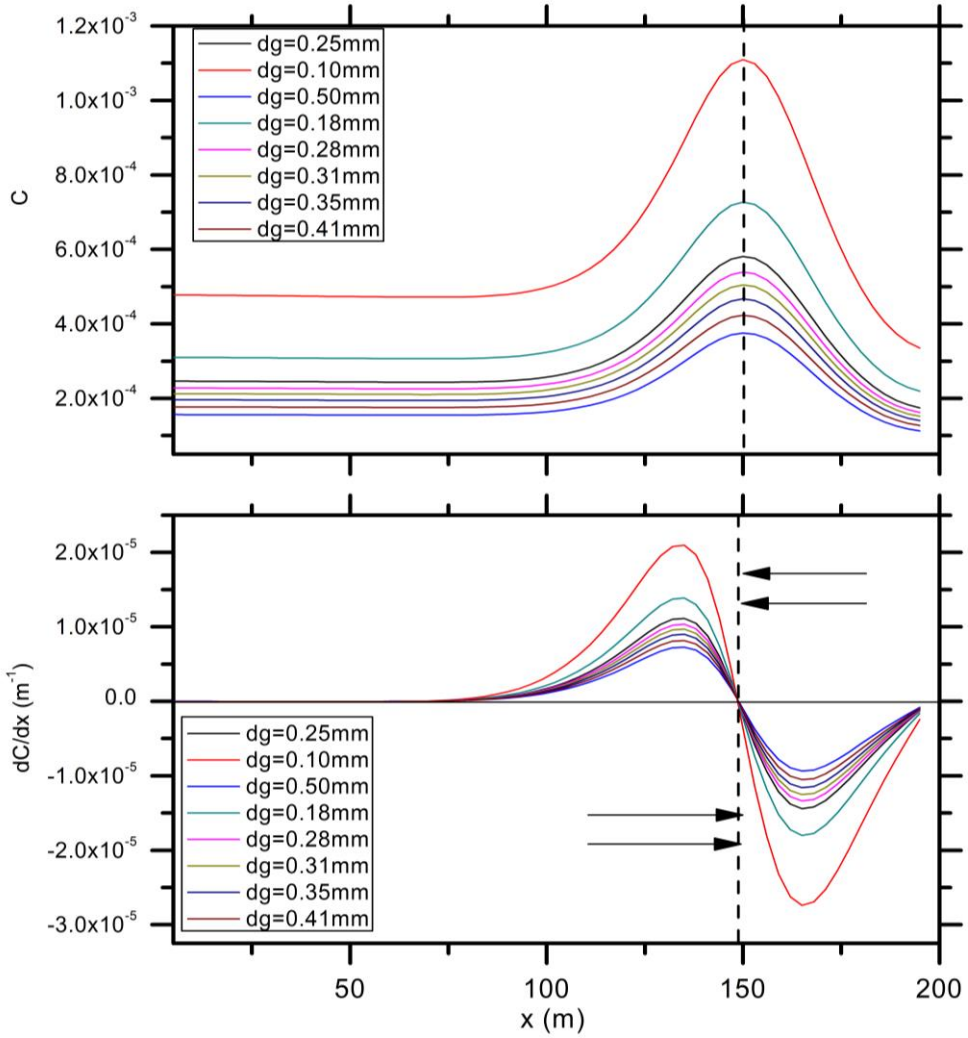

Figure 6.14 The cross-shore distribution of depth-averaged sediment concentration and its gradient for simulations using uniform sediment on alongshore uniform beach, where no perturbation is added. The black arrows indicate the direction of sediment concentration gradient.

To explain why the change in sediment concentration can trigger the anomalous changes in growth rate Ω_o, we have investigated the spatial distribution of sediment concentration and its gradient. The cross-shore distribution of sediment concentration and sediment concentration gradient for the basic state of all simulations with uniform sediment are displayed in Figure 6.14. As we can see, the sediment concentration has a peak near the sandbar crest due to the strong wave

breaking in this area. Furthermore, the sediment concentration decreases both shoreward and seaward near the bar crest.

According to the BEE equation, which written as:

$$(1-p)\frac{\partial h}{\partial t} = -D\vec{v}\nabla C + \nabla \bullet (\Gamma \nabla h), \tag{6.10}$$

the growth of crescentic bar is due to the term $-D\vec{v}\nabla C$. For the normal incident waves, the contribution of alongshore current is negligible to the growth of crescentic bar. In this case, the growth of crescentic bar is mainly generated by the "bed-surf" mechanism (Falqués et al., 2000). This means the growth of crescentic bar is dependent on sign and magnitude of $-u\partial C/\partial x$. In the inner surf zone, the crescentic bar can grow if (1) $u > 0$ (onshore current) over the shoal ($\partial C/\partial x < 0 \Rightarrow -u\partial C/\partial x > 0 \Rightarrow \partial h/\partial t > 0$) or (2) $u < 0$ (offshore current) over the trough ($\partial C/\partial x < 0 \Rightarrow -u\partial C/\partial x < 0 \Rightarrow \partial h/\partial t < 0$). In the outer zone, the opposite direction of current is required, as the direction of sediment concentration gradient has been changed to be onshore oriented.

Figure 6.14 shows for finer sediment, the sediment concentration is higher and the magnitude of sediment concentration gradient (absolute value of $\partial C/\partial x$) is also larger. Due to the larger sediment concentration gradient magnitude, the growth rate Ω_o tends to be larger for finer sediment. Figure 6.15 shows that although the sediment concentration of B4 on alongshore uniform seabed without perturbation locates between the values that predicted from the two simulations using uniform sediment, the magnitude of $\partial C/\partial x$ for simulation B4 is not. The magnitude of $\partial C/\partial x$ for simulation B4 is larger even than that predicted from the simulation using the finest sediment ($d_g = 0.1\,mm$) in the area of $165m < x < 195\,m$, where initially the mean sediment size decreases seaward (see

Table 6.1 and Figure 6.3). It is thus actually the increasing of sediment concentration gradient magnitude triggers the “abnormal” increase in the growth rate for B4.

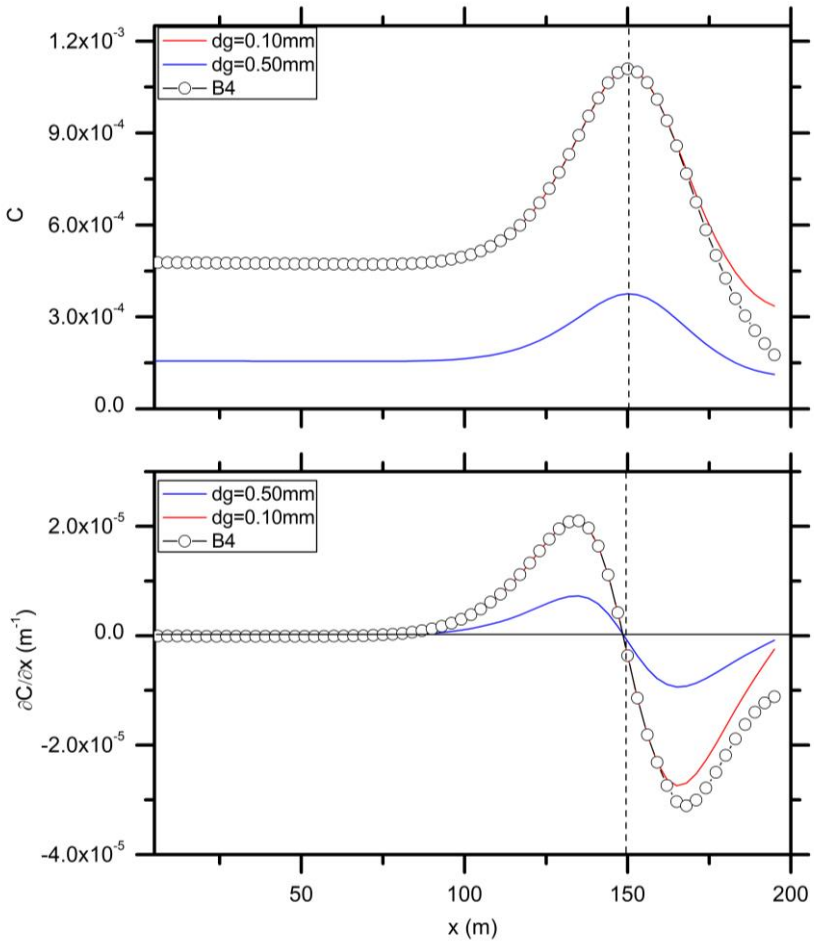

Figure 6.15 The cross-shore distribution of depth-averaged sediment concentration and its gradient for simulation B4 and two simulations with uniform sediment ($d_g = 0.1\,mm, d_g = 0.5\,mm$) on alongshore uniform seabed without perturbation.

6.5 Discussion

In this Chapter, the simulations that considering both uniform and non-uniform sediment are carried out. Due to the simulations using non-uniform sediment are incorporated, the spatial distribution pattern and evolution of sediment size becomes possible to be studies. In some situation (sediment size initially decrease offshore as

simulations of B1-B6), we have successfully reproduced the same distribution pattern of sediment size as that observed from the field, i.e., the mean sediment size is fine over the shoals and coarse in the channel (Gallagher et al., 2011; MacMahan et al., 2005). Besides this, we also find that if the waves can last long enough, the sediment size in the rip feeder area can start to decrease, which seems to caused by the alongshore mixing of sediment. However, it is not easy to compare this with the field observation. Because even in the study carried out by Gallagher et al. (2011), where the measured sediment size data is high resolution in both spatial and temporal scale, the corresponding waves and bathymetry data is limited. Thus, we are not able to know whether the waves are long enough for the fining of sediment size in the rip feeder area to occur. In the simulations that using an initial cross-shore varying mean sediment size, we find the mean grain size tend to be finer in the inner surf zone and coarser in the outer surf zone. This is because the current (rip current) over the shoals (trough) of crescentic bar can bring sediments onshore (offshore) from the seaside (shore side) where the sediment is relatively fine (coarse). Actually, this result is also consistent with the field observation. van Rijn (1998) stated that the fine sediment transported offshore during the storm weather can be transported back to shore during calm weather.

Beside the spatial distribution and dynamical behavior of sediment size are in general consistent with the field observation, we find the prediction of saturation time for rip channels (here, crescentic bar) is much closer to that observed from the field. As we can see that the saturation time predicted from simulations of B1-B6 is only about 5 days. This value is quite close to that reported by van Enckevort et al. (2004), who suggests that the observed response time (the concept of response time used by van Enckevort et al. (2004) is consistent with the concept of saturation time used here) is about 3 days. Moreover, the predicted value of saturation time for simulation of B1-B6 is also closer than the simulations using uniform sediment to the field observation about the residue time of LBT state on Duck Beach. For more information on the residue time of LBT state on Duck Beach, see Chapter 4.

6.6 Summary

In this chapter, we compared the prediction of rip channel dynamics and the coupling behavior among transverse bar and crescentic bar for uniform and non-uniform sediments. We find that for coupling behavior between transverse bar and crescentic bar is one way, with the dynamics of crescentic bar can have influence on the dynamics of transverse bar but not vice versa. For the situation that the mean sediment size vary cross-shore, the coupling time can be strongly reduced comparing to that for the uniform sediment. This is because the growth rate of the crescentic bar increases for this situation, as the increase in the magnitude of sediment concentration gradient. As for the case that the mean sediment size vary cross-shore the magnitude of sediment concentration gradient is not a simple average of the values for the uniform sediments, the temporal evolution properties, such as growth rate, saturation time and coupling time, cannot be obtained by averaging the corresponding values obtained for the uniform sediment. This demonstrate that the coastal sediment heterogeneity is critical to the evolution of individual alongshore non-uniform sandbar features and also the coupling behaviour among different morphological patterns on beach.

Chapter 7

Conclusions and future works

7.1 Conclusions

The open source program XBeach has been adopted for the first time to study the self-organization behavior of rip channels with focusing on the effects of sediment size.

For the uniform sediment, we find that the grain size can affect a number of aspects of rip channel dynamics. With increasing grain size, both longshore migration speed and growth rate decrease significantly, while the response and saturation times increase. On the other hand, the influence of grain size on the geometrical properties of the rip channel seems to be much less pronounced, as the wavelength of the channels hardly changes and the three-dimensionality features only vary slightly. The "global analysis" method is applied to investigate the mechanism underlying the variations of growth rate and migration speed for varying sediment size. The calculations reveal that these variations are mainly caused by the amount of sea bed sediments being stirred up which is clearly grain-size-dependent. Quantitative relationships between predicted rip channel characteristics, sediment grain size and the hydrodynamic conditions are tentatively established **(answer to research question one).**

Furthermore, we have also investigated the heterogeneous sediment effects on the rip channel system. We find that in case the mean sediment size does not vary in cross-shore, the behaviour of rip channels is quite similar to that obtained for the uniform sediment with equivalent sediment size. Therefore, in this situation, the heterogeneous sediment can be roughly instead by the homogeneous sediment that with the same averaged grain size **(answer to research question three).**

However, we also find that when the sediment size varies cross-shore, the temporal evolution behaviour of rip channel is quite different to that for the uniform sediment. Specifically, the indicators such as growth rate, saturation time, coupling time can locate outside the range of values restricted by that using uniform sediment. A deep analysis shows that such a phenomenon is triggered by the fact that the magnitude of sediment concentration gradient depends on the spatial distribution of sediment size. Therefore, in this case the heterogeneous sediment can not be instead by uniform sediment size with equivalent mean sediment size **(answers to research question two).**

7.2 Recommendations for future works

Suggestions for model improvement

In this thesis, many processes that can potentially play a role in the formation and evolution of rip channels are not fully taken into account. For instance, the three dimension structures of wave-induced current is ignored, as the offshore-oriented undertow and onshore-oriented current deduced by wave skewness and asymmetry are turned off in the present thesis. However, properly incorporation of this 3-D structures of currents is still challengeable. Indeed, XBeach model has been shown to predict observed storm beach response with a reasonable degree of accuracy (Roelvink et al., 2009; Tiessen et al., 2010). But, under calm to moderate waves, conditions that rip channel commonly developed and evolved, the wave-induced currents can be overwhelmed by oscillatory wave-motions and XBeach model tend to overestimate the erosion of bathymetry, especially in the swash zone (Orzech et al., 2011) , which tends to be caused by the underestimation of onshore sediment transport. Further works are required to validate the XBeach model results with both undertow and wave nonlinearity processes turned on using the recent laboratory data, in which the accretive morphological evolution has been well reproduced

(e.g.,Emanuel, 2005; Murray, 2004). Furthermore, the influence of sediment size on the roughness of seabed is not considered. In fact, changing the size of sediment can subsequently has an influence on the seabed roughness, which then can affect the strength of current and finally results impacts on the evolution of rip channels.

While studying the formation and evolution of rip channels, some processes are parameterized and thus empirical parameter is used in the formulations. One of the typical examples is the bed slope coefficient that used in the sediment transport formulation. This parameter concerns to the downslope transport of sediment and thus is relevant to the saturation of rip channels. However, the value of this parameter has a large degree of uncertainty (Castelle and Ruessink, 2011; Garnier et al., 2006; Garnier et al., 2008). Further research is required on this point.

Suggestions for data modelling integration

The research presented in this thesis is based on numerical simulations with the aim to investigate the effects of sediment size on the self-organization behavior of rip channels. These simulations are idealized, such as they start from an idealized bathymetry and assume the wave field are constant. Therefore, the predictions can only been compared to the field observations in a qualitative way. However, a more precise comparison with the observations of rip channel system is encouraged to be carried out in the future.

To do so, we recommend to study the formation and evolution of rip channels beginning from an accurate in situ-measured beach bathymetry and using the measured wave conditions. This bathymetry should be measured immediately after the storm in order to fit the model concept. In order to examine the effects of sediment size and its spatial distribution on the dynamical behavior of rip channels, the beaches that consists of non-uniform sediment should first be selected out. Then, detailed measurement of the spatial distribution of sediment size and sediment concentration on these beaches should be conducted.

The comparison between model simulation and field observation data from these beaches can be carried out at least in two aspects. First, the observed spatial distribution of sediment concentration (especially, in the cross-shore direction) can be used to compare with the model output, in order to examine how significant the spatial distribution of sediment size can have influence on the sediment concentration gradient for a given beach. Second, comparing the hindcasted dynamical behavior of rip channels to that observed from the these beaches (either based on in situ-measurement or video-inferred bathymetries) directly can be another important test on both of the model performance and the effects of sediment size.

Bibliography

Almar, R. et al., 2008. Video observations of beach cusp morphodynamics. Marine Geology, 254(3): 216-223.

Austin, M., Scott, T., Brown, J., Brown, J. and MacMahan, J., 2009. Macrotidal rip current experiment: Circulation and dynamics. Journal of Coastal Research: 24-28.

Bailard, J.A. and Inman, D.L., 1981. An energetics bedload model for a plane sloping beach: Local transport. Journal of Geophysical Research: Oceans (1978–2012), 86(C3): 2035-2043.

Baldock, T., Holmes, P., Bunker, S. and Van Weert, P., 1998. Cross-shore hydrodynamics within an unsaturated surf zone. Coast. Eng., 34(3): 173-196.

Brocchini, M., Kennedy, A., Soldini, L. and Mancinelli, A., 2004. Topographically controlled, breaking-wave-induced macrovortices. Part 1. Widely separated breakwaters. J. Fluid Mech., 507: 289-307.

Calvete, D., Coco, G., Falqués, A. and Dodd, N., 2007. (un)predictability in rip channel systems. Geophysical Research Letters, 34(5): L05605.

Calvete, D., Dodd, N., Falqués, A. and Van Leeuwen, S., 2005. Morphological development of rip channel systems: Normal and near-normal wave incidence. Journal of Geophysical research, 110(C10): C10006.

Castelle, B., Bonneton, P., Dupuis, H. and Sénéchal, N., 2007. Double bar beach dynamics on the high-energy meso-macrotidal french aquitanian coast: A review. Marine Geology, 245(1): 141-159.

Castelle, B. and Coco, G., 2012. The morphodynamics of rip channels on embayed beaches. Continental Shelf Research, 43(0): 10-23.

Castelle, B. et al., 2012. On the impact of an offshore bathymetric anomaly on surf zone rip channels. Journal of Geophysical Research: Earth Surface (2003–2012), 117(F1).

Castelle, B. and Ruessink, B.G., 2011. Modeling formation and subsequent nonlinear evolution of rip channels: Time-varying versus time-invariant wave forcing. J. Geophys. Res.-Earth Surf., 116: F04008.

Castelle, B. et al., 2010a. Coupling mechanisms in double sandbar systems. Part 1: Patterns and physical explanation. Earth Surface Processes and Landforms, 35(4): 476-486.

Coco, G. and Murray, A.B., 2007. Patterns in the sand: From forcing templates to self-organization. Geomorphology, 91(3-4): 271-290.

Damgaard, J., Dodd, N., Hall, L. and Chesher, T., 2002. Morphodynamic modelling of rip channel growth. Coast. Eng., 45(3-4): 199-221.

de Schipper, M.A., Reniers, A.J.H.M., Ranasinghe, R. and Stive, M.J.F., 2014. The influence of sea state on formation speed of alongshore variability in surf zone sand bars. Coast. Eng., 91(0): 45-59.

Dodd, N. et al., 2003. Understanding coastal morphodynamics using stability methods. Journal of Coastal Research, 19(4): 849-866.

Dongeren, A.V. and Svendsen, I.A., 1997. Absorbing-generating boundary condition for shallow water models. Journal of waterway, port, coastal, and ocean engineering, 123(6): 303-313.

Drønen, N. and Deigaard, R., 2007. Quasi-three-dimensional modelling of the morphology of longshore bars. Coast. Eng., 54(3): 197-215.

Durbarbier, B. and Castelle, B., 2011. Numerical modeling investigation of the influence of tide on the formation and subsequent nonlinear evolution of rip channels. Journal of Coastal Research, SI64: 1018 - 1022.

Emanuel, K., 2005. Increasing destructiveness of tropical cyclones over the past 30 years. Nature, 436(7051): 686-688.

Falqués, A., Coco, G. and Huntley, D.A., 2000. A mechanism for the generation of wave-driven rhythmic patterns in the surf zone. J. Geophys. Res.-Oceans, 105(C10): 24071-24087.

Falqués, A. et al., 2008. Rhythmic surf zone bars and morphodynamic self-organization. Coast. Eng., 55(7-8): 622-641.

Feddersen, F., Guza, R., Elgar, S. and Herbers, T., 2000. Velocity moments in alongshore bottom stress parameterizations. Journal of Geophysical Research, 105(C4): 8673-8686.

Ferrer, P. et al., 2011. Hydrodynamics over a microtidal double crescentic barred beach in low energetic conditions (leucate beach, france). Journal of Coastal Research: 2032-2036.

Foti, E. and Blondeaux, P., 1995. Sea ripple formation: The heterogeneous sediment case. Coast. Eng., 25(3): 237-253.

Gallagher, E.L., Elgar, S. and Guza, R., 1998. Observations of sand bar evolution on a natural beach. Journal of Geophysical research, 103: 3203-3215.

Gallagher, E.L., MacMahan, J., Reniers, A.J.H.M., Brown, J. and Thornton, E.B., 2011. Grain size variability on a rip-channeled beach. Marine geology, 287(1–4): 43-53.

Gallop, S.L., Bryan, K.R., Coco, G. and Stephens, S., 2011. Storm-driven changes in rip channel patterns on an embayed beach. Geomorphology, 127(3): 179-188.

Garnier, R., Calvete, D., Dodd, N. and Falqués, A., 2007. Modelling the interaction between transverse and crescentic bar systems, River, coastal and estuarine morphodynamics: Rcem 2007, two volume set. Taylor & Francis, pp. 931-937.

Garnier, R., Calvete, D., Falqués, A. and Caballeria, M., 2006. Generation and nonlinear evolution of shore-oblique/transverse sand bars. J. Fluid Mech., 567: 327-360.

Garnier, R., Calvete, D., Falqués, A. and Dodd, N., 2008. Modelling the formation and the long-term behavior of rip channel systems from the deformation of a longshore bar. J. Geophys. Res.-Oceans, 113(C7): C07053.

Garnier, R., Dodd, N., Falqués, A. and Calvete, D., 2010a. Mechanisms controlling crescentic bar amplitude. J. Geophys. Res.-Earth Surf., 115: F02007,10.

Garnier, R., Falqués, A., Calvete, D., Thiébot, J. and Ribas, F., 2013. A mechanism for sandbar straightening by oblique wave incidence. Geophysical Research Letters, 40(11): 2726-2730.

Garnier, R., Ortega-Sánchez, M., Losada, M.A., Falqués, A. and Dodd, N., 2010b. Beach cusps and inner surf zone processes: Growth or destruction? A case study of trafalgar beach (cádiz, spain). Scientia Marina, 74(3): 539-553.

Guillén, J. and Hoekstra, P., 1996. The “equilibrium” distribution of grain size fractions and its implications for cross-shore sediment transport: A conceptual model. Marine geology, 135(1–4): 15-33.

Haller, M.C., Dalrymple, R.A. and Svendsen, I.A., 2002. Experimental study of nearshore dynamics on a barred beach with rip channels. Journal of Geophysical Research: Oceans (1978–2012), 107(C6): 14-1-14-21.

Henderson, S.M. and Bowen, A., 2003. Simulations of dissipative, shore-oblique infragravity waves. Journal of Physical Oceanography, 33(8): 1722-1732.

Hirano, M., 1971. River bed degradation with armouring. Trans. Jpn. Soc. Civ. Eng, 3(2): 194-195.

Holland, K.T. and Elmore, P.A., 2008. A review of heterogeneous sediments in coastal environments. Earth-Science Reviews, 89(3–4): 116-134.

Holman, R.A. and Bowen, A.J., 1982. Bars, bumps, and holes: Models for the generation of complex beach topography. Journal of Geophysical Research-Oceans and Atmospheres, 87(NC1): 457-468.

Holman, R.A., Symonds, G., Thornton, E.B. and Ranasinghe, R., 2006. Rip spacing and persistence on an embayed beach. J. Geophys. Res.-Oceans, 111(C1): C01006,10.1029/2005JC002965.

Holthuijsen, L., Booij, N. and Herbers, T., 1989. A prediction model for stationary, short-crested waves in shallow water with ambient currents. Coast. Eng., 13(1): 23-54.

Jamal, M., Simmonds, D. and Magar, V., 2014. Modelling gravel beach dynamics with xbeach. Coast. Eng., 89: 20-29.

Johnson, R., 2007. Edge waves: Theories past and present. Philosophical Transactions of the Royal Society A: Mathematical, Physical and Engineering Sciences, 365(1858): 2359-2376.

Jones, A.R., Murray, A., Lasiak, T.A. and Marsh, R.E., 2008. The effects of beach nourishment on the sandy ‐ beach amphipod exoediceros fossor: Impact and recovery in botany bay, new south wales, australia. Marine Ecology, 29(s1): 28-36.

Kennedy, A.B. and Thomas, D., 2004. Drifter measurements in a laboratory rip current. Journal of Geophysical Research: Oceans (1978–2012), 109(C8).

Kinsman, B., 2013. Wind waves: Their generation and propagation on the ocean surface.

Klein, M. and Schuttelaars, H., 2005. Morphodynamic instabilities of planar beaches: Sensitivity to parameter values and process formulations. J. Geophys. Res, 110: F04S18.

Komar, P.D., 1998. Beach processes and sedimentation. Prentice-Hall, Englewood Cliffs,NJ.

Konicki, K.M. and Holman, R.A., 2000. The statistics and kinematics of transverse sand bars on an open coast. Marine geology, 169(1-2): 69-101.

Kulkarni, C.D., Levoy, F., Monfort, O. and Miles, J., 2004. Morphological variations of a mixed sediment beachface (teignmouth, uk). Continental Shelf Research, 24(11): 1203-1218.

Lafon, V. et al., 2005. Morphodynamics of nearshore rhythmic sandbars in a mixed-energy environment (sw france): 2. Physical forcing analysis. Estuarine, Coastal and Shelf Science, 65(3): 449-462.

Leatherman, S.P., 2012. Undertow, rip current, and riptide. Journal of coastal research, 28(4): iii-v.

Lippmann, T. and Holman, R.A., 1989. Quantification of sand bar morphology: A video technique based on wave dissipation. Journal of Geophysical Research: Oceans (1978–2012), 94(C1): 995-1011.

Lippmann, T.C. and Holman, R.A., 1990. The spatial and temporal variability of sand bar morphology. Journal of Geophysical Research: Oceans (1978–2012), 95(C7): 11575-11590.

MacMahan, J. et al., 2010. Mean lagrangian flow behavior on an open coast rip-channeled beach: A new perspective. Marine Geology, 268(1): 1-15.

MacMahan, J.H., Thornton, E.B., Stanton, T.P. and Reniers, A.J.H.M., 2005. Ripex: Observations of a rip current system. Marine geology, 218(1): 113-134.

McCall, R. et al., 2014. Modelling storm hydrodynamics on gravel beaches with xbeach-g. Coast. Eng., 91: 231-250.

McLachlan, A. and Brown, A.C., 2010. The ecology of sandy shores. Academic Press.

Murray, A.B., 2004. Rip channel development on nonbarred beaches: The importance of a lag in suspended ‐ sediment transport. Journal of Geophysical Research: Oceans (1978–2012), 109(C4).

Ojeda, E., Ruessink, B. and Guillen, J., 2008. Morphodynamic response of a two-barred beach to a shoreface nourishment. Coast. Eng., 55(12): 1185-1196.

Orzech, M.D., Reniers, A.J.H.M., Thornton, E.B. and MacMahan, J.H., 2011. Megacusps on rip channel bathymetry: Observations and modeling. Coast. Eng., 58(9): 890-907.

Orzech, M.D., Thornton, E.B., MacMahan, J.H., O'Reilly, W.C. and Stanton, T.P., 2010. Alongshore rip channel migration and sediment transport. Marine Geology, 271(3): 278-291.

Padmalal, D. and Maya, K., 2014. Sources of sand and conservation, Sand mining. Springer, pp. 155-160.

Price, T., Castelle, B., Ranasinghe, R. and Ruessink, B., 2013. Coupled sandbar patterns and obliquely incident waves. Journal of Geophysical Research: Earth Surface, 118(3): 1677-1692.

Price, T.D. and Ruessink, B., 2013. Observations and conceptual modelling of morphological coupling in a double sandbar system. Earth Surface Processes and Landforms, 38(5): 477-489.

Price, T.D. and Ruessink, B.G., 2011. State dynamics of a double sandbar system. Continental Shelf Research, 31(6): 659-674.

Quartel, S., 2009. Temporal and spatial behaviour of rip channels in a multiple-barred coastal system. Earth Surface Processes and Landforms, 34(2): 163-176.

Ranasinghe, R., Symonds, G., Black, K. and Holman, R., 2004. Morphodynamics of intermediate beaches: A video imaging and numerical modelling study. Coast. Eng., 51(7): 629-655.

Reeve, D., Chadwick, A. and Fleming, C., 2004. Coastal engineering: Processes, theory and design practice. CRC Press.

Reniers, A., Roelvink, J. and Thornton, E., 2004. Morphodynamic modeling of an embayed beach under wave group forcing. Journal of Geophysical research, 109(C1): C01030.

Ribas, F. and Kroon, A., 2007. Characteristics and dynamics of surfzone transverse finger bars. Journal of Geophysical Research, 112(F3): F03028.

Roelvink, D. et al., 2009. Modelling storm impacts on beaches, dunes and barrier islands. Coast. Eng., 56(11-12): 1133-1152.

Roelvink, D. et al., 2010. Xbeach model description and manual. Unesco-IHE Institute for Water Education, Deltares and Delft University of Tecnhology. Report June, 21: 2010.

Roelvink, J.A., 1993. Surf beat and its effect on cross-shore profiles, Technische Universiteit Delft.

Roos, P.C., Wemmenhove, R., Hulscher, S.J., Hoeijmakers, H.W. and Kruyt, N., 2007. Modeling the effect of nonuniform sediment on the dynamics of offshore tidal sandbanks. Journal of Geophysical Research: Earth Surface (2003–2012), 112(F2).

Ruessink, B., Coco, G., Ranasinghe, R. and Turner, I.L., 2007. Coupled and noncoupled behavior of three‐dimensional morphological patterns in a double sandbar system. Journal of Geophysical Research: Oceans (1978–2012), 112(C7).

Ruessink, B., Van Enckevort, I., Kingston, K. and Davidson, M., 2000. Analysis of observed two-and three-dimensional nearshore bar behaviour. Marine Geology, 169(1): 161-183.

Sallenger, A.H., Holman, R.A. and Birkemeier, W.A., 1985. Storm-induced response of a nearshore-bar system. Marine Geology, 64(3): 237-257.

Scott, T., Russell, P., Masselink, G., Wooler, A. and Short, A., 2007. Beach rescue statistics and their relation to nearshore morphology and hazards: A case study for southwest england. Journal of Coastal Research, 50: 1-6.

Short, A., 1979. Three dimensional beach-stage model. The Journal of Geology: 553-571.

Short, A., 1985. Rip-current type, spacing and persistence, narrabeen beach, australia. Marine Geology, 65(1): 47-71.

Short, A.D., 1999. Handbook of beach and shoreface morphodynamics. J. Wiley and Sons Ltd, Chichester, UK.

Smit, M., Reniers, A. and Stive, M., 2012. Role of morphological variability in the evolution of nearshore sandbars. Coast. Eng., 69: 19-28.

Smit, M.W.J. et al., 2007. The role of video imagery in predicting daily to monthly coastal evolution. Coast. Eng., 54(6–7): 539-553.

Smit, M.W.J., Reniers, A.J.H.M., Ruessink, B.G. and Roelvink, J.A., 2008. The morphological response of a nearshore double sandbar system to constant wave forcing. Coast. Eng., 55(10): 761-770.

Sonu, C.J., 1973. Three-dimensional beach changes. The Journal of Geology: 42-64.

Soulsby, 1997. Dynamics of marine sands: A manual for practical applications. Thomas Telford, London,UK.

Southgate, H.N., Wijnberg, K.M., Larson, M., Capobianco, M. and Jansen, H., 2003. Analysis of field data of coastal morphological evolution over yearly and decadal timescales. Part 2: Non-linear techniques. Journal of Coastal Research: 776-789.

Stauble, D.K. and Cialone, M.A., 1996. Sediment dynamics and profile interactions: Duck94. Proceedings of the 25th International Conference on Coastal Engineering, p.^pp. 3921-3934.

Thiébot, J., Idier, D., Garnier, R., Falqués, A. and Ruessink, B.G., 2012. The influence of wave direction on the morphological response of a double sandbar system. Continental Shelf Research, 32(0): 71-85.

Thornton, E., MacMahan, J. and Sallenger Jr, A., 2007. Rip currents, mega-cusps, and eroding dunes. Marine Geology, 240(1): 151-167.

Thornton, E.B. and Guza, R., 1983. Transformation of wave height distribution. Journal of Geophysical Research: Oceans (1978–2012), 88(C10): 5925-5938.

Tiessen, M., Van Leeuwen, S., Calvete, D. and Dodd, N., 2010. A field test of a linear stability model for crescentic bars. Coast. Eng., 57(1): 41-51.

Tiessen, M.C., Dodd, N. and Garnier, R., 2011. Development of crescentic bars for a periodically perturbed initial bathymetry. Journal of Geophysical Research: Earth Surface (2003–2012), 116(F4).

Turner, I.L., Whyte, D., Ruessink, B.G. and Ranasinghe, R., 2007. Observations of rip spacing, persistence and mobility at a long, straight coastline. Marine geology, 236(3-4): 209-221.

van der Wegen, M., Dastgheib, A., Jaffe, B.E. and Roelvink, D., 2011. Bed composition generation for morphodynamic modeling: Case study of san pablo bay in california, USA. Ocean Dynamics, 61(2-3): 173-186.

van Enckevort, I.M.J. et al., 2004. Observations of nearshore crescentic sandbars. J. Geophys. Res.-Oceans, 109(C6): C06028.

Vis-Star, N.C., de Swart, H. and Calvete, D., 2008. Patch behaviour and predictability properties of modelled finite-amplitude sand ridges on the inner shelf. Nonlinear processes in geophysics, 15(6): 943-955.

Vis-Star, N.C., de Swart, H.E. and Calvete, D., 2009. Effect of wave–bedform feedbacks on the formation of, and grain sorting over shoreface-connected sand ridges. Ocean dynamics, 59(5): 731-749.

Vousdoukas, M., Ferreira, Ó., Almeida, L. and Pacheco, A., 2012. Toward reliable storm-hazard forecasts: Xbeach calibration and its potential application in an operational early-warning system. Ocean Dynamics, 62(7): 1001-1015.

Walgreen, M., De Swart, H. and Calvete, D., 2003. Effect of grain size sorting on the formation of shoreface‐connected sand ridges. Journal of Geophysical Research: Oceans (1978‐2012), 108(C3).

Walgreen, M., De Swart, H.E. and Calvete, D., 2004. A model for grain-size sorting over tidal sand ridges. Ocean Dynamics, 54(3-4): 374-384.

Wang, P., Davis Jr, R.A. and Kraus, N.C., 1998. Cross-shore distribution of sediment texture under breaking waves along low-wave-energy coasts. Journal of Sedimentary Research, 68(3).

Weir, B., Uchiyama, Y., Lane, E.M., Restrepo, J.M. and McWilliams, J.C., 2011. A vortex force analysis of the interaction of rip currents and surface gravity waves. Journal of Geophysical Research: Oceans, 116(C5): C05001.

Werner, B.T. and Fink, T.M., 1993. Beach cusps as self-organized patterns. Science, 260(5110): 968-971.

Wijnberg, K.M. and Kroon, A., 2002. Barred beaches. Geomorphology, 48(1): 103-120.

Windle, J. and Rolfe, J., 2013. Estimating nonmarket values of brisbane (state capital) residents for state based beach recreation. Ocean & Coastal Management, 85, Part A(0): 103-111.

Wright, L.D. and Short, A.D., 1984. Morphodynamic variability of surf zones and beaches: A synthesis. Marine geology, 56(1-4): 93-118.

Yu, J. and Slinn, D.N., 2003. Effects of wave-current interaction on rip currents. Journal of Geophysical research, 108(C3): 3088.